

# Limits to Drift Chamber Resolution

Werner Riegler



Dissertation

# Limits to Drift Chamber Resolution

ausgeführt zum Zwecke der Erlangung des akademischen Grades eines Doktors der  
technischen Wissenschaften unter der Leitung von

Dr. Christian Fabjan  
Institut für Kernphysik der TU Wien

eingereicht an der Technischen Universität Wien  
Technisch-Naturwissenschaftliche Fakultät

von

Werner Riegler

Auf der Schanz 9, 4360 Grein  
Matrikelnummer 8825503  
geboren am 30. März 1970 in Enns

Wien, November 1997

# Abstract

ATLAS (A Large Toroidal LHC Apparatus) will be a general-purpose experiment at the Large Hadron Collider that will be operational at CERN in the year 2004. The ATLAS muon spectrometer aims for a momentum resolution of 10% for a transverse momentum of  $p_T=1\text{TeV}$ . The precision tracking devices in the muon system will be high pressure drift tubes (MDTs) with a single wire resolution of  $< 80\mu\text{m}$ . Approximately 370000 MDT tubes will be assembled into  $> 1100$  chambers covering an area of  $\approx 2500\text{m}^2$ . The high counting rates in the spectrometer as well as the aim for excellent spatial resolution and high efficiency put severe constraints on the MDT operating parameters.

This work describes a detailed study of all the resolution limiting factors in the ATLAS environment. A 'full chain' simulation of the MDT response to photons and charged particles as well as quantitative comparisons with measurements was performed. The good agreement between simulation and measurements resulted in a profound understanding of the drift chamber processes and the individual contributions to the spatial resolution. An optimization of the detector physics operating parameters and the electronics parameters was performed.

The detailed study of the individual contributions to the spatial resolution showed that signal rise time fluctuations due to charge deposit fluctuations are one of the major contributions to the spatial resolution of high pressure drift chambers. A scheme to correct for these fluctuations was developed. Resolution limiting factors from space charge effects were studied as well.

A detailed analysis of the MDT efficiency by analysing pulse shapes of inefficient events gave answer to the nature of the inefficiencies. A scheme to increase the MDT efficiency by using a second discriminator was developed.

Vibrations of the MDT wires induced by the ions created in the avalanche are also a resolution limiting contribution at high count rates. This effect as well as the effect of externally induced vibrations were studied.

Finally a frontend electronics scheme that allows to extract all the interesting information contained in the wire chamber signal into a single output channel was developed.

# Contents

<b>Abstract</b>	<b>2</b>
<b>1 Requirements for detectors at LHC</b>	<b>6</b>
1.1 The Large Hadron Collider . . . . .	6
1.2 Physics at LHC and detector requirements . . . . .	6
1.3 ATLAS . . . . .	9
1.4 Muon precision drift chambers . . . . .	11
<b>2 Environment and requirements for the muon chambers in ATLAS</b>	<b>13</b>
2.1 General performance requirements and environment . . . . .	13
2.1.1 Background rates in the muon spectrometer . . . . .	13
2.1.2 Momentum resolution . . . . .	14
2.1.3 Reconstruction efficiency . . . . .	15
2.2 Chamber construction requirements and alignment requirements . . . . .	15
2.3 Single Tube operation requirements . . . . .	17
<b>3 Simulation of the MDT response to charged particle tracks</b>	<b>19</b>
3.1 Detector physics simulation . . . . .	19
3.1.1 Ionization along the particle track . . . . .	20
3.1.2 Drift of the electrons . . . . .	22

3.1.3	The avalanche process . . . . .	24
3.1.4	The induced current signal . . . . .	24
3.1.5	Signal characteristics . . . . .	25
3.2	Electronics Simulation . . . . .	27
3.2.1	The MDT . . . . .	27
3.2.2	Preamplifier . . . . .	29
3.2.3	Noise . . . . .	29
3.2.4	Tail cancellation . . . . .	33
3.2.5	Calculation of the electronics response . . . . .	36
<b>4</b>	<b>Comparison of simulated signal shapes with measurements</b>	<b>38</b>
4.1	Setup and electronics simulation . . . . .	38
4.2	Fe55 signals . . . . .	40
4.3	Muon signals . . . . .	44
<b>5</b>	<b>Comparison of the simulated MDT resolution with measurements</b>	<b>49</b>
<b>6</b>	<b>Working point optimization</b>	<b>56</b>
6.1	Dependence of the resolution on pressure . . . . .	56
6.2	Contributions to the MDT resolution . . . . .	58
6.3	Resolution optimization . . . . .	62
6.4	Optimization of filter time constants . . . . .	68
<b>7</b>	<b>Comparison of time slewing corrections with measurements</b>	<b>72</b>
<b>8</b>	<b>Space charge effects</b>	<b>76</b>
8.1	Theory of space charge effects . . . . .	76
8.1.1	A first order model . . . . .	77

8.1.2	Exact calculation . . . . .	78
8.2	Gas gain reduction due to space charge . . . . .	80
8.3	Shift of the rt-relation . . . . .	80
8.3.1	Shift of the rt-relation due to drift time changes . . . . .	81
8.3.2	Shift of the rt-relation due to gas gain reduction . . . . .	81
<b>9</b>	<b>Temperature effects</b>	<b>85</b>
9.1	Shift of the rt-relation due to drift time changes . . . . .	85
9.2	Shift of the rt-relation due to gas gain changes . . . . .	86
<b>10</b>	<b>Baseline shift</b>	<b>88</b>
<b>11</b>	<b>MDT wire vibrations</b>	<b>92</b>
11.1	General frequency and damping characteristics of the MDT wires . . . . .	92
11.2	Vibrations induced by radiation . . . . .	97
11.3	Externally induced vibrations . . . . .	100
<b>12</b>	<b>MDT efficiency</b>	<b>103</b>
12.1	Introduction . . . . .	103
12.2	Inefficiency due to signals not exceeding the threshold . . . . .	105
12.3	Inefficiencies due to electromagnetic secondaries and charge fluctuations . .	107
12.4	Inefficiencies due to uncorrelated background . . . . .	112
12.4.1	Background characteristics . . . . .	112
12.4.2	Double track separation . . . . .	115
12.4.3	Two filter scheme . . . . .	118
12.4.4	Two Discriminator Scheme . . . . .	125
<b>13</b>	<b>Summary and conclusion</b>	<b>132</b>

# Chapter 1

## Requirements for detectors at LHC

### 1.1 The Large Hadron Collider

The Large Hadron Collider (LHC) will be a 7+7TeV proton-proton collider with a design luminosity of  $10^{34} \text{cm}^{-2} \text{s}^{-1}$ , planned to be operational in the year 2004. It will be installed in the 27km tunnel at CERN/Geneva that currently houses LEP (the Large Electron Positron Collider). The 1232 super conducting dipole bending magnets will contain two separate beam lines with opposite magnetic field strengths of 8.4T. At the interaction points, the transverse bunch radius will be  $15\mu\text{m}$  and the bunch length will be 30cm, so the effective spread of the vertex position is expected to be 5.5cm along the beam direction. The bunch spacing will be 25ns. The LHC will also be able to collide Pb ions reaching centre of mass energies in the PeV range. Some important particle cross sections and interaction rates are shown in fig. 1.1. A p-p cross section between 90 and 130mbarn will result in  $\approx 20$  p-p interactions per bunch crossing for a luminosity of  $10^{34} \text{cm}^{-2} \text{s}^{-1}$ . The total integrated luminosity is expected to be  $10^5$  events/(pbarn  $\times$  year).

### 1.2 Physics at LHC and detector requirements

The most prominent issue for the LHC is the search for the Standard Model (SM) Higgs boson or a family of Higgs bosons when considering the Minimal Supersymmetric extension of the Standard Model (MSSM). The Higgs search is therefore used as a benchmark for detector optimization and is discussed here in order to illustrate the requirements for detectors at LHC.

In case the Higgs boson is not discovered at LEP2 the lower limit on the Higgs mass will be  $\approx 80 \text{GeV}$  at the start up of LHC [1]. For a SM Higgs boson in the mass region below the threshold for  $H \rightarrow WW$  and  $H \rightarrow ZZ$  decays, the Branching Ratio (BR) for  $H \rightarrow b\bar{b}$  is almost 100% since the b-quark is the heaviest particle accessible for the



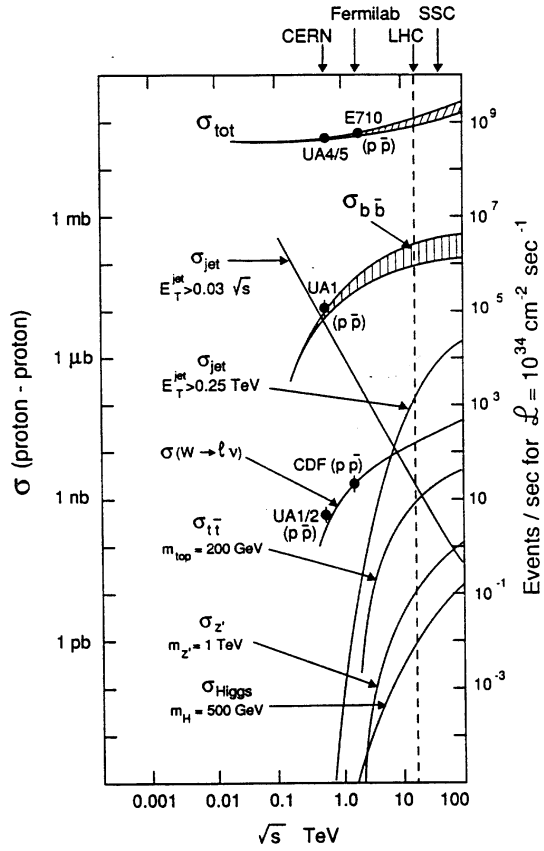


**Figure 1.1** : Cross sections of some characteristic processes. The center of mass energy of LHC will be 14TeV with a design luminosity of  $10^{34} \text{ cm}^{-2} \text{ s}^{-1}$ . The production rate of the Higgs particle is eleven orders of magnitude smaller than the total p-p interaction rate.

Higgs decay. Since the direct  $b\bar{b}$  cross section is very large (fig. 1.1) this channel can only be observed if the Higgs particle is produced in association with  $W$  or  $t\bar{t}$ . In a Higgs mass range of  $80\text{GeV} < m_H < 120\text{GeV}$  the most promising detection channel is the  $H \rightarrow \gamma\gamma$  decay. High detection efficiency is required to observe the rare decay ( $\sigma \times BR \simeq 40\text{fb} \rightarrow \simeq 4000$  events per year). The  $H \rightarrow \gamma\gamma$  channel suffers from large irreducible background from  $q\bar{q} \rightarrow \gamma\gamma$ ,  $gg \rightarrow \gamma\gamma$  and  $qg \rightarrow q\gamma\gamma$  processes. Reducible backgrounds from  $jet - jet$ ,  $\gamma - jet$  and  $Z \rightarrow ee$  events with production cross-sections that are many orders of magnitude larger than the signal cross section require excellent photon/jet and photon/electron discrimination. For an acceptance $\times$ efficiency value of 20% one expects 480 signal and  $> 40000$  background events in the signal mass bin after one year of high luminosity running. If the Higgs particle is produced in association with a  $W$  or  $t\bar{t}$  the leptonic decays of these particles provide an isolated lepton for triggering the experiment. The goal is to reconstruct a peak in the invariant mass spectrum of the  $b\bar{b}$  pairs. The reconstruction and tagging of b-jets with high efficiency is a crucial element in the detector performance in the search for such a decay channel.

In the mass range of  $120\text{GeV} < m_H < 180\text{GeV}$  the  $H \rightarrow ZZ^* \rightarrow 4\mu, 4e$  and  $\mu\mu ee$  channel provide a very clean signature for a SM Higgs boson. For a Higgs mass of  $150\text{GeV}$  one expects  $\approx 550 H \rightarrow 4l$  events per year. The background processes are the  $ZZ^*, Z\gamma^* \rightarrow 4l$  continuum,  $t\bar{t} \rightarrow 4l$  and  $Zb\bar{b} \rightarrow 4l$ . Assuming an acceptance of 50% one expects 264  $H \rightarrow 4l$  events over 470 background events in one year of high luminosity running.

For a mass range of  $180\text{GeV} < m_H < 800\text{GeV}$ , the  $H \rightarrow ZZ \rightarrow 4l$  decay mode is considered to be the most reliable discovery channel since the expected signal rates are large and the background small. For large Higgs boson masses the Higgs width increases rapidly and the signal will be rate limited. For this mass range, the  $H \rightarrow ZZ \rightarrow ll\bar{\nu}\nu$  channel may be considered which is six times more frequent than the  $H \rightarrow 4l$  channel and the signal would show up in the missing  $E_T$  spectrum.

There are many other examples of LHC physics which have been used as a benchmark process for detector design. For the search of the MSSM Higgs bosons  $H^\pm$  and  $A$ , efficient secondary vertex detection for  $\tau$  leptons and  $b$ -quarks as well as high resolution calorimetry for jets and missing transverse energy are essential. Also the search for stable supersymmetric particles sets stringent requirements for the hermiticity and missing  $E_T$  capability of the detectors. New heavy gauge bosons  $W'$  and  $Z'$  could be accessible to the LHC for masses up to 5-6TeV. Therefore high resolution lepton measurement and charge identification are needed even in a  $p_T$  range up to a few TeV. An important chapter of the LHC physics will be the study of heavy quark systems since also at lower luminosity the LHC will be a high rate beauty and top factory. A particularly rich field will be the precise measurement of CP-violation in the  $B_d^0$  system and the determination of the angles in the Cabbibo-Kobayashi-Maskawa unitary triangle. The investigations of  $\bar{B}B$  mixing in the  $B_s^0$  system, rare  $b$  decays and general spectroscopy of states with b-quarks will be of great interest. Precise secondary vertex determination, full reconstruction of final states with relatively low- $p_T$  particles, an example being  $B_d^0 \rightarrow J/\Psi K_s^0$  followed by  $J/\Psi \rightarrow l^+l^-$  and  $K_0^s \rightarrow \pi^+\pi^-$ , and low  $p_T$  lepton first level trigger thresholds as well as second-level track

triggering capability are necessary requirements for the experiment.

## 1.3 ATLAS

'The ATLAS collaboration proposes to build a general-purpose pp detector which is designed to exploit the full discovery potential of the Large Hadron Collider' [2]. The collaboration submitted a Letter of Intent in 1992, a Technical Proposal in 1994 and is currently (1997) writing Technical Design Reports for each subsystem including most of the final specifications. Construction will start in 1998 and the experiment should be ready for the start of LHC in 2004. Cross sections of the experiments can be seen in fig. 1.2 - 1.4.

A super conducting central solenoid with an inner radius of 1.2m and a length of 5.3m will provide an axial magnetic field of 2T in the center of the tracking volume. Three super conducting air core toroid magnet systems will provide an average toroidal field of 0.4T in the muon system. The barrel toroid extends over a length of 26m with an inner diameter of 9.4m and an outer diameter of 19.5m. Two end cap toroids are inserted in the barrel at each end; they have a length of 5.6m and an inner diameter of 1.26m.

The volume inside the solenoid will house the ATLAS Inner Detector (fig. 1.5) consisting of a silicon pixel vertex detector, a silicon strip detector and a transition radiation tracker. The pixel detector consists of three barrel layers of 140 million pixels (each  $50\mu\text{m}$  in  $R-\phi$  and  $300\mu\text{m}$  in the direction along the beam line) and four disks on each side between radii of 11cm and 14cm aiming for a point resolution of  $\sigma_{r-\phi} = 12\mu\text{m}$  and  $\sigma_z = 60\mu\text{m}$ .

The silicon strip detectors with a pitch of  $80\mu\text{m}$  are mounted in four barrel layers at radii of 30, 37.3, 44.7 and 52cm using small angle stereo to provide a z-measurement. The forward detector will consist of different detectors mounted on 9 wheels. The spatial resolution will be  $18\mu\text{m}$  in  $R - \phi$  and  $580\mu\text{m}$  in z.

The Transition Radiation Tracker consists of 420000 proportional drift tubes with 4mm diameter divided into a barrel part and several forward wheels. The detector is operated with a  $Xe/CF_4/CO_2$  gas mixture optimized for the detection of X-rays created as transition radiation in stacks of thin radiators between the tubes. The single wire resolution will be  $170\mu\text{m}$  and the efficiency will be  $> 50\%$  even for the highest rates (15MHz).

The ATLAS calorimetry system is shown in fig. 1.3. A barrel cryostat around the inner detector cavity contains the Electro Magnetic (EM) Liquid Argon (LAr) calorimeter and the solenoidal coil. Two end cap cryostats enclose the electromagnetic and hadronic end cap calorimeters. The EM calorimeter consists of accordion shaped Kapton electrodes and lead absorbers over its full coverage with a segmentation of  $\Delta\eta \times \Delta\phi \approx 0.25 \times 0.25$  aiming for an energy resolution of  $\Delta E/E = 10\%\sqrt{E} \oplus 1\%$  ( $E$  in GeV). The total thickness of the EM calorimeter is above  $24X_0$  in the barrel region and above  $26X_0$  in the forward region. The barrel hadron calorimeter with an inner/outer radius of 228cm/423cm is

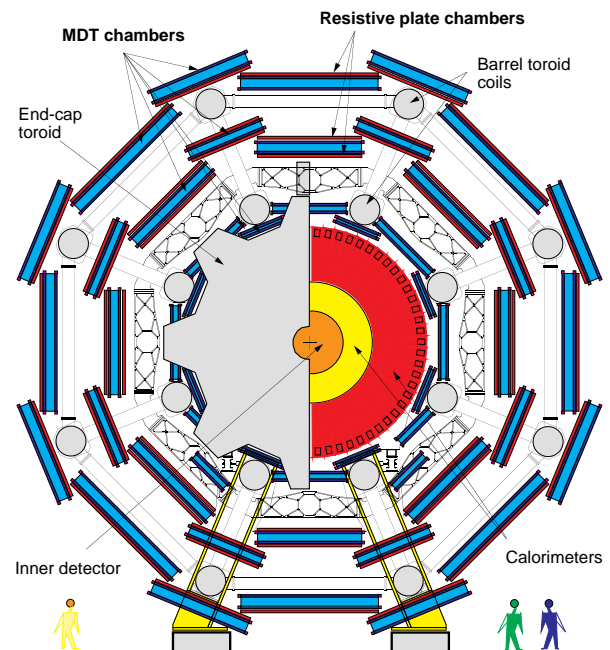


**Figure 1.2 :** Transverse view of the ATLAS experiment.

### ATLAS Calorimetry

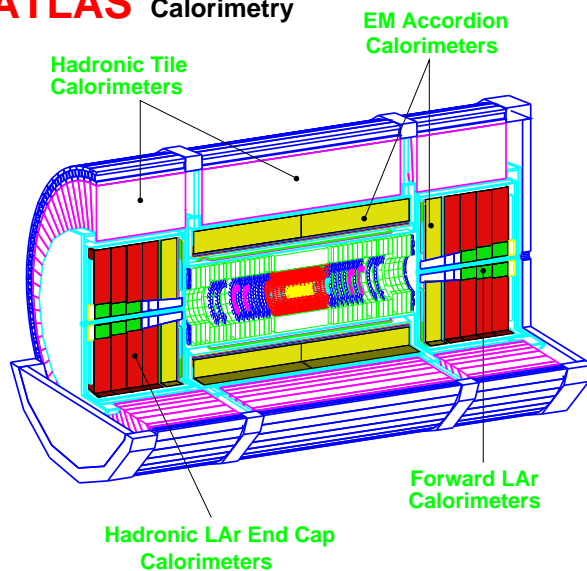


**Figure 1.3 :** Layout of the ATLAS calorimeter system.

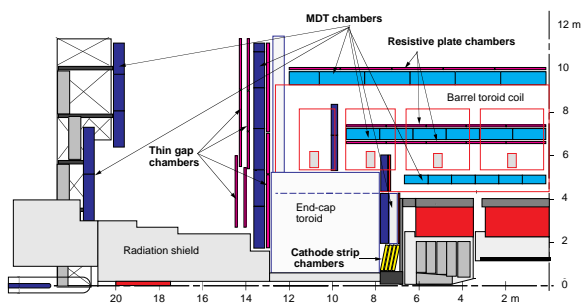


**Figure 1.4 :** Side view of one quadrant of the ATLAS experiment

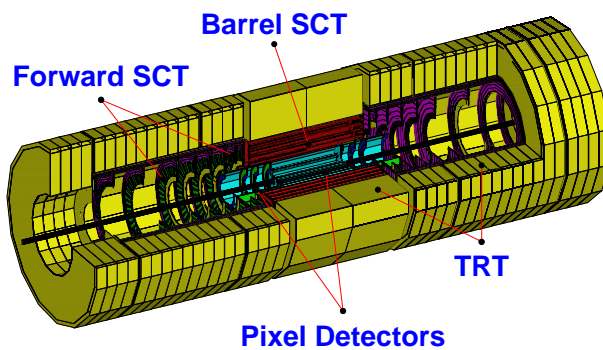


**Figure 1.5 :** The ATLAS inner detector consisting of a pixel detector system, a Semi Conductor Tracker (SCT) and a Transition Radiation Tracker (TRT).

based on sampling technique using steel absorber material and scintillating planes read out by wavelength shifting fibres. A segmentation of  $\Delta\eta \times \Delta\phi \approx 0.1 \times 0.1$  and energy resolution of  $\Delta E/E = 50\% \sqrt{E} \oplus 3\%$  for  $\eta < 3$  should meet the performance requirements. The total thickness at  $\eta = 0$  is 11 interaction lengths. The end cap hadron calorimeter will be a parallel plate geometry liquid argon calorimeter covering a region of  $1.5 < |\eta| < 3.2$ .

The muon spectrometer dominates the size of the ATLAS experiment with its outer diameter of  $\approx 20m$ . Eight super conducting coils will provide an average toroidal magnetic field of 0.4T. The sagitta of the muon tracks will be measured with precision chambers in an inner, middle and outer station. The precision chambers will be Monitored Drift Tube chambers (MDTs) over most of the rapidity range. In the high rate environment at large rapidity, Cathode Strip Chambers (CSCs) will be used (fig. 1.4). Resistive Plate Chambers are used for bunch crossing identification, measurement of the 'second coordinate' (coordinate along the magnetic field lines) and for triggering the experiment. These chambers are gaseous parallel plate chambers with a typical space-time resolution of  $1cm \times 1ns$ . Four layers of resistive plate chambers with two coordinate readout are located near the middle muon station arranged in two groups of two chambers separated by about 40cm. Three additional trigger chamber layers are located in the outer muon station. Low and high  $p_T$  muon triggers are realized by requiring coincidences between groups of chambers in defined roads. The forward region will use Thin Gap Chambers (TGCs) for triggering and second coordinate measurement.

The ATLAS trigger is organized in three levels. The level 1 trigger accepts data at the full bunch crossing rate of 40MHz and must select no more than one interaction in  $10^4$  to reach a trigger rate below 100kHz. The level 2 and level 3 trigger reduce the event rate to 10-100Hz. Level 1 triggers require the following characteristics:  $\geq 1$  muon with  $p_T > 20GeV$ ,  $\geq 1$  isolated electromagnetic cluster with  $E_T > 30GeV$ ,  $\geq 2$  muons with  $p_T > 6GeV$ ,  $\geq 2$  isolated electromagnetic clusters with  $p_T > 20GeV$ ,  $\geq 1$  jet with  $p_T > 150GeV$  or large missing  $E_T$ .

## 1.4 Muon precision drift chambers

The sagittas of muon tracks are measured by precision chambers in an inner, middle and outer muon station. A  $p_T = 1TeV$  muon shows a sagitta of  $\approx 500\mu m$  in the average magnetic field of 0.4T, so a momentum resolution of 10% requires a sagitta measurement accuracy of  $50\mu m$ . The relative position of the muon chambers in the inner, middle and outer station will be monitored by an optical alignment system. The basic elements of these chambers are drift tubes 'Monitored Drift Tubes (MDTs)' with a diameter of 3cm and a  $50\mu m$  central wire that is connected to High Voltage (HV). The principle of operation is shown in fig. 1.6.

A muon crossing the MDT ionizes the detector gas along its track, the electrons are drifting

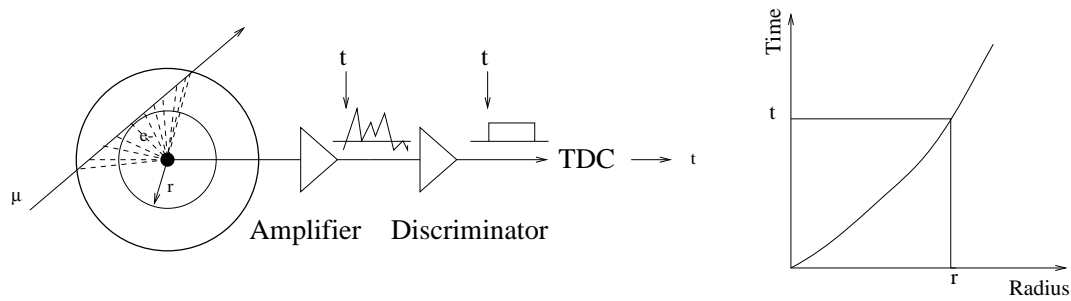


**Figure 1.6** : Principle of the MDT operation. The electron drift time is measured and converted to a distance via a space-drifttime relation ( $rt$ -relation).

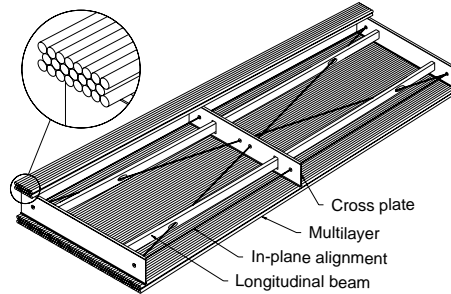


**Figure 1.7** : Two multilayers of MDT tubes each consisting of 3 or 4 layers are glued to a support frame ('spacer structure') to form a chamber. About 1200 of these chambers will be installed in the ATLAS muon spectrometer.

towards the wire in the electric field and are multiplied in an avalanche process close to the wire due to the high field. The movement of the ions induces a current on the wire that is read out at one end of the tube by a current sensitive preamplifier. After discriminating the signal, a Time to Digital Converter (TDC) stores the arrival time of the pulse, such measuring drift time of the ionization electrons. The drift time is then converted to a distance by a space-drifttime relation ( $rt$ -relation). The  $rt$ -relation is obtained by a so called auto-calibration procedure [5]. The detailed analysis of the contributions to the spatial resolution that can be obtained with such a drift tube is discussed throughout this work.

The MDT chambers consist of two multilayers separated by a support structure. Each multilayer combines three of four layers of tubes (fig. 1.7). The support structures provide accurate positioning of the two multilayers with respect to each other and mechanical integrity under effect of gravity and temperature. A X-ray Tomograph will be used to check the wire position accuracy before the chambers are installed [4]. The 1194 MDT chambers will cover an area of  $5500m^2$ . The total number of readout channels is 370000.

# Chapter 2

## Environment and requirements for the muon chambers in ATLAS

### 2.1 General performance requirements and environment

The main performance numbers of the spectrometer are momentum resolution and pattern recognition efficiency in the given background environment. The requirements on the performance will then define the specifications for the precision chambers.

#### 2.1.1 Background rates in the muon spectrometer

The high level of particle fluxes in the muon spectrometer has a major impact on the design considerations of the whole system but also on the optimization of the single tube response. The background sources in the muon spectrometer can be classified into two categories:

- Primary background: primary collision products penetrating into the muon spectrometer through the calorimeters, which are correlated in time with the p-p interaction. Conventional sources of primary background are semileptonic decays of light ( $\pi, K \rightarrow \mu X$ ) and heavy ( $c, b, t \rightarrow \mu X$ ) flavours, gauge Boson decays ( $W, Z, \gamma^* \rightarrow \mu X$ ), shower muons and hadronic punch-through. At small  $p_t < 10\text{GeV}$ , the largest source of background are muons from  $\pi/K$  decays in flight; depending on pseudorapidity, muons with momenta of 3-6 GeV will be absorbed in the calorimeters. At moderate  $p_t > 10\text{GeV}$ , top and Z decays also give a sizeable contribution.
- Radiation background: background consisting mostly of neutrons and photons in the 1 MeV range, produced by secondary interactions in the forward calorimeter, shielding material, the beam pipe and machine elements. Low-energy neutrons, which

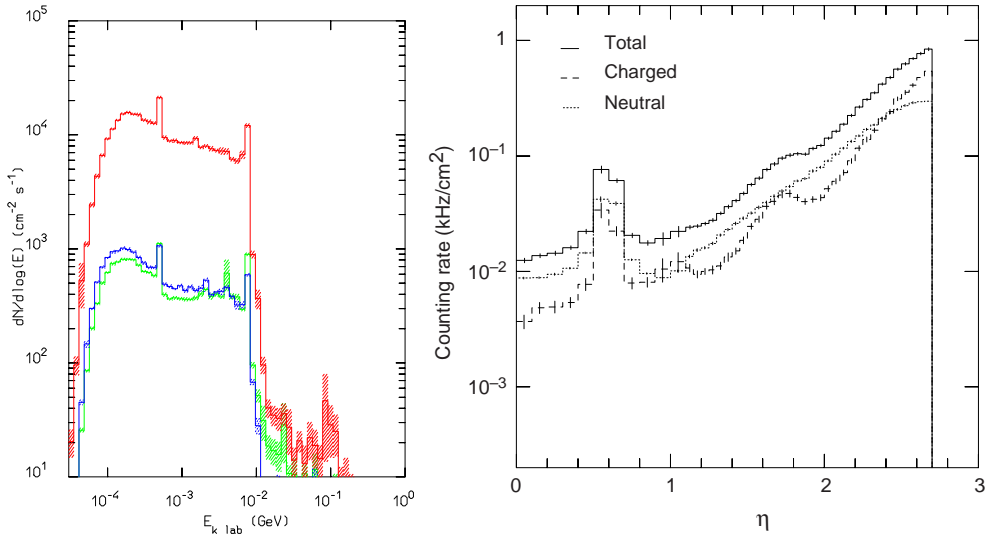


**Figure 2.1** : The left figure shows the expected photon flux as a function of photon energy in different regions of the muon spectrometer (top curve:  $2.3 < \eta < 2.7$ , middle curve:  $1.4 < \eta < 2.3$  and bottom curve:  $\eta < 1.4$ ). The right figure shows the expected counting rate per  $\text{cm}^2$  in the inner muon station.

are an important component of the hadronic absorption process, escape the absorber and produce a gas of low energy photon background through nuclear  $n - \gamma$  processes. This background enters into the spectrometer from all directions and is not any longer correlated in time to the primary p-p interaction. Using the MDT as an example, typical detection efficiencies for photons are at the level of 1%, and those for neutrons one order of magnitude smaller. Notwithstanding these low sensitivities, the low energy neutral particle background will dominate the counting rates in most areas of the spectrometer fig. 2.1.

### 2.1.2 Momentum resolution

The goal is a momentum resolution of about 10% for the most energetic muons that we expect at LHC i.e. about one TeV muons. Fig. 2.2 shows the individual contributions to the momentum resolution in the barrel region of the spectrometer. We see that for low energy muons the momentum resolution is limited by multiple scattering of the muons in the spectrometer material. For high energy muons the momentum resolution is limited by alignment errors and the MDT resolution which was assumed to be  $80 \mu\text{m}$  for this simulation.



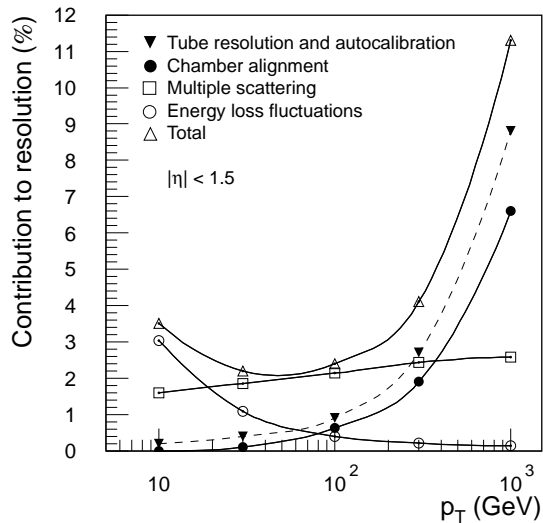


**Figure 2.2** : Individual contributions to the muon momentum resolution as a function of  $p_T$ . The average single wire resolution was assumed to be  $80 \mu m$ .

### 2.1.3 Reconstruction efficiency

The other crucial performance number connected with the muon chambers is the pattern recognition efficiency. The high background levels resulting in large chamber occupancies (up to 10% for a maximum drift time of 500ns) and hit rates (up to 400kHz per tube), put severe requirements on the single tube efficiency and rate capability (occupancy is defined as the fraction of time where the MDT is occupied by an event i.e. the MDT is not able to measure a muon track). Fig. 2.3 shows the pattern recognition efficiency and the fake track rate (number of wrongly reconstructed tracks) for different background levels and layout schemes. The simulation was done assuming a maximum drift time of 480ns and a MDT hit efficiency of 99% where hit efficiency is defined as the MDT efficiency in absence of any correlated or uncorrelated background particles.

## 2.2 Chamber construction requirements and alignment requirements

The main construction requirements for the MDT chambers in order to reach to desired measurement accuracy are the following:

- The elements of the spacer structure are three 'cross-plates' and two 'long-beams' connecting the cross-plates. The tubes must follow the wires within  $100 \mu m$  to limit the deviations from the ideal  $rt$ -relation. Therefore the spacer frame must guide the multilayers along the wire trajectories.

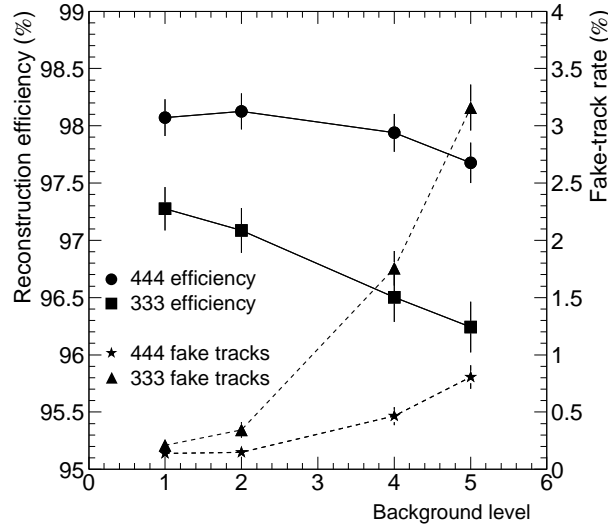


**Figure 2.3** : Pattern recognition efficiency as a function of noise level. A background level of five refers to a safety factor of five on top of the nominal background rate derived from simulation. '444' indicates a chamber configuration with four layers of tubes per multilayer, '333' indicates three layers.

- The sag of the wires must be controllable within  $10\mu m$  up to a wire length of  $4m$ .
- The wires of the chamber must be placed with respect to alignment fiducials with an accuracy of  $20\mu m$ .
- The internal optical alignment system mounted on the spacer structure must monitor the displacement of the middle cross-plate due to temperature gradients at the few micron level.
- The leak rate for a single tube must be  $< 10^{-8}barl/s$ .
- The wire tension (350g) must have an r.m.s. of  $< 7g$ .
- The wire of a single tube has to be positioned to  $10\mu m$  r.m.s. (in projection) with respect to the outer tube wall at a few designated positions along the tube axis.
- The optical alignment system must measure the relative position of the inner, middle and outer muon station with an accuracy such that the maximum alignment contribution to the sagitta measurement is  $< 30\mu m$ .

## 2.3 Single Tube operation requirements

The general requirements for the MDT system described above translate into requirements for all the individual parts of the system. The requirements for the single tube operation are described in detail in the following sections. How to meet the individual specifications and what the limitations are will be discussed throughout this work.

### Resolution

The single tube resolution is directly connected to the momentum resolution for high energy muons. The requirement is an average resolution of  $80\mu m$ . One can arrive at such resolution levels by using gases with low diffusion coefficients and/or high pressure. This would in principle not limit the choice of gases very much, but all the other requirements described throughout this chapter have serious implications on the choice.

### MDT efficiency

The reconstruction efficiency is linked directly to the MDT efficiency. The requirement is a hit efficiency of  $> 99\%$  i.e. in the absence of background particles a muon traversing a single MDT tube should be measured with an accuracy of  $80\mu m$  in more than  $99\%$  of the cases. This can be achieved by either using high gas gain or low thresholds. To arrive at a high efficiency also in the presence of background particles one prefers a fast drift gas to keep the occupancy low or one even needs dedicated electronics to identify piled up signals.

### Space charge effects

The high background rates cause significant amounts of space charge in the MDT volume. As the electric field changes, the electron drift velocity changes, the  $rt$ -relation is shifted and therefore the single wire resolution is deteriorated. This effect puts severe requirements on the choice of the drift gas and the gas gain. To minimise this additional bias in resolution one has to find a gas where the electron drift velocity depends only weakly on the electric field giving a very linear  $rt$ -relation.

### B-field dependence of the $rt$ -relation

The drift of the electrons is affected by the magnetic field, so we have to use different space drifttime relations in different magnetic field regions of the detector. We derive the  $rt$ -relation by a so called 'auto calibration' procedure [5]. For this procedure we have to use the tracks from a certain region of a chamber, so if the magnetic field changes a lot over this region we only derive an average  $rt$ -relation and the resolution decreases. To minimize this effect one prefers a gas where the space drift time relation has a weak dependence on the magnetic field.

### MDT aging

The high background rates and the aim for good momentum resolution are the driving

issues for the MDT operation requirements. One of the biggest concerns is the possible degradation of the drift chamber performance due to large amounts of charge deposit on the wire. Assuming the rates given above together with a gas gain of  $2 \times 10^4$  we expect a charge deposit of 0.6C per cm of wire for 10 years of high luminosity LHC running (including a safety factor of 5). Such a high amount of charge can cause aging effects resulting from deposits of various kinds on the wire and the cathode. These deposits can either reduce the MDT performance or even completely destroy a tube. To minimise these effects we want to operate the chamber at the lowest possible gas gain that is still compatible with our requirements on resolution. The aging problem also puts severe constraints on the choice of gas and construction materials.

### **Baseline variations**

The wires of the MDTs are decoupled from the readout electronics by a capacitor, so the system is AC-coupled. Since in an AC-coupled system the signals must integrate to zero over long time scales there will be a fluctuation of the baseline for high counting rates, i.e. a signal is 'sitting on the long tail' of all the previous events. Since the induced current signals have a very long tail (maximum ion drift time  $\approx 4\text{ms}$ ) and the time scale for feeding back the charge to the wire is of the order  $\tau = CR_l \approx 1\text{ms}$  ( $R_l$  is the high voltage loading resistor and  $C$  is the decoupling capacitor) the baseline is still affected by signals that occurred  $\approx 10\text{ms}$  earlier. With a maximum count rate of 400kHz per tube this can result in significant baseline shifts. To avoid this problem one needs dedicated electronics for baseline restoration.

### **Wire vibrations**

Another effect that can limit the MDT resolution are vibrations of the wire. Two effects causing such vibrations have been observed: vibrations of the wire due to vibrations of the structure the chamber is fixed to and vibrations due to repulsion of the wire by positively charged ions created in the avalanche. The vibration induced by the moving ions depends mainly on the charge deposit per event and the counting rate.

# Chapter 3

## Simulation of the MDT response to charged particle tracks

In order to find out if we have a good understanding of the detector performance, a detailed simulation of the detector physics processes and the electronics was performed and compared to measurements.

Three programs were used for simulating the response of the MDT to charged particle tracks: HEED [6], MAGBOLTZ [7] and GARFIELD [8].

The HEED program was written by Igor Smirnov and computes in detail the energy loss of fast charged particles in gases, taking delta electrons and optionally multiple scattering of the incoming particle into account. The program can also simulate the absorption of photons through photo ionisation in gaseous detectors.

The MAGBOLTZ programme, written by Steve Biagi, computes electron transport parameters for a large variety of gases and mixtures of gases. The program is based on the numerical solution of the Boltzmann transport equation.

GARFIELD, written by Rob Veenhof, is a program for simulation of two and three dimensional drift chambers. It is interfaced to MAGBOLTZ and HEED and computes field maps, electron and ion drift lines, drift time tables and arrival time distributions, signals induced on the wires by moving ions and electrons etc.

### 3.1 Detector physics simulation

Using the programs described above we are able to simulate the detector physics processes in detail. The calculations were done for two gases:  $Ar/CO_2/CH_4$  91/4/5 which is a very fast and linear gas with the disadvantage of high diffusion and bad aging behaviour and

$Ar/CO_2$ 80/20 which is a slow and nonlinear gas having the advantage of low diffusion and 'nice' aging properties. A gas mixture combining the 'nice' properties of these two mixtures would be desirable.

### 3.1.1 Ionization along the particle track

The muon interacts electromagnetically along its track causing ionization of the detector gas. Since the interactions are independent, the number of interactions per unit of track length is Poisson distributed resulting in an exponential distribution of the distances between the interaction points.

The main interactions liberating electrons are the following:

- The muon ionizes a gas atom creating a primary electron that can have sufficient energy to cause gas ionization itself.
- The muon excites a gas atom which returns to the ground state via one of many possible mechanisms. It can deposit charge in the gas volume by emitting an Auger electron or by emitting a photon which (rarely) itself causes ionization in that gas via the photoeffect.

Since the range of the primary electrons is on average quite small the gas is left with clusters of electron-ion pairs along the muon track. The energy deposit is normally characterised by the number of clusters per unit of length and the number of electrons per cluster. Fig. 3.1 shows the average energy deposit and the average number of clusters per unit of length for different gases.

The energy deposited by the muon in the gas volume depends on the muon energy in the characteristic way described by the Bethe Bloch formula (fig. 3.2).

The figure also shows the number of electrons created by the primary electrons ('cluster size distribution') as simulated by HEED. Although most of the primary electrons have a very short range there is a small fraction of very high energetic electrons (delta electrons) creating tracks up to a length of several mm.

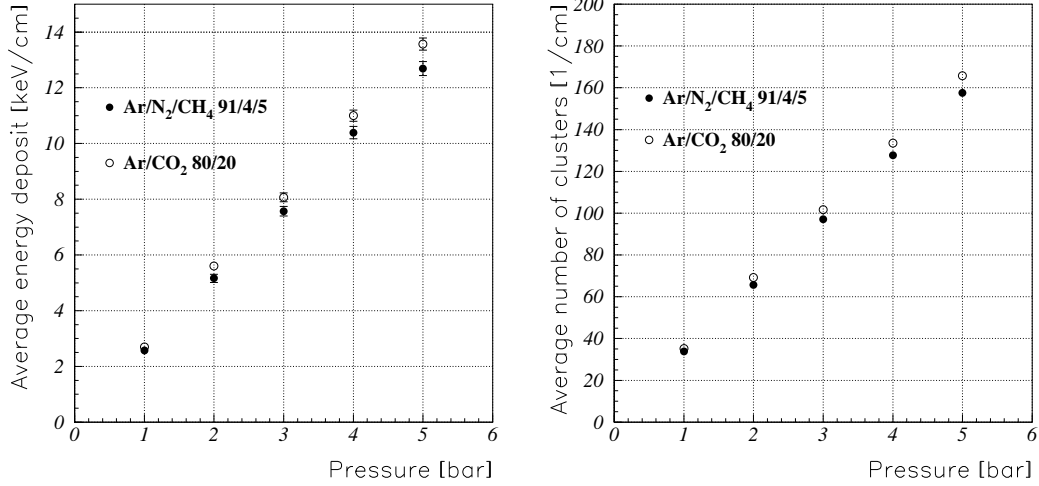


**Figure 3.1** : Average energy deposit and the number of interactions (clusters) per unit of length for two gases calculated with HEED. The muon energy is 100GeV.

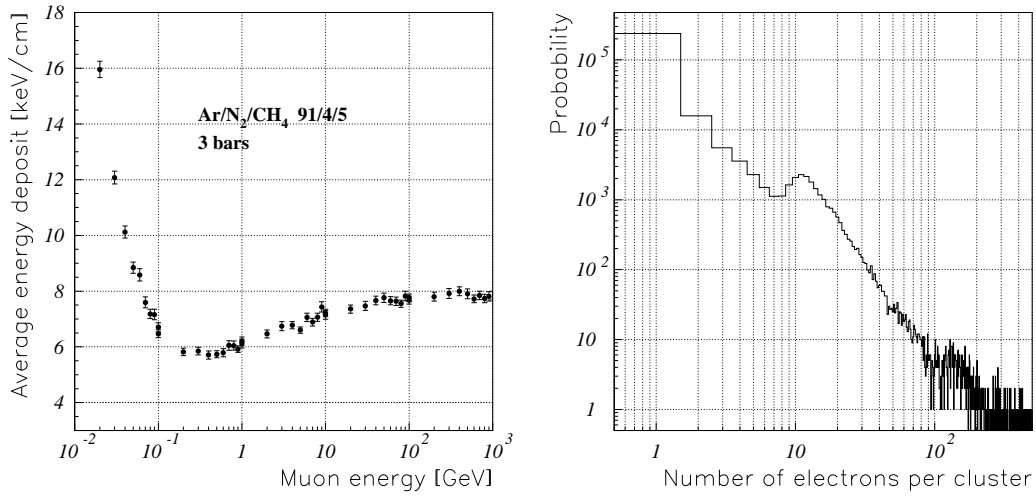


**Figure 3.2** : Energy deposited in the gas Ar/N<sub>2</sub>/CH<sub>4</sub>91/4/5 at 3bars absolute for different muon energies calculated with HEED. The right figure shows the cluster size distribution given by HEED i.e. the number of electrons liberated by one primary electron.

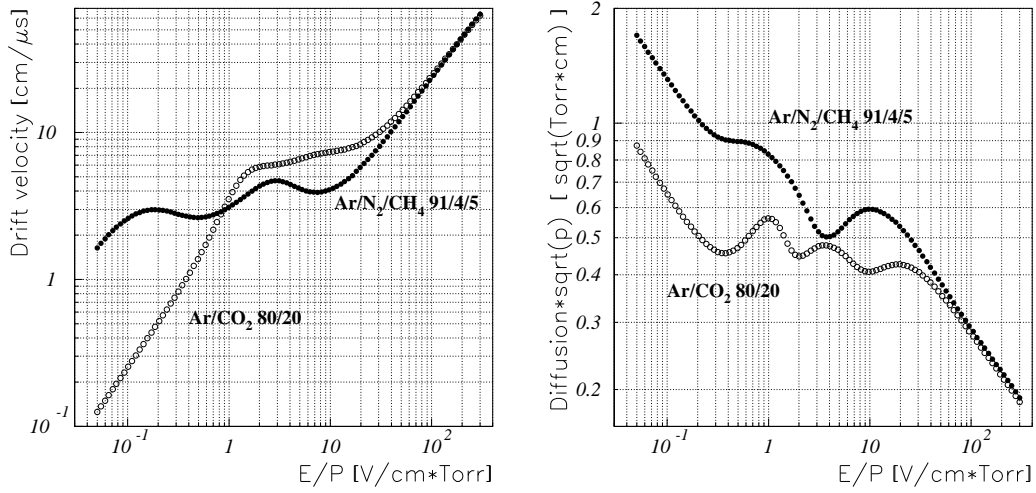


**Figure 3.3** : Drift velocity and diffusion as a function of  $E/P$ .

### 3.1.2 Drift of the electrons

The electrons created by the muon along its track drift towards the wire along the electric field lines. The drift of the electrons can be characterized by the drift velocity and longitudinal and transverse diffusion. These parameters are calculated using MAGBOLTZ. The electron drift velocity and the diffusion as a function of  $E/P$ , where  $E$  is the electric field and  $P$  the gas pressure, are shown in fig. 3.3. We see that the  $Ar/CO_2$  mixture shows considerably less diffusion compared to the  $Ar/N_2/CH_4$  mixture.

From the electric field and the drift velocity parameters (fig. 3.4) we find the  $rt$ -relation for the two gas mixtures (fig. 3.5). Since the drift velocity of the  $Ar/N_2/CH_4$  mixture depends only weakly on the electric field, the space-drifttime relation is more linear and shows less dependence on the gas pressure compared to the  $Ar/CO_2$  mixture.



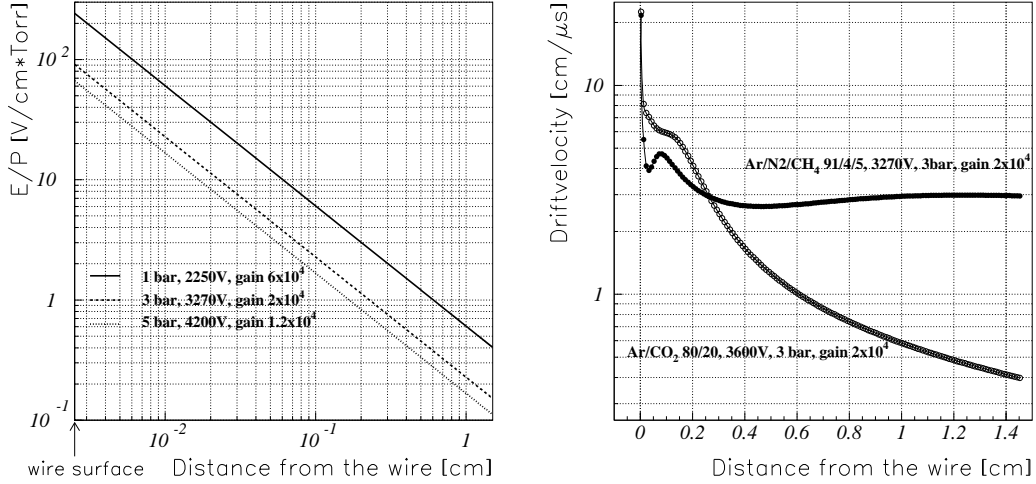


**Figure 3.4** : The left figure shows typical  $E/P$  values for the MDTs. The gas gain was adjusted such that the total amount of charge deposited on the wire is the same. The right figure shows the drift velocity as a function of radius for different gases.

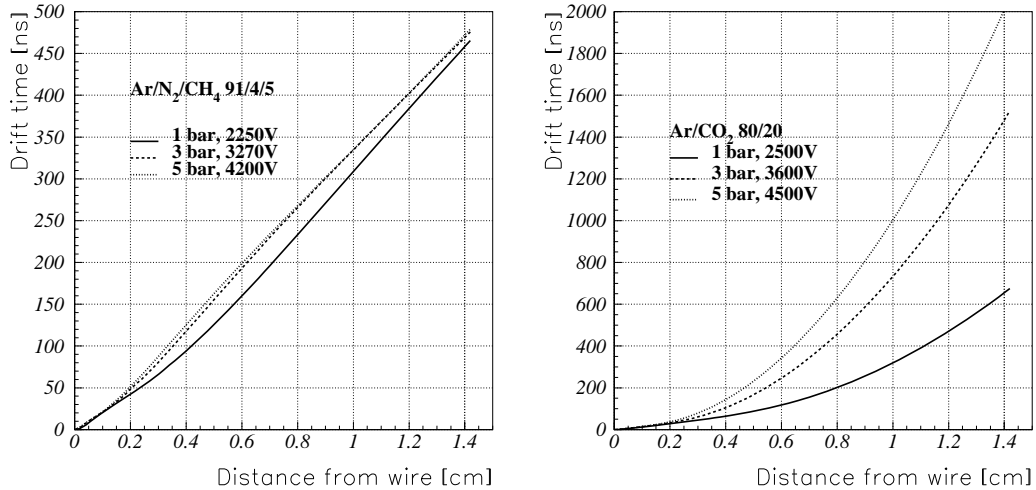


**Figure 3.5** :  $Rt$ -relations for different gases and pressures. 'Linear' gas mixtures show considerably less pressure dependence compared to 'nonlinear gases'.

### 3.1.3 The avalanche process

As the drifting electrons approach the wire they gain enough energy to ionize the counting gas and an avalanche process starts. Typical amplification factors used in drift chambers are  $10^4$  to  $10^5$ . The amplification is a statistical process which for a cylindrical geometry is well described by a Polya [12] distribution.

$$f(x) \propto x^\Theta e^{-(1+\Theta)x}$$

where  $\Theta$  is a parameter between 0 and 1.

MAGBOLTZ calculates the Townsend coefficient, so in principle one can find the gas gain for a given voltage by integrating this coefficient. The Townsend coefficient  $\alpha$  describes the increase in the number of free electrons over a path length  $dr$ . This quantity depends in a complicated manner on the electron energy and distribution and thus on the electric field and the gas mixture. The total gas amplification factor is given by

$$\frac{N}{N_0} = \exp \left[ \int_{r_a}^{r_{min}} \alpha(r) dr \right] = \exp \left[ \int_{E(r_a)}^{E_{min}} \frac{\alpha(E)}{dE/dr} dr \right] \quad (3.1)$$

Since the avalanche multiplication is an exponential process, small uncertainties in the Townsend coefficient result in large uncertainties of the gas gain and the theoretical values differ significantly from the measurements (fig.3.6).

The amplification factor for a given voltage was taken from measurements and given to GARFIELD as an input parameter. The avalanche simulation in GARFIELD is done by choosing the gain randomly from the given Polya distribution and reconstructing the average avalanche process for each incoming electron.

### 3.1.4 The induced current signal

The simulation of the induced current signal is the most critical point in the whole simulation chain. The movement of the ions and electrons created in the avalanche induces a current on the wire. Fig. 3.7 shows measured values for the ion mobility used for this simulation.

Since close to the wire the electric field varies strongly, the peak of the induced current signal depends strongly on the actual position of the creation of the charge. Also the electric field within the avalanche may be distorted by the surrounding ions.

Two models for calculation of the current signal are available in GARFIELD:

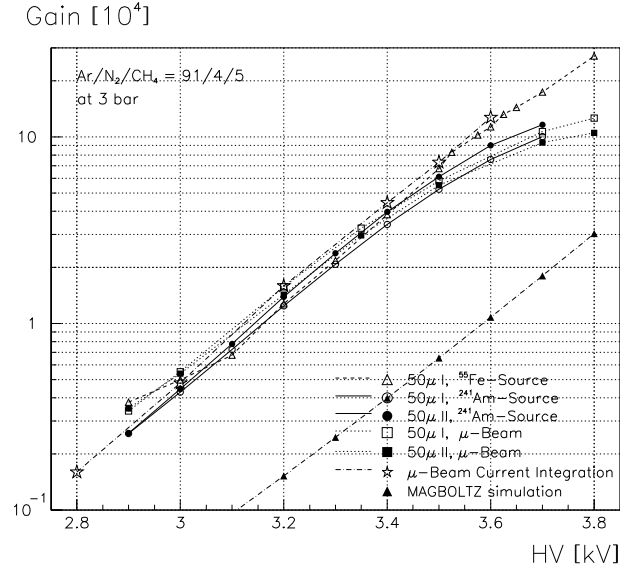


**Figure 3.6** : Amplification Factor simulated by MAGBOLTZ compared to measurements [11].

1. The induced current signal is calculated by tracking the ions from the wire surface according to the field-dependent ion mobility, the electron component is neglected, so this model assumes that the avalanche takes place very close to the wire ( $< 1\mu\text{m}$ ).
2. The average avalanche shape for the given gas gain is reconstructed using the Townsend coefficient. The ions and the electrons are tracked in the field from their point of creation according to the given ion mobility and the electron drift velocity from MAGBOLTZ. This model should in principle be the most realistic one if one can neglect space charge effects within the avalanche.

The two different models are evaluated in the next section. The induced current signal for the given particle track is integrated in specified time bins and written to a file for use in the subsequent simulation. In the next step the signal is further processed by folding it with the electronics response in order to find the preamplifier output.

### 3.1.5 Signal characteristics

According to Ramo's theorem [15] the current signal induced on an electrode is given by

$$i(t) = -\frac{q}{V}v(t)E(x(t)) \quad v = \mu E$$

where  $q$  is the charge moving with a velocity  $v(t)$  at position  $x(t)$ ,  $E$  is the electric field

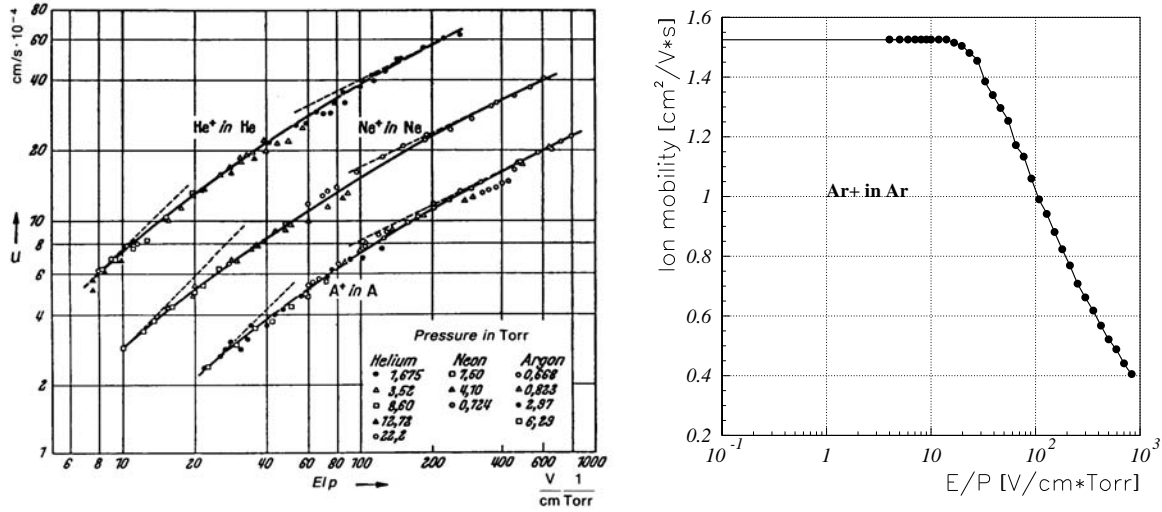


**Figure 3.7** : Ion mobility for different gases and the corresponding ion mobility  $\text{Ar}^+$  in Ar [13]. For low fields the mobility is constant, for high fields it falls off as  $1/\sqrt{E}$  [14]. Since we expect  $E/P$  values of up to 200  $\text{V}/\text{cm}\cdot\text{Torr}$  the signal shape and the pulse height will definitely be affected by the varying ion mobility.

and  $V$  the potential of the electrode. Assuming a constant ion mobility we can calculate the current induced by a single ion moving from the wire surface to the cathode.

$$E(r) = \frac{V_0}{r \log \frac{b}{a}} \quad \text{where} \quad \begin{array}{l} E \dots \text{electric field} \\ V_0 \dots \text{voltage on the wire} \approx 3500\text{V} \\ a \dots \text{wire radius} = 25\mu\text{m} \\ b \dots \text{tube radius} = 1.46\text{cm} \end{array} \quad (3.2)$$

$$\rightarrow i(t) = \frac{q}{2 \log \frac{b}{a}} \frac{1}{t + t_0} \quad t = 0 \dots t_{max} \quad t_0 = \frac{a^2 \log \frac{b}{a}}{2V_0\mu} \quad t_{max} = \frac{\log \frac{b}{a}}{2\mu V_0} (b^2 - a^2) \approx t_0 \frac{b^2}{a^2}$$

$t_{max}$  is the time it takes the ions to move from the wire to the tube wall. With a mobility of  $\mu = 0.52 \text{cm}^2/\text{V}\cdot\text{s}$  and  $q = e_0 = 1.609 \times 10^{-19} \text{C}$  we find

$$t_0 = 11\text{ns} \quad t_{max} = 3.73\text{msec} \quad i(t=0) = 1.15\text{pA}$$

E.g. a 5.9keV  $\text{Fe}55$  photon creating a cluster of 225 electrons in a chamber operated at 3 bars with a gain of  $2 \times 10^4$  induces a current pulse with a peak of  $225 \times 2 \times 10^4 \times 1.15\text{pA} = 5.2\mu\text{A}$ .

## 3.2 Electronics Simulation

### 3.2.1 The MDT

A schematic of the MDT circuit together with a simplified model are shown in fig. 3.8.  $R_{in}$  represents the preamplifier input resistance which will be  $100\ \Omega$ . To avoid reflections on one end of the tube the termination resistor  $R_t$  is matched to the tube impedance. For a tube radius of  $1.46\text{cm}$  and a  $50\ \mu\text{m}$  wire  $R_t = \sqrt{LC} = 382\ \Omega$ , where  $C$  is the tube capacitance and  $L$  the tube inductance per unit of length. The decoupling capacitors were chosen to be  $500\text{pF}$ .

The HV loading resistor  $R_l$  should be high to limit the current in case of a breakdown, but it should be low enough to avoid significant voltage drop for the rates we expect. Choosing  $R_l = 1\text{M}\Omega$  we expect a voltage drop  $2\text{V}$  for a count rate of  $250\text{kHz}$  which is an acceptable value.

A  $50\ \mu\text{m}$  W/Rh wire has a DC resistance of about  $50\ \Omega/\text{m}$ .  $R_1$  is the total wire resistance between the impact point and the preamp side,  $R_2$  the wire resistance between impact point and termination end.

The analytical transfer function of the MDT (from the impact point to the preamp input) can be found in [16]. Fig. 3.8 shows the absolute value of the transfer function for a  $1\text{m}$  tube.

The tube transfer function has 4 characteristic frequency intervals

1.  $f < 10^2\text{Hz}$

A large part of the signal leaves the wire via the  $1\text{M}\Omega$  HV loading resistor.

2.  $10^2 < f < 10^5\text{Hz}$

In this frequency range half the induced signal leaves via the termination resistor side and the other half via the preamp side, since the signal divides like the ratio of the two capacitors.

3.  $10^5 < f < 10^9\text{Hz}$

The capacitors can be neglected and the signal splits like  $(R_t + R_2)/(R_1 + R_2 + R_t + R_i)$ .

4.  $> 10^9\text{Hz}$ :

The frequency dependent wire resistance starts to be important and the high frequency signals are attenuated strongly.

The leading edge of the signal is mostly affected by the 3rd domain, the overall signal shape is dominated by domain 2 and 3. Since the frequencies  $> 10^9\text{Hz}$  are cut off by the preamp we can use a simplified circuit for the MDT response (fig. 3.8). The transfer function of the circuit is given by

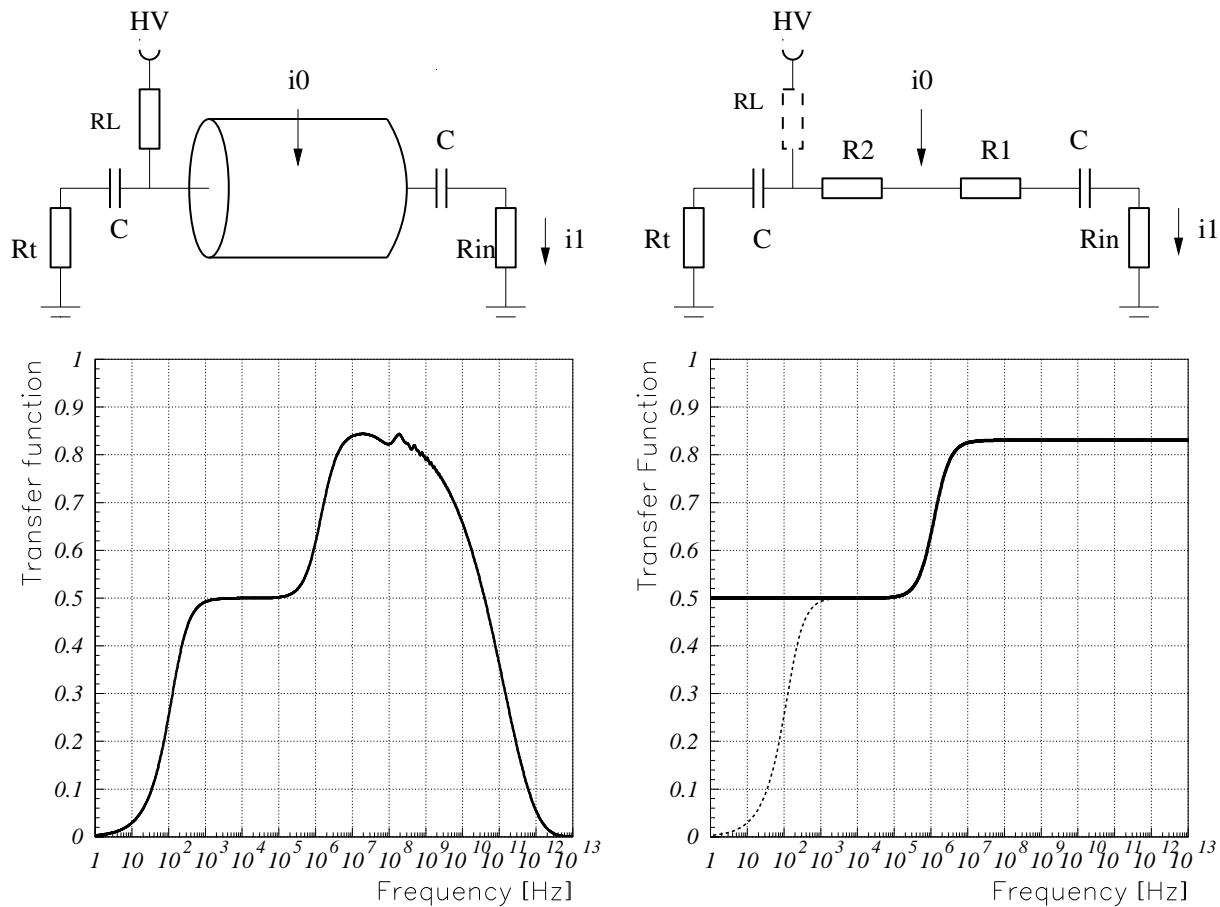


**Figure 3.8** : Transfer function of the MDT from the impact point to preamp input. The left figure shows the exact calculation [16], the right figure shows the transfer function from the simplified model with and without the loading resistor. The values assumed for this plot are  $R_l = 1M\Omega$ ,  $R_1 = R_2 = 23\Omega$ ,  $C = 470pF$ ,  $R_t = 382\Omega$ ,  $R_{in} = 55\Omega$ .

$$\begin{aligned}
\frac{i_1}{i_0} &= \frac{s(b + as)}{e + ds + cs^2} \\
a &= R_l(R_2 + R_t) + R_2R_t \\
b &= \frac{1}{C}(R_2 + R_l) \\
c &= R_l(R_1 + R_i + R_2 + R_t) + R_1R_t + R_iR_t + R_2R_t \\
d &= \frac{1}{C}(2R_l + R_t + R_1 + R_i + R_2) \\
e &= \frac{1}{C^2}
\end{aligned} \tag{3.3}$$

Since within the first  $\mu s$  the effect of the loading resistor on the MDT signal shape is negligible we can drop this resistor for pulse shape studies and arrive at a simpler transfer function

$$\begin{aligned}
\frac{i_1}{i_0} &= \frac{R_2 + R_t}{R_{in} + R_1 + R_2 + R_t} \times \frac{s + \frac{1}{\tau_1}}{s + \frac{1}{\tau_2}} & \tau_1 &= C \times (R_2 + R_t) \\
& & \tau_2 &= C/2 \times (R_{in} + R_t + R_1 + R_2)
\end{aligned} \tag{3.4}$$

This transfer function is equivalent to a 'pole/zero' or 'zero/pole' network described below. As we can see, the transfer function depends on the avalanche position along the wire which results in different signal shapes for different impact parameters as well as different signal losses.

These simplified circuits are only applicable if the tube is terminated at the characteristic tube impedance on one side since reflections are not taken into account.

### 3.2.2 Preamplifier

The preamp was assumed to be an ideal preamp followed by  $n+1$  RC integration stages [17], [18].

$$f(s) = \frac{n!\tau}{(1 + s\tau)^{n+1}} \quad \text{where} \quad \begin{array}{l} n \dots \text{number of integrations} \\ \tau \dots \text{time constant of one integration stage} \\ n\tau = t_p \dots \text{peaking time} \end{array} \tag{3.5}$$

This corresponds to a delta response of

$$\bar{f}(t) = \left(\frac{t}{\tau}\right)^n e^{-\frac{t}{\tau}} \quad \bar{f}_{max} = n^n e^{-n} \tag{3.6}$$

Fig. 3.9 shows the delta responses for different integration numbers.

### 3.2.3 Noise

A major part of the noise in the MDTs consists of thermal noise caused by the termination resistor. The thermal noise of a resistor  $R$  can be represented as a current noise source in parallel with a noiseless resistor  $R$  and having a mean square current magnitude of

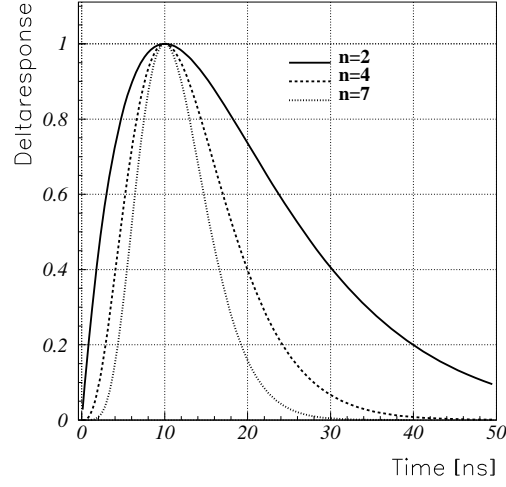


**Figure 3.9** : Delta responses of preamps with 10ns peaking time for different numbers of integrations.

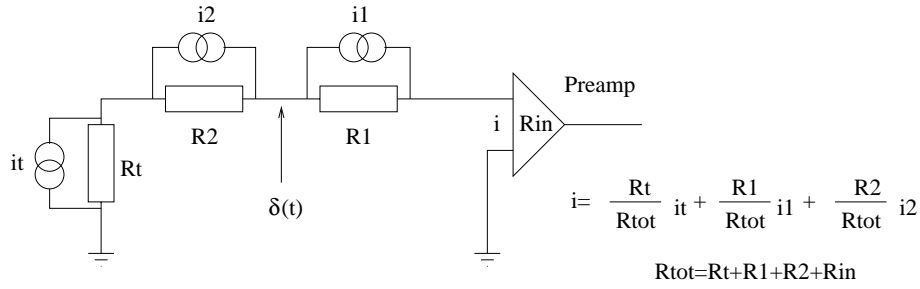


**Figure 3.10** : Thermal noise can be modelled as a current source parallel to a noiseless resistor.  $R_1$  and  $R_2$  are the wire resistances left and right of the impact point.

$i_{rms}^2 = 4kT/R \times df$  where  $k$  is the Boltzmann constant,  $T$  is the temperature of the resistor and  $df$  the frequency interval [18]. The current does not depend on the frequency, so thermal noise is white noise. The equivalent circuit for the MDT is shown in fig. 3.10.

To find the output rms voltage  $V_{rms}^2$  for a current sensitive preamplifier with transfer function of  $f(s)$  we have to evaluate the expression

$$V_{rms}^2 = \left( \frac{R_t^2}{R_{tot}^2} i_{rms_t}^2 + \frac{R_1^2}{R_{tot}^2} i_{rms_1}^2 + \frac{R_2^2}{R_{tot}^2} i_{rms_2}^2 \right) \int_0^\infty |f(i\omega)|^2 \frac{d\omega}{2\pi} \quad R_{tot} = R_t + R_1 + R_2 + R_{in} \quad (3.7)$$

With  $i_{rms}^2 = 4kT/R$  this expression becomes



$$V_{rms}^2 = \frac{R_1 + R_2 + R_t}{R_{tot}^2} 4kT \int_0^\infty |f(i\omega)|^2 \frac{d\omega}{2\pi} \quad (3.8)$$

Inserting the transfer function (3.5) and solving the integral by complex integration gives

$$V_{rms}^2 = \frac{R_1 + R_2 + R_t}{R_{tot}^2} 4kT \frac{(2n)! \tau}{2^{2n+2}} \quad (3.9)$$

In order to derive the Equivalent Noise Charge (ENC) one has to divide the  $V_{rms}$  by the peak of the preamp output caused by a unit delta input pulse on the wire. The ENC in electrons is obtained by dividing by the electron charge  $e_0$ .

$$ENC = \frac{V_{rms}}{e_0 * peak} \quad peak = \frac{R_2 + R_t}{R_{tot}} n^n e^{-n} \quad (3.10)$$

resulting in

$$ENC = \frac{\sqrt{R_t(R_1 + R_2 + R_t)}}{R_2 + R_t} \frac{1}{e_0} \frac{e^n}{2^n} n^{-(n+1/2)} \sqrt{t_p \frac{kT}{R_t}} (2n)! \quad (3.11)$$

The ENC depends on the wire length and the impact point. Fig. 3.11 shows the ENC for different peaking times and integration numbers ( $T = 300K$ ,  $R_t = 382\Omega$ ) for a very short tube neglecting the wire resistance.

How the ENC changes with wire length and impact parameter is shown in fig. 3.12. The ENC for the middle of the wire is almost independent of the wire length since signal and noise are attenuated by nearly the same factor. The preamp noise was neglected in this study since it should be very small compared to the termination resistor noise.

The noise is introduced to the simulation by adding gaussian numbers every time bin such that the correct  $V_{rms}$  on the output is reproduced.

The noise determines the minimum threshold we can apply to the preamplifier output. To avoid accidental threshold crossings we have to set the threshold to  $> 5V_{rms}$ .

$$thr_{min} = 5 \times \sigma_{noise} \quad (3.12)$$

It is common use to express the threshold in 'electrons'. A threshold of n electrons corresponds to the voltage equivalent to the peak of the signal caused by n ionization electrons in the tube. Fig. 3.11 shows the thresholds equivalent to  $5 \times \sigma_{noise}$  for different preamp peaking times and integration numbers for a gas gain of  $2 \times 10^4$ .

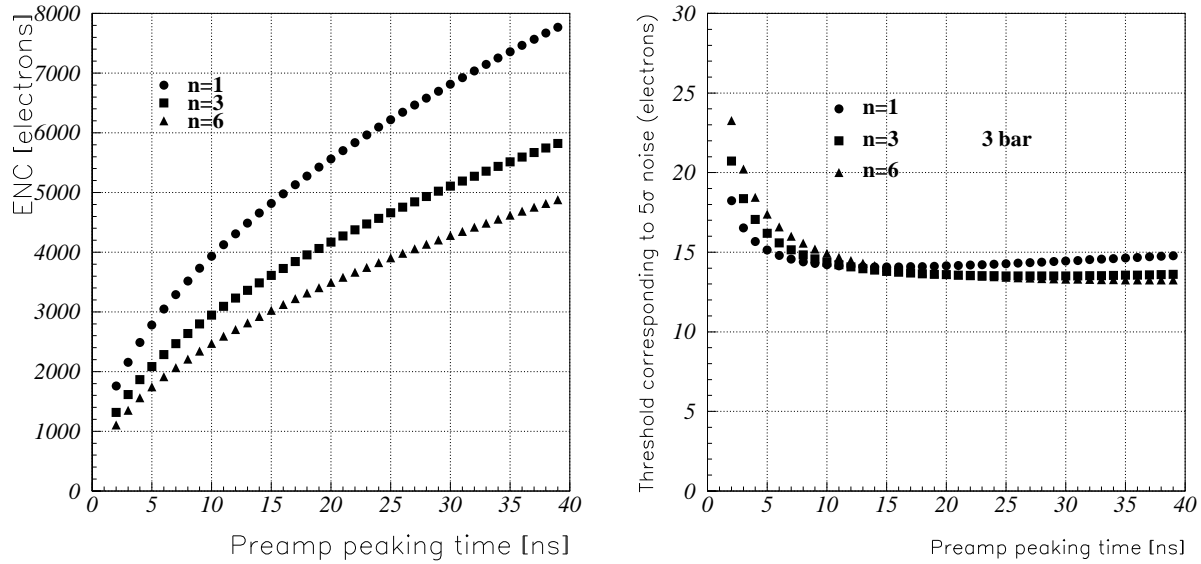


**Figure 3.11** : ENC from the termination resistor for different preamp peaking times and integration numbers and equivalent  $5\sigma$  noise levels for a gain of  $2 \times 10^4$ . The wire resistance was neglected for this figure. The ENC and equivalent minimum threshold for different wire lengths and impact parameters can be found by multiplying these numbers by the factors given in fig. 3.12.

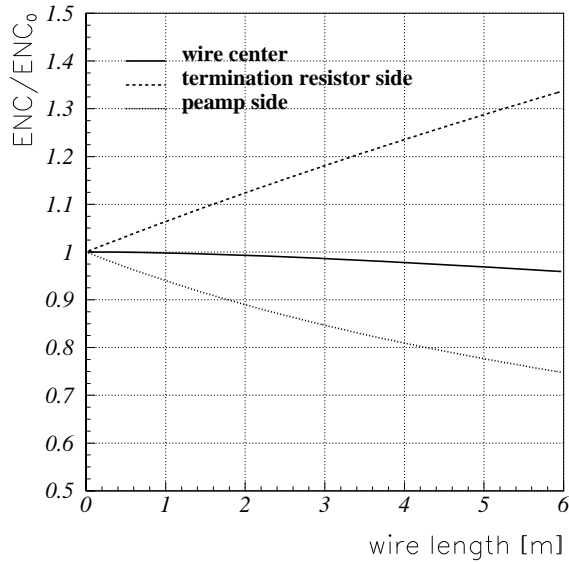


**Figure 3.12** : Dependence of the ENC on the wire length with respect to the ENC for a very short tube. For a particle crossing a 6m MDT close to the termination resistor side, the signal to noise ratio is a factor 1.33 worse compared to a very short tube.

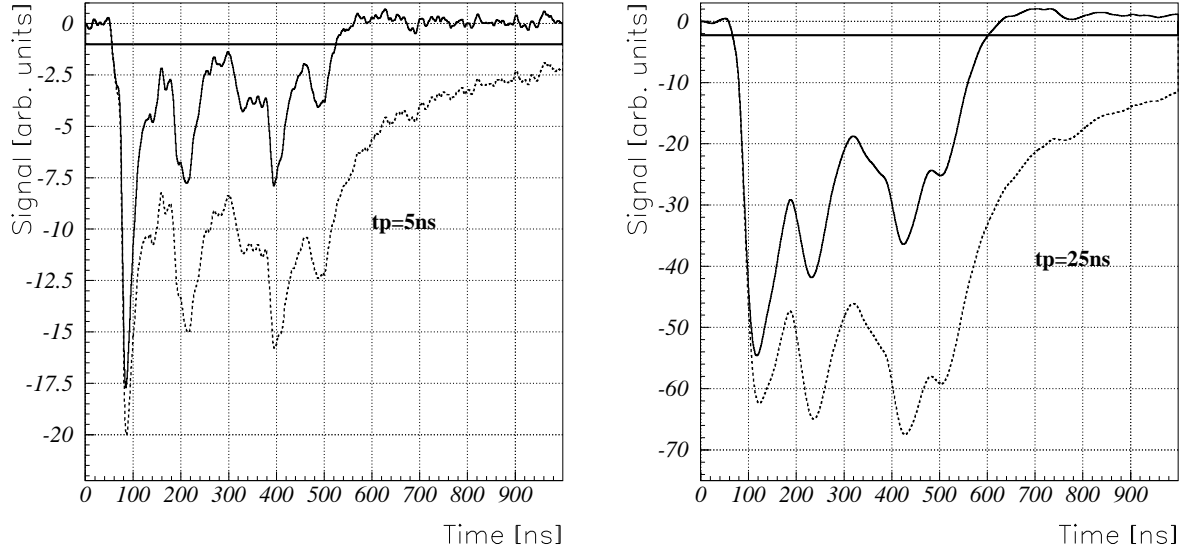


**Figure 3.13** : The two figures show the same induced current signal sent through preamps with  $tp=5ns$  and  $tp=25ns$ . The two pulse shapes in each figure show the electronics output without (dotted line) and with (solid line) tail cancellation. The horizontal line indicates the threshold level.

### 3.2.4 Tail cancellation

The ions moving away from the anode wire induce a current signal which has approximately a  $(t+t_0)^{-1}$  form. Since this 'ion tail' would cause large dead times and signal 'pile-up' one has to differentiate the signal to restore the baseline quickly. Fig. 3.13 shows an example of the electronics output with and without tail cancellation.

Two commonly used filter circuits, a pole/zero and a zero/pole filter are shown in fig. 3.14. The transfer functions for these two networks are

$$f_1(s) = \frac{s + \frac{1}{\tau_1}}{s + \frac{1}{\tau_2}} \quad \begin{array}{l} \tau_1 = R_1 C \\ \tau_2 = \frac{R_1 R_2 C}{R_1 + R_2} \\ \tau_1 > \tau_2 \end{array} \quad \text{and} \quad f_2(s) = \frac{R_1}{R_1 + R_2} \times \frac{s + \frac{1}{\tau_1}}{s + \frac{1}{\tau_2}} \quad \begin{array}{l} \tau_1 = R_1 C \\ \tau_2 = (R_1 + R_2) C \\ \tau_1 < \tau_2 \end{array} \quad (3.13)$$

Sending a  $e^{-\frac{t}{\tau_1}}$  signal through such a filter results in an output  $\propto e^{-\frac{t}{\tau_2}}$ , so we see that a pole/zero filter shortens the signal tail while a zero/pole filter attenuates it and makes the tail longer. For tail cancellation we therefore use a pole/zero filter.

Since the MDT signals are not of an exponential form but of the form  $s(t) = (t+t_0)^{-1}$ , more than one filter is needed. For this simulation a  $2 \times$  pole/zero network was used. The optimization of the time constants for such a double filter is described in [21].

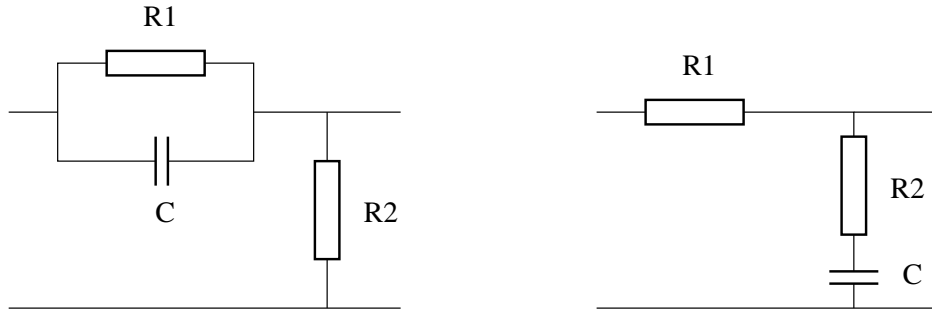


**Figure 3.14** : Pole/zero and zero/pole filters are commonly used circuits for signal shaping.

Since the signal shape depends on the position of the track along the wire one has to decide for which impact parameter one wants to adjust the filter constants.

Adjusting the filter constants for the termination resistor side causes over compensation for a signal close to the preamp side. The result is considerable undershoot of the signal (fig. 3.15). Adjusting the filter constants for the preamp side results in undercancellation  $\rightarrow$  baseline shift  $\rightarrow$  pile up, which is intolerable for the low thresholds we need to use (fig. 3.15).

**We have to adjust the filter constants for signals from the termination resistor side.**

As a consequence the filters have to be adjusted differently for every tube length and in case of a change of gas or pressure all the constants have to be changed differently.

As we have seen before, the tube acts as a pole/zero filter (fig. 3.4). Adding a zero/pole filter one could cancel the tube transfer function for the terminator side. We would be left with the signal

$$s(t) = c_1 * \frac{1}{t + t_0} \quad (3.14)$$

for the far end of all tubes. The zero/pole time constants would stay fixed with the tubes and one could adjust the two pole/zero filters only for cancelling the  $\frac{1}{t+t_0}$  signal independently of the tube length in the whole system. However, this procedure would add some complication to the frontend and could be a source of errors.

Since the filters have programmable time constants it is more convenient to have an independent test setup with different tubes to determine the individual constants experimentally and to program them directly to the frontend.

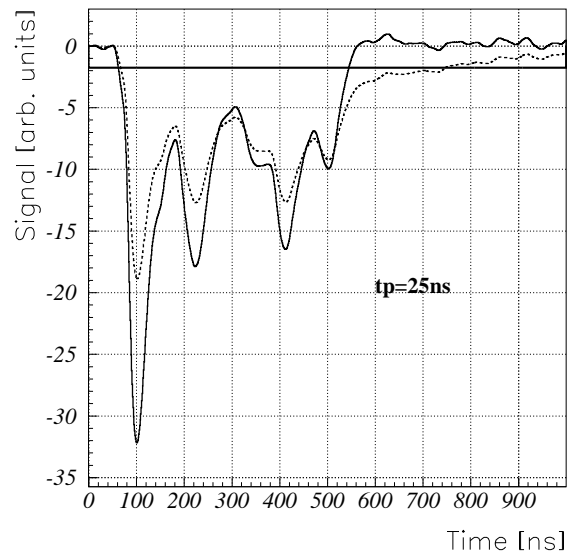
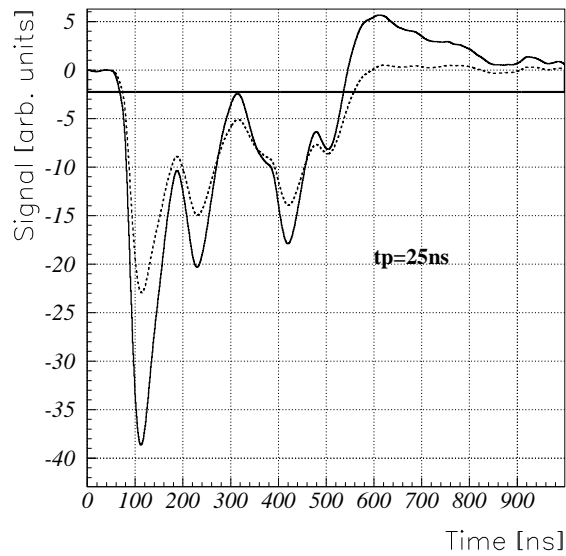


**Figure 3.15** : The same current signal induced on both ends of a 6m tube. In the left figure the filter constants are adjusted for the termination resistor side, in the right one for the preamp side. The signal close to the terminator shows attenuation (dashed line). Clearly we have to adjust for the termination end to avoid pileup.

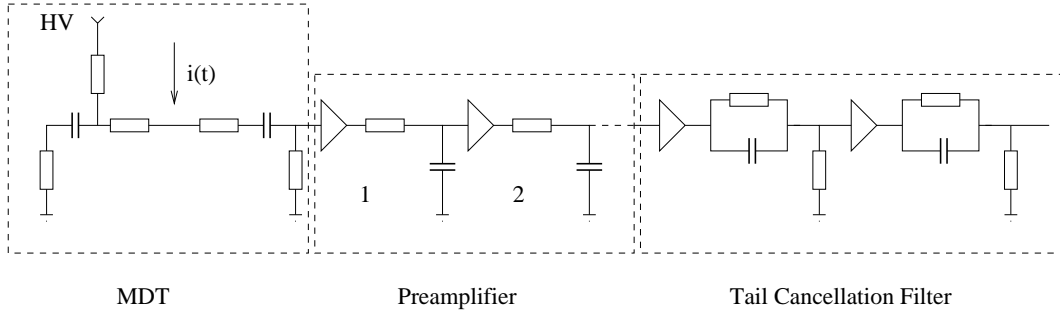


**Figure 3.16** : Model of the total frontend chain. The triangles indicate gain stages that decouple the individual parts.

### 3.2.5 Calculation of the electronics response

This section describes briefly the calculation of the electronics response for a given input signal. For non periodic signals the easiest way to calculate the electronics response  $s(t)$  is convoluting the input signal  $i(t)$  with the delta response  $f(t)$  of the system. The response  $s(t)$  is

$$s(t) = \int_0^t f(t-t')i(t')dt' \quad \text{or} \quad s_n = \sum_{m=1}^n f(t_n - t_m)i_m \times (t_m - t_{m-1}), \quad (3.15)$$

if the input signal  $i(t)$  is given as a table  $t_n, i_n$ . The response  $f(t)$  of the system to a delta function input is the inverse Laplace transform of the system transfer function  $g(s)$

$$f(t) = \frac{1}{2\pi i} \int_{-\infty}^{\infty} g(s)e^{st} dt \quad (3.16)$$

The explicit transfer functions and delta responses for our model of tube, preamp and filters (fig. 3.16) are the following:

Tube with loading resistor:

$$g(s) = \frac{s(b+as)}{e+ds+cs^2} \quad \rightarrow \quad f(t) = c_1e^{-\alpha t} + c_2e^{-\beta t} + k_2\delta(t) \quad (3.17)$$

$$\begin{aligned} k_1 &= \frac{b}{c} - \frac{da}{c^2} & k_2 &= \frac{a}{c} & k_3 &= \frac{ea}{c^2} & \alpha &= \frac{d}{2c} - \sqrt{\frac{d^2}{4c^2} - \frac{e}{c}} \\ \beta &= \frac{d}{2c} + \sqrt{\frac{d^2}{4c^2} - \frac{e}{c}} & c_1 &= \frac{k_1\alpha + k_3}{\alpha - \beta} & c_2 &= -\frac{k_1\beta + k_3}{\alpha - \beta} \end{aligned}$$

Tube without loading resistor and pole/zero, zero/pole filters:

$$g(s) = c_1 \frac{s + \frac{1}{\tau_1}}{s + \frac{1}{\tau_2}} \quad \rightarrow \quad f(t) = c_1 \left( \frac{1}{\tau_1} - \frac{1}{\tau_2} \right) e^{-\frac{t}{\tau_2}} + c_1 \delta(t) \quad (3.18)$$

Preamplifier:

$$g(s) = \frac{n! \tau}{(1 + s\tau)^{n+1}} \quad \rightarrow \quad f(t) = \left( \frac{t}{\tau} \right)^n e^{-\frac{t}{\tau}} \quad (3.19)$$

If we know the input signal at  $N$  discrete points in time, using (3.15) we have to evaluate  $N^2/2$  steps which can be quite time consuming. However if the delta response can be factorized i.e.

$$f(t_1 + t_2) = f(t_1)f(t_2) \quad (3.20)$$

which is the case for the exponential terms in (3.17) and (3.18) we can convert the sum in (3.15) into a recursive expression

$$s_n = \sum_{m=1}^n f(t_n - t_m) i_m \times (t_m - t_{m-1}) \quad \rightarrow \quad s_{n+1} = f(t_{n+1} - t_n) s_n + f(0) i_{n+1} \times (t_{n+1} - t_n) \quad (3.21)$$

which takes only  $N$  steps and speeds up the calculation significantly. The convolution method was used to study the dependence of the MDT performance on electronics parameters. For comparison of measured pulse shapes with simulated ones the preamplifier used in the experiment was simulated using PSPICE [19].

# Chapter 4

## Comparison of simulated signal shapes with measurements

In order to verify the simulation model described in the previous chapter, a series of comparisons with measurements was performed. The first test was a quantitative comparison of measured MDT signals with the result of the simulation model.

### 4.1 Setup and electronics simulation

The setup for the MDT signal recording can be seen from fig. 4.1. A chamber with 32 tubes built at NIKHEF [22] was set up in the M2 test beam area in 1995 [30]. One tube was read out with a LECROY digital scope [23]. The hardware and operating parameters were the following:

setup parameters	
wire diameter	$50\mu m$
inner tube radius	1.475cm
tube wall thickness	$250\mu m$
tube length	30cm
gas	$Ar/N_2/CH_4 91/4/5$
pressure	3 bars absolute
flow rate	1l/h
muon energy	170 GeV
preamplifier	L3 preamplifier [24]
peaking time	4ns
scope sampling frequency	500 MHz (2ns time bins)



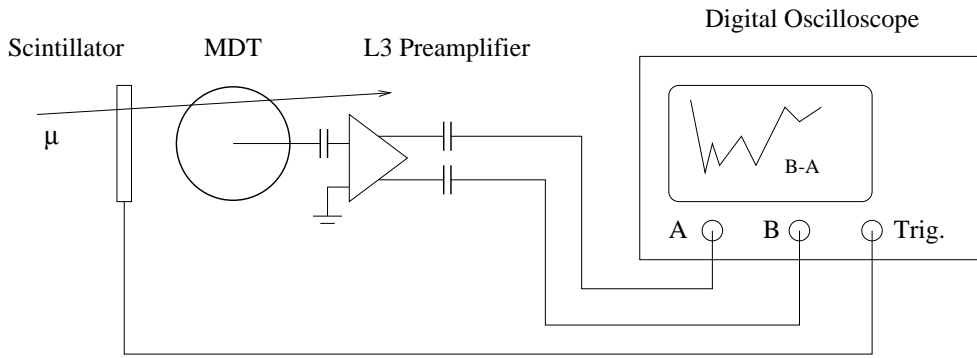


**Figure 4.1** : Setup for recording of MDT signals.

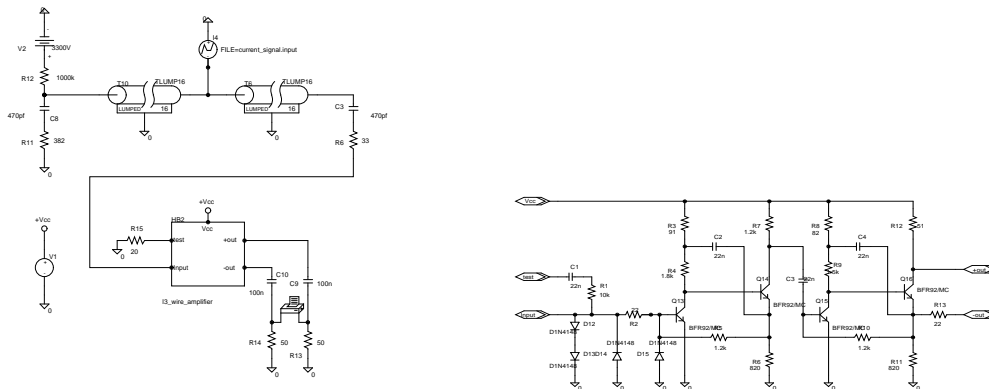


**Figure 4.2** : PSPICE schematic for simulation of the MDT and the preamplifier of the setup shown in fig. 4.1.

The simulation of the signal induced on the wire was done with GARFIELD as described before, the simulation of the MDT and the preamplifier was done with PSPICE in sufficient detail in order to avoid any free parameters (fig. 4.2). Fig. 4.3 shows the system response to a delta pulse injected on the wire and the comparison of the measured and the simulated response to a step function injected on the termination resistor end of the tube.

The induced current signal from GARFIELD was input to the circuit as an ideal current source on the wire and a transient analysis was done in PSPICE. The output could then directly be compared to the signals measured with the oscilloscope.

The analysis of the signal shapes consisted of two different aspects: The first quantity of interest is the shape of a signal created by a single charge deposit in the MDT. The other important aspect is the overall shape of the signal from a muon track which is dominated by the statistics of the charge deposit along the track.

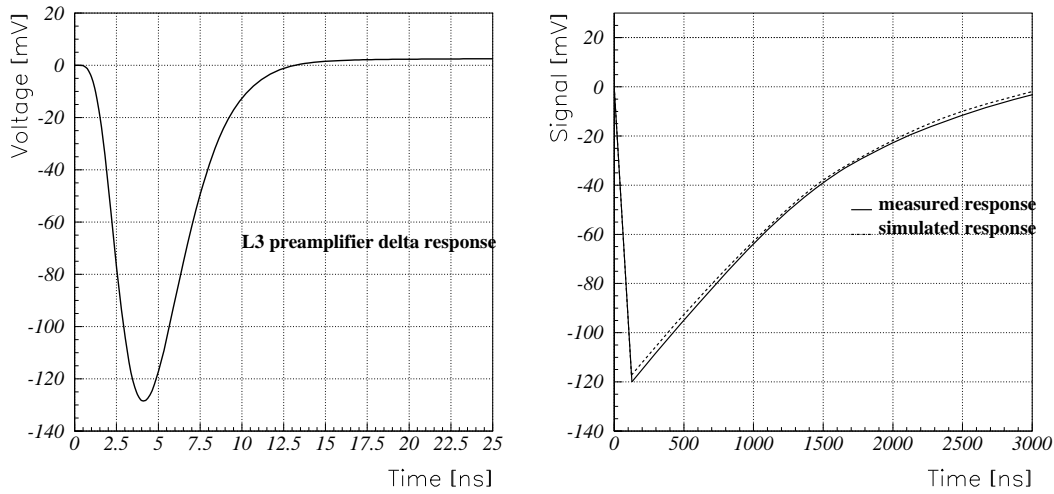


**Figure 4.3** : Delta response of the system simulated with PSPICE and comparison of the response to a step function injected on the termination resistor side. As one can see the PSIPCE model matches the measurements nicely.

The single electron response was studied using signals from an Fe55 source. This source emits photons with an energy of 5.9 keV. The effective ionization potential of Ar is 26eV; most Fe55 photons leave a localised cluster of 226 electrons in the MDT.

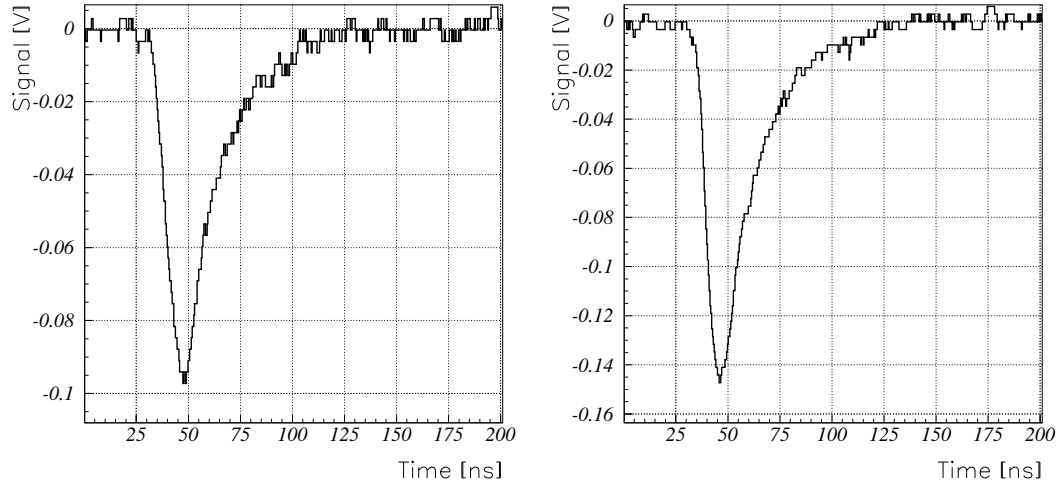
For studying the ionization distribution along the muon track the signals from 170 GeV muons were compared to the simulation.

## 4.2 Fe55 signals

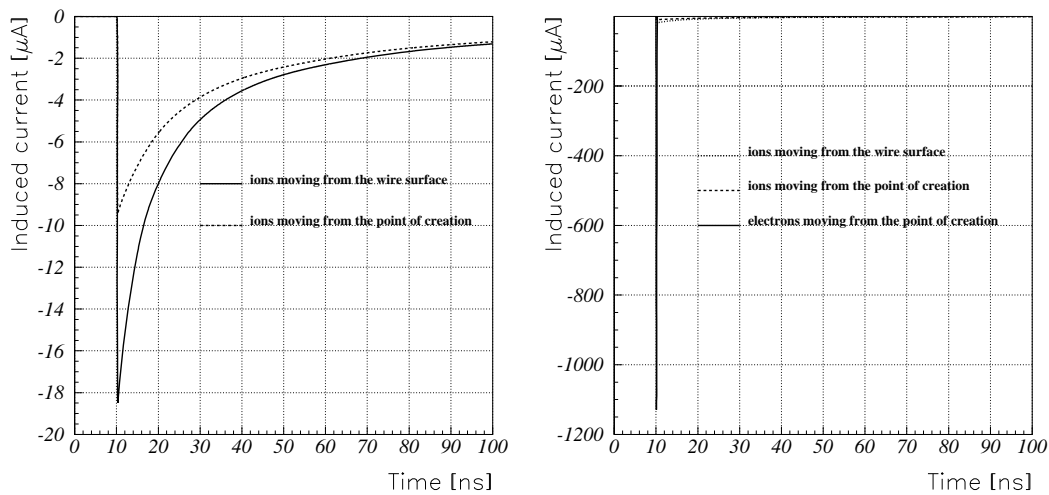
Fig. 4.4 shows some examples of measured Fe55 pulses. The pulse height variation depends on the gas gain fluctuations and due to diffusion also on the distance of the photon conversion from the wire. To account for this in the simulation, clusters of 226 electrons were put to random positions in the MDT. Fig. 4.5 shows the current signals induced on the wire as calculated with GARFIELD. Tracking the ions from their point of creation gives a significantly lower pulse compared to the model assuming the ions to move from the wire surface. The electron component of the signal is large but very short, so the total induced charge is low compared to the total charge induced by the ions, but it still gives a significant contribution to the signal shape in the first 100-200ns. The current signals calculated with the different models were sent through the preamplifier using PSPICE.

Fig. 4.6 shows a comparison of averaged simulated and measured signals. The agreement of the pulse heights and the tails of the averaged pulse shapes is quite poor.

The model neglecting the electron component and assuming all the ions being created at



**Figure 4.4** : Examples of measured Fe55 signals.



**Figure 4.5** : The left figure shows the induced current signal assuming the ions being created on the wire surface and a more realistic model taking into account the actual position of the ion creation. The right figure shows in addition the electron component of the signal calculated with GARFIELD.

the wire surface shows a tail that is falling off too slowly, the fact that the pulse heights agree for this model should be considered only accidental. Explaining the difference in the tail by assuming that the ion mobility is wrong is not reasonable since one would have to change the mobility by an unrealistic amount to match the results.

The model simulating the avalanche process in detail and tracking the ions and electrons from their point of creation overestimates the pulse height by far and shows a tail that drops too fast which suggest that the electron component is not modelled realistically. Nevertheless we see that the electron component causes the tail to fall off faster which would suggest that a realistic contribution of an electron component to the signal could explain the observed behaviour. If the simulated electron component of the signal would be a factor 3 lower the pulse height and the tail of simulated pulse would match the data.

One reason for the overestimation of the electron component could be the following: since in our model the electrons and ions are tracked according to the electric field given by the anode wire potential, the interactions of the drifting particles on each other are neglected. Taking into account the electrostatic repulsion of the ions would blow up the avalanche but it should not have a big impact on the induced current signal. The electron component however should be strongly affected by the mirror charge induced by the ions on the wire. According to GARFIELD simulations the ions are produced at an average distance of only  $2.7\mu m$  from the wire surface for our operating parameters. Although the avalanche starts much further from the wire ( $\approx 100\mu m$ ) the center of gravity of the ion cloud is shifted very close to the wire since the multiplication process is exponential. The electrons arrive within a time of 26ps rms, so the electron pulse is a very sharp spike. The electrons move between the ion cloud and the wire surface and they are strongly affected since the ion cloud induces a mirror charge on the wire and such reduces the electric field. The undisturbed electric field at the wire surface is  $2.2 \times 10^7 V/m$  for a voltage of 3500V. Assuming that the avalanche spread along the wire is  $\approx 100\mu m$  and  $\approx 20\mu m$  around the wire and modelling the effect of the ions by assuming a  $100\mu m \times 20\mu m$  'sheet' with a total charge of  $2 \times 10^4$  electrons at a distance of  $2\mu m$  from the wire we find a field of  $1.8 \times 10^7 V/m$  due to the induced mirror charge! The field created at the wire surface by the ions is comparable to the the field from the anode wire potential. This effect would certainly reduce the electron pulse component. The effect can be modelled by adding the field produced by the ions and their mirror charges to the undisturbed field and tracking the electrons according to this field. This procedure is currently being implemented into GARFIELD.

For all further studies the model tracing the ions from the wire surface was used and the tail was simply matched to the data by applying a pole/zero filter to the signals (fig. 4.7).

Since for lower gas pressure and thinner wires the ion and electron velocities are much higher compared to our parameters (3bars,  $50 \mu m$  wire), the discrepancy should be much more pronounced. Measurements for different pressures and wire diameters were not performed within this work.

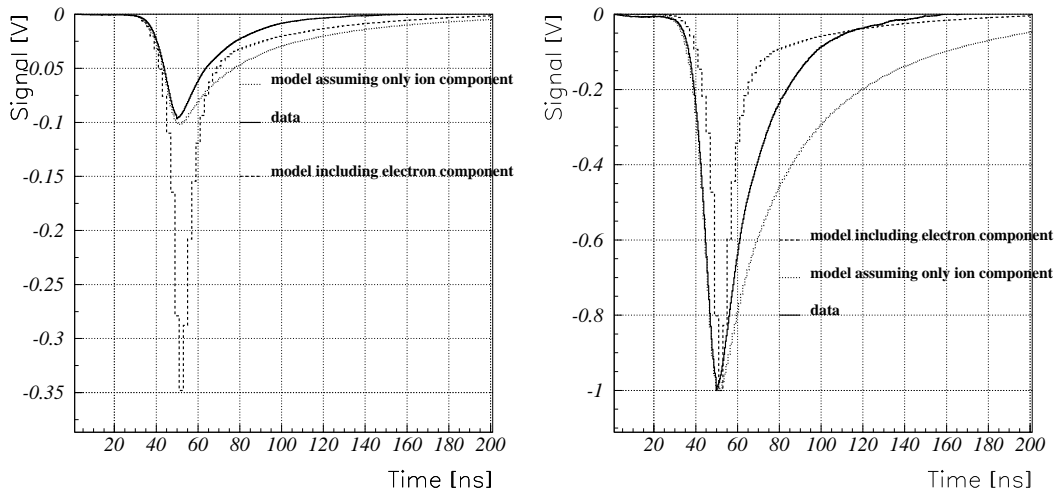


**Figure 4.6** : Comparison of simulated Fe55 signals with measurements. Neither the model assuming the ions moving from the surface nor the model including the electron component match the data well. In the right figure the pulses are scaled to the same height to compare the tail.

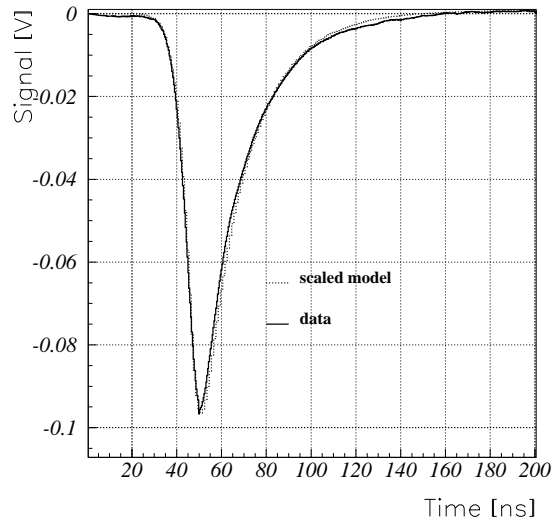


**Figure 4.7** : By sending the simulated signal through a pole/zero filter with time constants 60ns/30ns the simulated signal can be matched to the data.

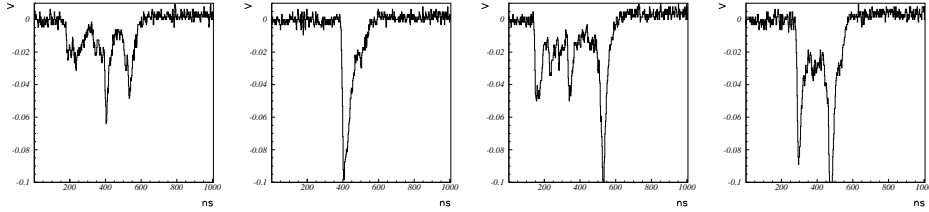


*Figure 4.8 : Examples of measured muon pulses.*

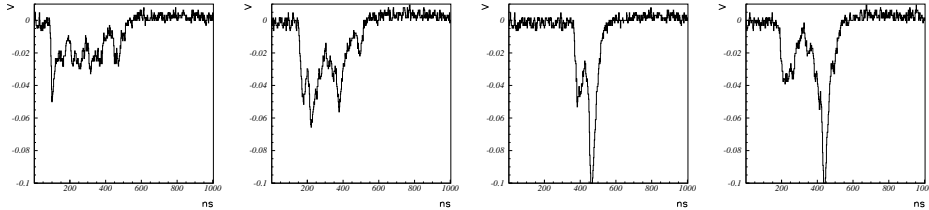


*Figure 4.9 : Examples of simulated muon pulses.*

### 4.3 Muon signals

In this section we will compare the signals from 170 GeV muons to the simulation. For this simulation the model assuming only the ions moving from the wire surface, neglecting the electron pulse will be considered. Fig. 4.8 shows examples of muon pulses recorded with the L3 preamplifier, fig. 4.9 shows muon signals simulated with GARFIELD, MAGBOLTZ, HEED and PSPICE taking into account the adjustment of the shape as described above. The noise was included to the simulation by overlaying measured noise samples to the simulated signal.

The 'spiky' shape of the signals is due to charge deposit fluctuations along the muon track. Fig. 4.10 shows the quantitative comparison of the pulse heights and the integrated signals. The agreement of measurement and simulation is quite good.

Another important quantity that will be of interest later is the leading edge charge of the signal. Fig. 4.11 shows a comparison of the leading edge charge i.e. the charge in a 25 ns gate following the threshold crossing time (threshold of  $5\sigma$  of the noise). Also there the agreement is quite good.

To quantitatively compare the signal structure, three different thresholds were applied to the signal and the width of the spikes as well as the gaps between the spikes were histogrammed for 430 measured and simulated signals (fig. 4.12). The shape of the distribution as well as the absolute number of hits are in excellent agreement (fig. 4.13).

Finally we can compare the trailing edge resolution. Since the trailing edge of the signal is due to the electrons created close to the tube wall the trailing edge has a fixed time

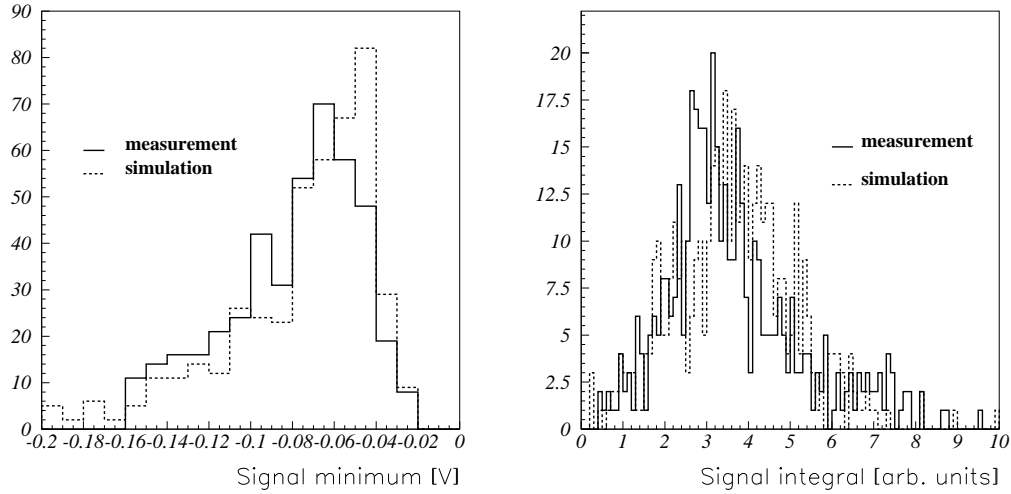


**Figure 4.10 :** The distribution of the signal minima and the integrated signal shows quite good agreement between measurement and simulation.

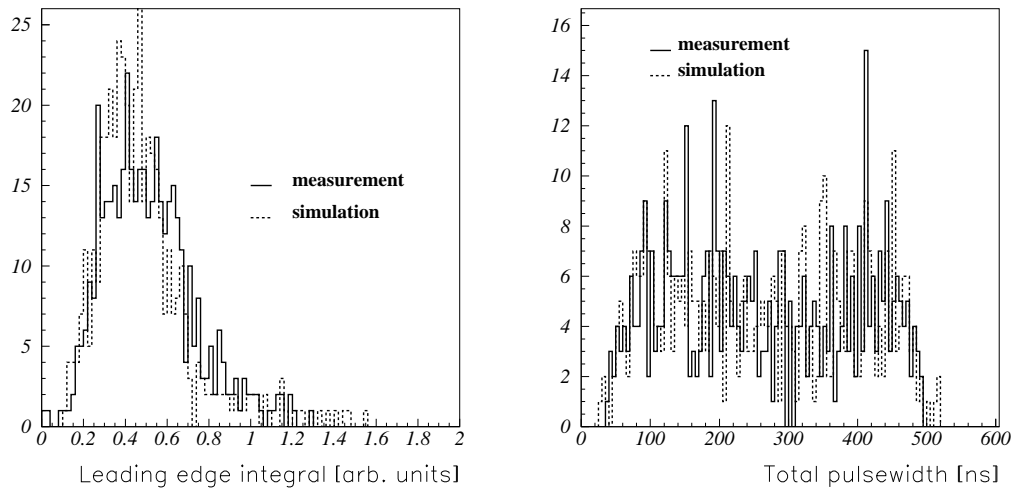


**Figure 4.11 :** The left histogram shows the comparison of the leading edge charge of the signal. The right figure shows a comparison of the pulsewidth. The agreement is quite good.

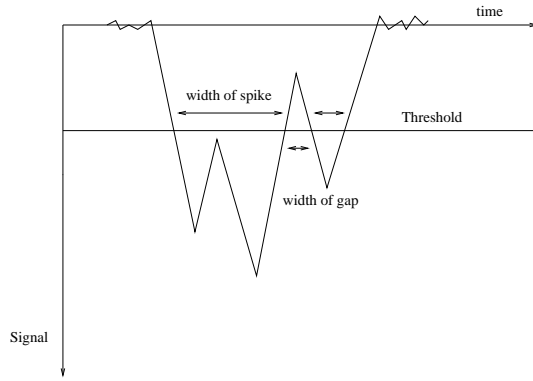


**Figure 4.12** : To quantitatively compare the signal structure, the width of the spikes and the gaps between the spikes as defined in this figure were histogrammed.

relation with respect to the muon arrival time (fig. 4.14).

To conclude the comparison of measured and simulated signals we can state the following:

- The signal shape from a single cluster of electrons is not well simulated with the model assuming only ions moving from the wire surface according to the field dependent ion mobility. A model taking into account a detailed simulation of the avalanche process and the electron component of the signal fits the data even less. An overestimation of the electron component is likely to be the explanation of the discrepancy.
- After matching the signal tail to the data, the charge deposit, pulse height and signal structure from a muon track is in very good agreement with the simulation. We can conclude that the ionization fluctuations as well as the absolute amount of ionization are very well simulated by HEED.



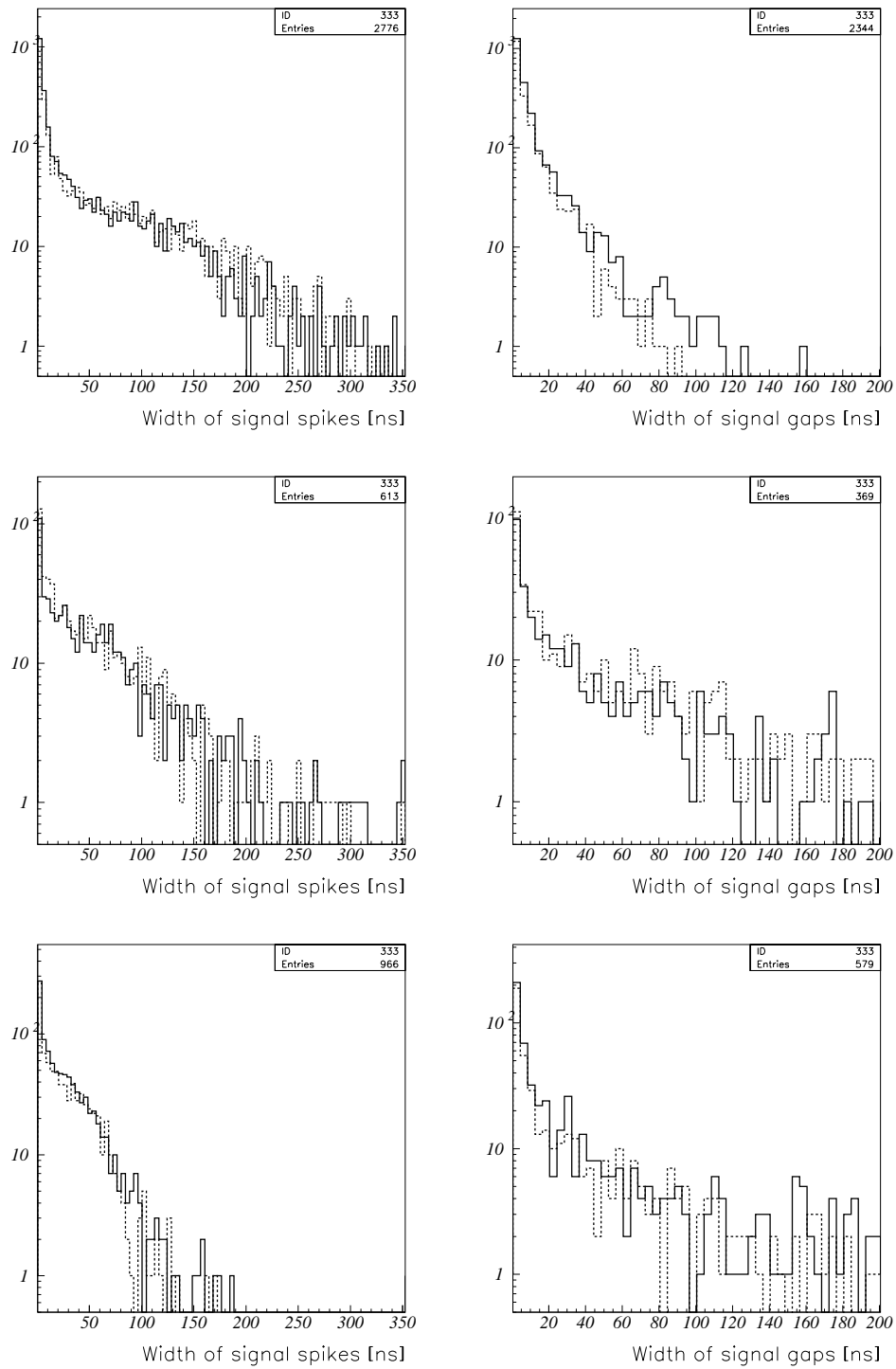


**Figure 4.13** : This figure shows the width of all spikes and gaps for 430 simulated and measured signals. The thresholds are 12mV, 25mV and 40mV for the 3 rows of figures. The absolute number of 'spikes' as well as the shapes of the distributions are in excellent agreement.

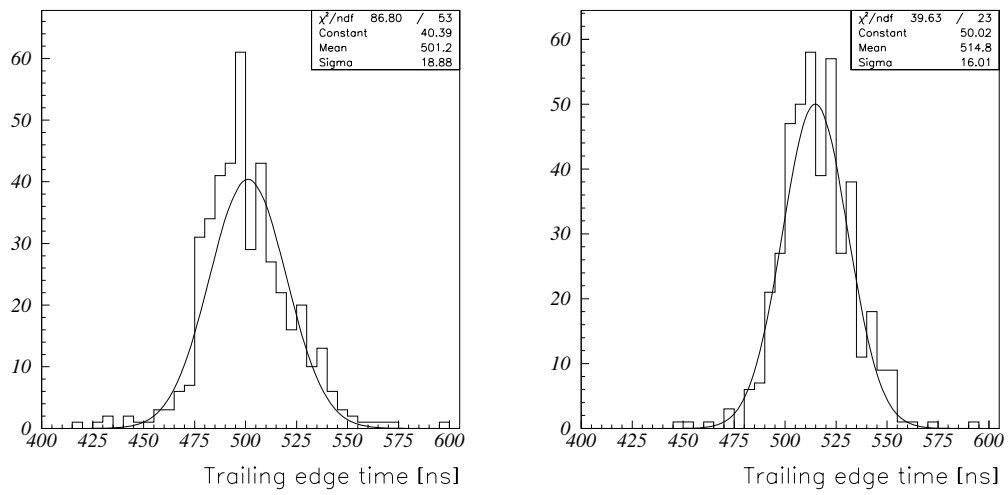


**Figure 4.14 :** The measured trailing edge time distribution (left figure) differs slightly from the simulated one (right figure).

# Chapter 5

## Comparison of the simulated MDT resolution with measurements

During summer 1995 and 1996 several MDT prototype tests have been performed in the M2 test beam area [30]. The detectors were placed in the halo of a high intensity muon beam. The average muon energy in the halo was 170 GeV.

Fig. 5.1 shows the setup for the spatial resolution measurement. Six single tubes with different wire diameters (30,40,50,70,100,160 $\mu m$ ) were placed between six planes of silicon telescope, two planes with strips perpendicular to the wire and 4 planes with strips parallel to the wire. The silicon telescope was able to measure the position of the muon track with an accuracy about 10 $\mu m$  at the tube position.

The single tubes were produced at the Max Plank Institute (MPI) Munich [31], the silicon telescope was provided by Munich University (LMU) [29]. The setup parameters are shown in table 5.1.

Only the data from the 50 $\mu m$  tube were analysed within this work. For the dependence of the resolution on the wire diameter see [32]. Since the FADC timing with respect to the trigger was not good enough the signal was split and sent to a discriminator and a TDC. The discriminator was set to the lowest possible threshold. The trigger time resolution was measured to be better than 400ps.

The pulse shapes recorded with the FADC are used to determine the charge of the signal and to find the hit time for thresholds different from the discriminator threshold. This was done the following way: the threshold set at the discriminator as well as a higher threshold were applied to the pulse shape in software. The time difference of the two threshold crossing times was then added to the TDC hit time.

The discriminator threshold was set to  $5\sigma$  of the noise. To calibrate the threshold an Am source (60 keV photons) together with a Mb foil (17.2 keV fluorescence line) was used. The 17.2 keV photons create a cluster of around 662 electrons (the effective ionization potential

setup parameters	
inner tube radius	1.46cm
wall thickness	400 $\mu$ m
tube length	1m
gas	Ar/N <sub>2</sub> /CH <sub>4</sub> 91/4/5
pressure	3 bars absolute
flow rate	1l/h
preamplifier	BNL preamp [28]
preamp peaking time	15ns
FADC sampling freq	250 MHz
FADC dynamic range	7 bits 0-2V
silicon strip pitch	50 $\mu$ m
number of strips per plane	1024
resolution at tube position	10 $\mu$ m
muon energy	170 GeV

Table 5.1: Setup parameters.

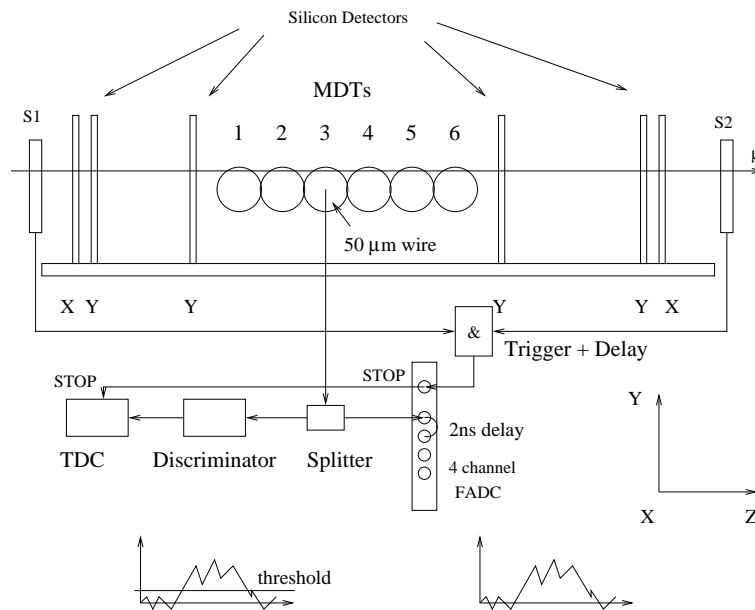
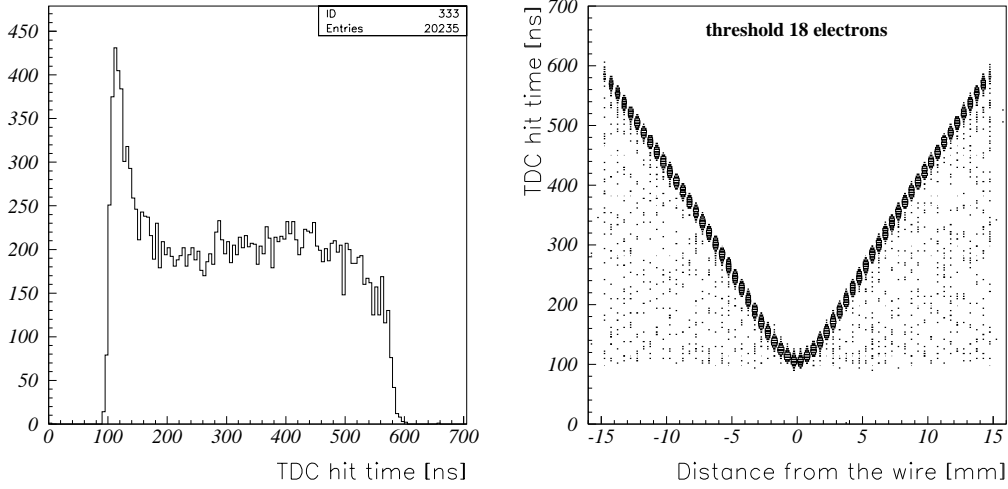


Figure 5.1 : Setup for the resolution measurement in the 1996 test beam.



**Figure 5.2** : TDC spectrum and TDC hits versus track position.

for Argon is 26eV). Dividing the peak of the photon pulse by 662 yields the pulse height for one ionization electron. The calibration was done with a pulse height analyser and showed that the  $5\sigma$  noise level corresponds to a threshold of 18 primary electrons for a gas gain of  $2 \times 10^4$  which is in very good agreement with the simulations assuming that the termination resistor is the main source of noise.

Fig. 5.2 shows the drift time spectrum (TDC spectrum) as well as the TDC time versus the track position obtained by the silicon telescope. The hits 'below' the two rt-relation bands are due to delta electrons created by the muon in the tube wall or the counting gas. A detailed study of these effects is given in chapter 12.

The rt-relation and the resolution are found the following way:

1. To get rid of the delta electron hits all the hits outside  $5rms$  of the average time in a position slice are thrown away.
2. The hit times are averaged in  $1mm$  position slices which yields a first order rt-relation.
3. A fourth order polynomial is fit to the central part of the rt-relation ( $\pm 3mm$  around the 'lowest' point) and the minimum of the curve yields a first order wire position.
4. The wire position is subtracted from the individual positions and procedures 2 and 3 are repeated. This iteration is done until there is no more significant change of the wire position.
5. The difference of the position predicted with the silicon telescope and the position calculated from the hit time via the rt-relation is histogrammed and fit with a Gaussian in  $1mm$  slices in r (residuals). The  $\sigma$  of the Gaussian corresponds to the MDT

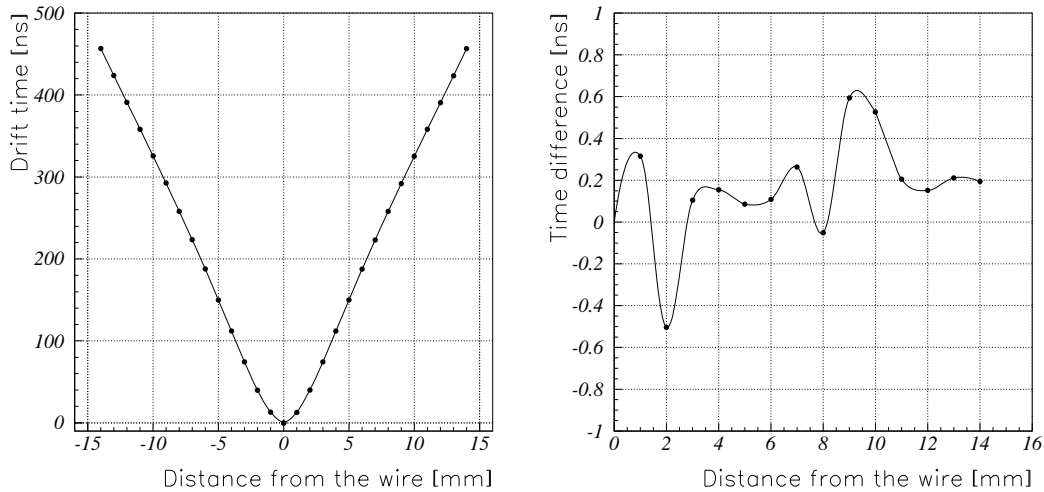


**Figure 5.3** : *Rt*-relation and time difference between the left and the right side.

resolution. Since the mean value of the Gaussian should be zero the *rt* relation is corrected by this value and the procedure is repeated until all the residuals are nicely centered around zero. The result is the *rt* relation and the radial dependence of the resolution.

Fig. 5.3 shows the *rt*-relation and the difference between the left and the right side. Fig. 5.4 shows a comparison of the simulated *rt*-relation compared to the measurement.

The radial dependence of the MDT resolution for four different thresholds together with the results of the simulation are shown in fig. 5.5. 16000 tracks with random distances from the wire were created in GARFIELD and traced as described in chapter 3.

The Monte Carlo data and the measurements were analysed with the same program. The solid lines in fig. 5.5 show the result using HEED for simulating the ionization along the muon track. The dotted line uses a cluster size distribution given by Lapique and Piuz [10]. We find that in most regions HEED fits the data best.

Fig. 5.6 and 5.7 show the comparison of the simulation to some other measurements done in 1996 and 1997.

We can conclude of the resolution studies for the  $Ar/N_2/CH_4 91/4/5$  gas mixture:

- The  $5\sigma$  noise level corresponds to a threshold of  $\approx 18$  primary electrons at a gas gain of  $2 \times 10^4$  which is in good agreement with the theoretical noise calculations.
- The *rt*-relation simulated with GARFIELD and MAGBOLTZ deviates from the measured one up to 6ns. Since for an average drift velocity of  $30\mu m/ns$  this corresponds

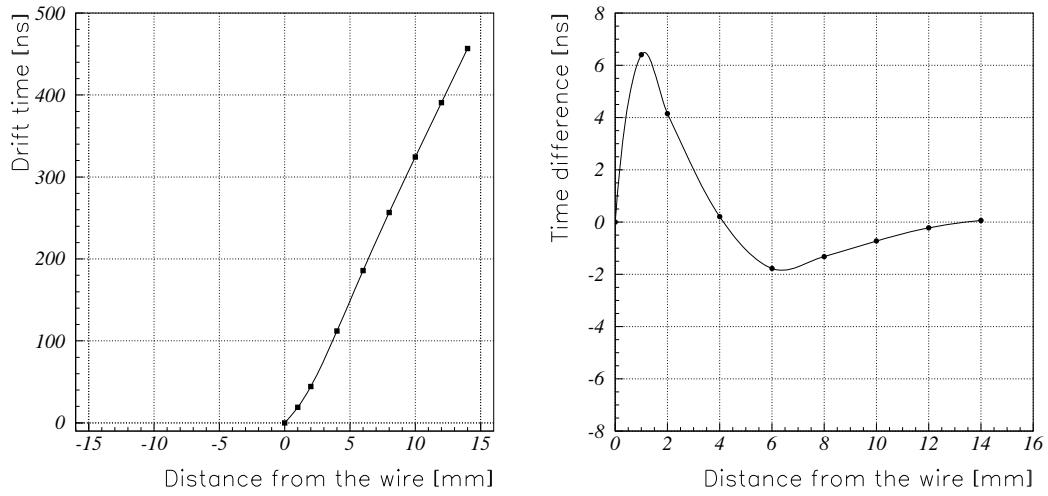


**Figure 5.4** : Simulated  $rt$ -relation and difference between the measured and simulated one.

to a systematic shift of  $180\mu m$ , we have to derive the final  $rt$ -relation from measurements and can not rely on simulation.

- The average resolution is  $\approx 80\mu m$  for a gas gain of  $2 \times 10^4$ .
- The GARFIELD simulation (using HEED to generate the ionization) matches the resolution curves very well.

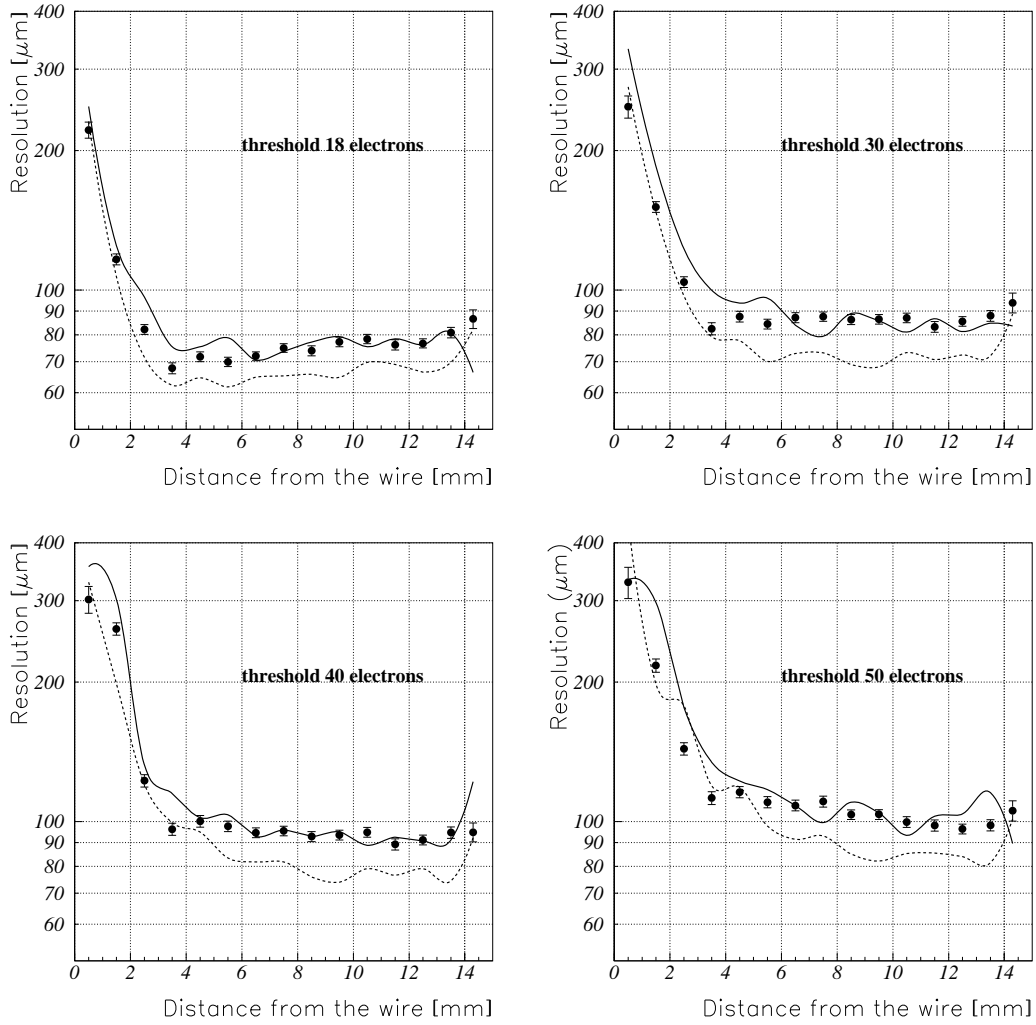


**Figure 5.5** : The radial dependence of the resolution compared to simulation. The points show the measurement results. The solid line is a simulation result using HEED to generate the ionization along the track. The dotted line shows a simulation using a cluster size distribution calculated by Lapique and Piuz [10]. The resolution is plotted on a log scale to show the decreased resolution close to the wire.



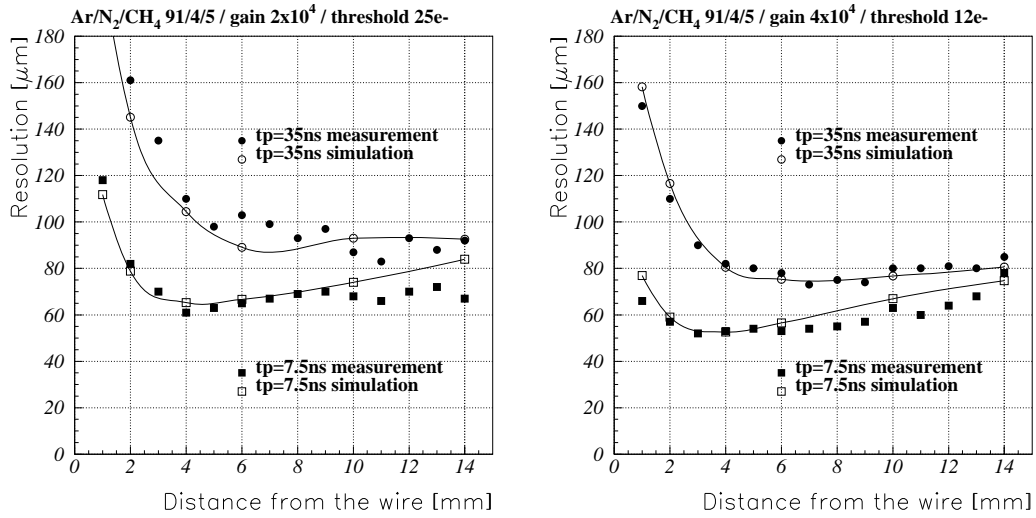


**Figure 5.6** : Measurements from the 1995 M2 testbeam compared to the GARFIELD simulation [25].

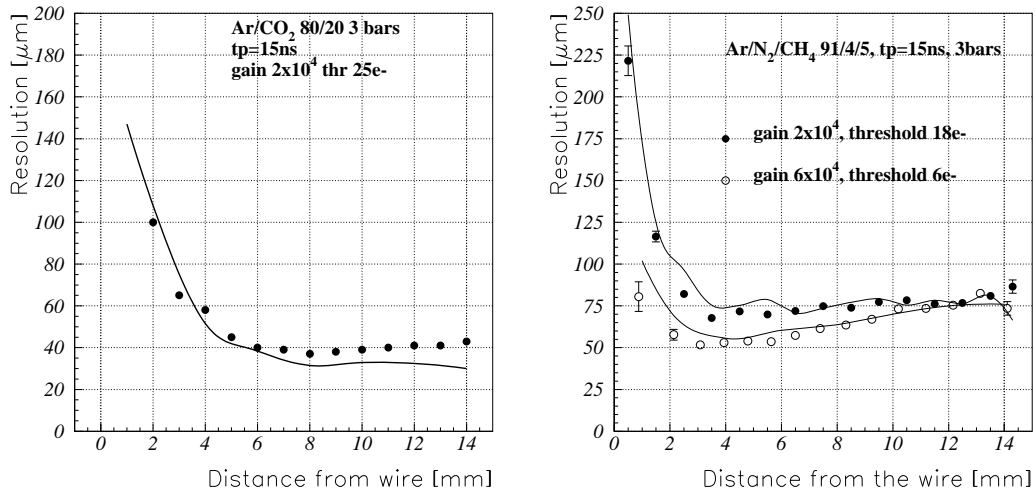


**Figure 5.7** : Measurements from the 1996 H8 testbeam [26] and the 1996 M2 testbeam [27] compared to the GARFIELD simulation. The points indicate the measurements, the lines show the simulation. The dependence of the resolution on gas gain and electronics parameters is discussed in the next chapter.

# Chapter 6

## Working point optimization

Knowing that we have developed a good understanding of the drift chamber processes we can explore a wide range of parameters like preamp peaking time, gas gain, pressure, thresholds and different gases in order to optimize our working point. We can also evaluate the individual contributions to the spatial resolution.

### 6.1 Dependence of the resolution on pressure

The first quantity of interest is the gas pressure. By increasing the pressure of the gas mixture, the contribution from diffusion, cluster position fluctuations and primary ionization fluctuations to the spatial resolution is decreased. Our goal of an average resolution of  $80\mu m$  will set the scale for the gas pressure. Two gases were studied:  $Ar/N_2/CH_4$  as an example of a fast and linear gas with a large diffusion coefficient and  $Ar/CO_2/80/20$  as an example for a slow nonlinear gas with a low diffusion coefficient. Certainly a fast, linear gas with low diffusion would be desired.

To perform the comparison by varying the pressure while keeping all other parameters fixed (threshold, gas gain etc.) may not be sufficient since different gas pressures might show the optimum performance for different parameters. We will perform the comparison the following way: since the aging problem i.e. the lifetime of the detector is one of the most important issues we will perform the comparison for the same total amount of charge deposited on the wire. Since we want to keep the charge deposit below  $1C/cm$  in 10 years of detector operation the baseline choice is a gas gain of  $2 \times 10^4$  for a pressure of 3 bars, so the resolution at this operating point is compared to a gain of  $6 \times 10^4$  at one bar and a gain of  $1.2 \times 10^4$  at 5 bars. The threshold is kept at the  $5\sigma_{noise}$  level since generally the resolution is best for the lowest threshold (see next section). The result of the comparison is shown in fig. 6.1.

We see that by keeping the amount of total charge deposited on the wire fixed, the resolu-

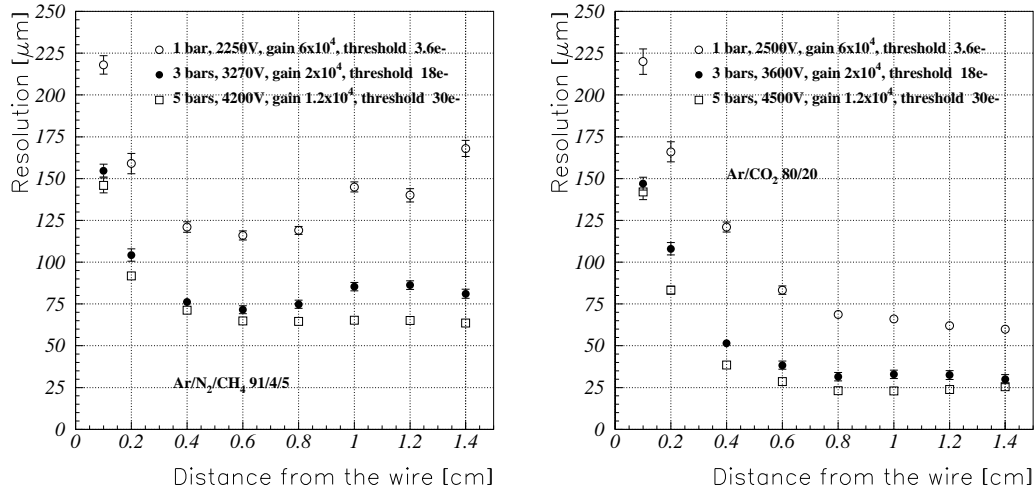


**Figure 6.1** : Keeping the total charge deposit constant, the resolution improves by increasing the pressure. Even a gas with a very low diffusion coefficient shows the required average resolution only if operated at increased pressure.

tion improves with pressure since the contributions from diffusion and primary ionization fluctuations are reduced. The  $Ar/CO_2$  mixture shows better resolution due to the low diffusion coefficient, but to arrive at the desired average resolution we still have to go to higher pressure, even for a gas with a diffusion coefficient as low as  $Ar/CO_2$ , in order to improve the resolution close to the wire. The resolution for the  $Ar/CO_2$  mixture will not improve by raising the gas gain since at a gain of  $6 \times 10^4$  the threshold is already very low in terms of primary electrons. However at a pressure of 3 bars the  $5\sigma_{noise}$  level corresponds to a threshold of 20 electrons (gain  $2 \times 10^4$ ), so by raising the gas gain to  $4 \times 10^4$  or  $6 \times 10^4$  we can improve the resolution as shown in the next section.

So we can conclude:

- A pressure of 3 bars is a good compromise in terms of resolution and total charge deposit.
- Keeping the total amount of charge deposited on the wire constant the resolution improves rapidly from 1 to 3 bars but only marginally by going to even higher pressure.
- Also for a gas with very low diffusion the resolution is limited by primary ionization statistics close to the wire and an average resolution of  $< 80\mu m$  is difficult to achieve at one bar.
- In terms of resolution the  $Ar/CO_2$  mixture shows better results compared to the  $Ar/N_2/CH_4$  mixture if the MDTs are operated at a low count rate. As shown in the next sections the  $Ar/CO_2$  mixture can not be used for high rate operation.

## 6.2 Contributions to the MDT resolution

In this section we will study the individual contributions to the MDT resolution for a gas pressure of 3 bars. The individual contributions like electronics noise, diffusion, gas gain fluctuations, cluster position fluctuations and charge deposit fluctuations were studied by performing a full chain simulation and 'switching off' the individual contributions while keeping all the others in the simulation.

Studying the effect of one single contribution by switching off all the other contributions does not make too much sense since the individual contributions do not add in quadrature to the total resolution. This is due to strong correlations of the individual contributions. The simulation showed that the combined effect from diffusion and charge fluctuations is bigger than the square sum of the individual effects. This can be understood from the fact that in case of large charge deposits there are also more electrons drifting to the wire, hence increasing the diffusion contribution. Also the contribution from noise is strongly correlated with the charge fluctuations which will be discussed below.

The following results were calculated for a gas pressure of 3bars, a preamplifier peaking time of 15ns ( $n=5$ ) and a threshold of 20 electrons ( $5\sigma_{noise}$  at a gain of  $2 \times 10^4$ ).

- **Gas gain fluctuations** have only a very small effect on the resolution since they are much smaller compared to charge deposit fluctuations.
- **Cluster position fluctuations** (fig. 6.2) affect the resolution only close to the wire since for large drift distances the charge focusing effect reduces the time separation of the individual clusters (fig. 12.4).
- **Diffusion** (fig. 6.3) has a major impact on the resolution for the  $Ar/N_2/CH_4$  91/4/5 mixture but only little impact on the resolution for  $Ar/CO_2$  80/20. The different diffusion coefficients for the two gases were already shown in fig. 3.3. Having switched off diffusion, the resolution difference is only due to the different drift velocities of the two gas mixtures.
- **Charge fluctuations** (fig. 6.4) have the biggest effect on the resolution by causing different signal rise times which results in time slewing. Also the reduced resolution close to the wire is due to charge fluctuations. As shown in the next section one can reduce this contribution by using fast electronics ( $t_p \approx 5$ ns) and low thresholds (2-5 electrons) and that a time slewing correction can improve the resolution. The performance of the time slewing correction depends critically on the noise.
- **Noise** (fig. 6.5) affects the resolution by imposing a lower limit on the threshold and directly by causing additional jitter of the threshold crossing time. The noise contributes less to the resolution of the  $Ar/CO_2$  mixture which is due to the lower drift velocity of this gas. The noise contribution is strongly correlated with the charge fluctuation contribution as shown in the next section. A small charge deposit results in a long rise time, so it delays the threshold crossing time but the noise shifts the

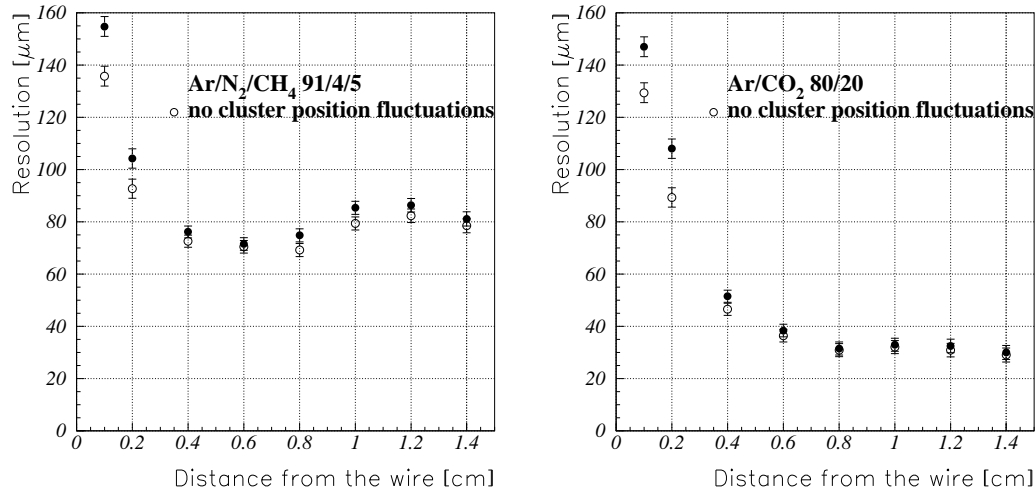


**Figure 6.2 :** The influence of cluster position fluctuations was studied by distributing the clusters with constant spacing along the particle track. Only close to the wire this contribution has an impact. The black points show the resolution including all components.

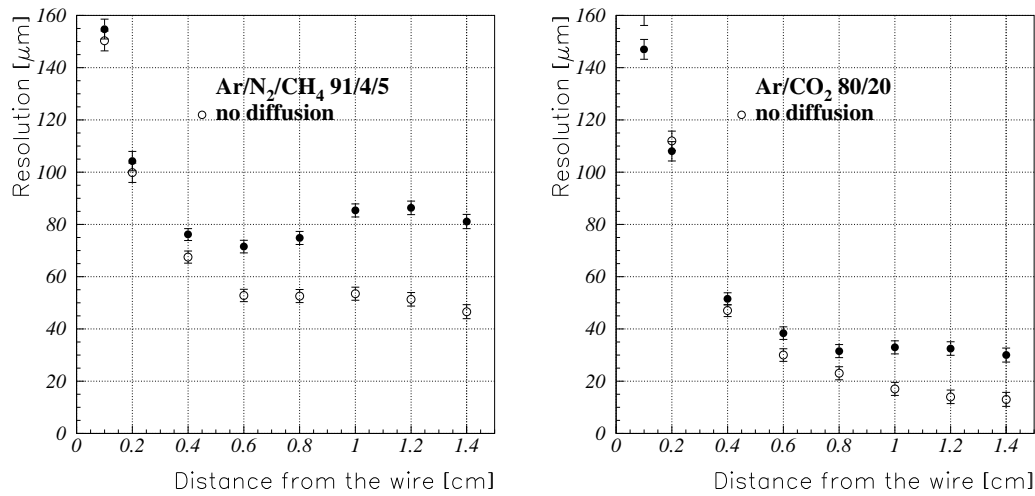


**Figure 6.3 :** Switching off the diffusion component in simulation shows that the contribution increases with the drift length as one would expect. The Ar/CO<sub>2</sub> gas shows very little diffusion at 3 bars. The black points show the resolution including all components.

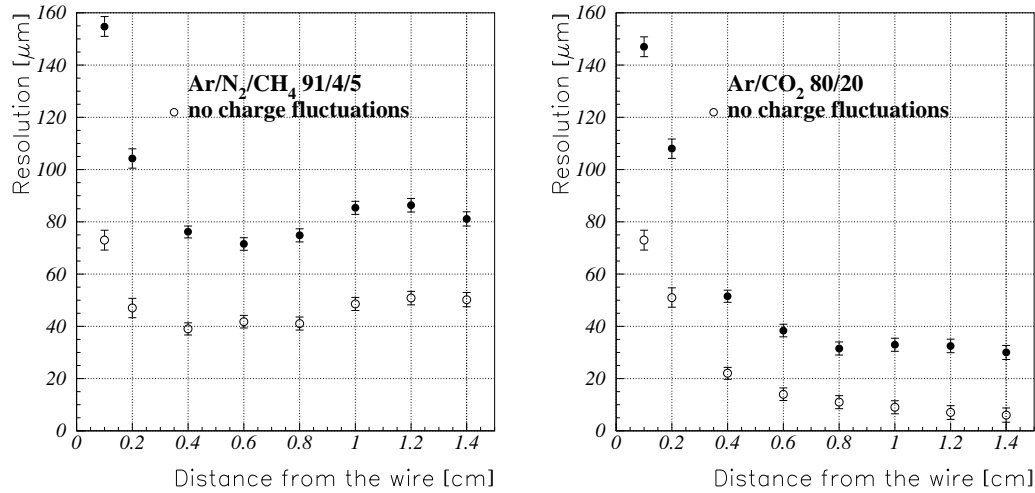


**Figure 6.4 :** The charge fluctuation contribution was studied by generating only clusters with three electrons (which is the average number per cluster). The charge fluctuations have the biggest impact on resolution for these operating parameters by causing time slewing effects. The black points show the resolution including all components.

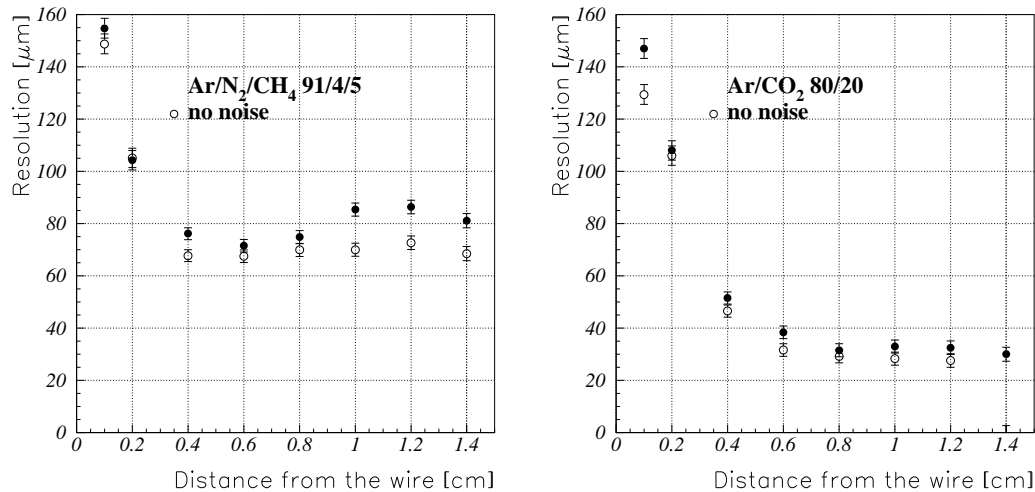


**Figure 6.5 :** The direct contribution from noise is smaller for the Ar/CO<sub>2</sub> mixture since the drift velocity is small. The black points show the resolution including all components.

threshold crossing on average to earlier times. For short signal rise times the shift is on average smaller, so the noise partially corrects for the time slewing. In case of large charge fluctuations the electronics noise reduces the time slewing effect by an amount that partially compensates the direct noise contribution. The contribution from noise is therefore partially hidden in the charge fluctuation contribution but it has a considerable influence if we want to perform a time slewing correction.

## 6.3 Resolution optimization

As shown in the previous chapter the ionization along the muon track is very well described by HEED. This program was interfaced to GARFIELD only recently. The following study was done in 1996 and the ionization was simulated using a cluster size distribution given by Lapique and Piuz [10]. Although the agreement with the measurements is not very good we are mainly interested in the influence of different parameters on the resolution which adequately described using this model.

To define the average MDT resolution one might fit a Gaussian to the residuals from all the distances. However, the residual distribution is not at all Gaussian, which is mostly due to the reduced resolution at distances  $< 2mm$ . Defining an average MDT resolution in this way is not appropriate since the actual value depends on the interval used for the fitting. Since for the optimizing process we are mainly interested in the differences in resolution for different parameters, we define the linear average of the resolutions from  $1mm$  to  $15mm$  as the quantity we want to optimize.

Fig.6.6 shows the average resolution for different peaking times, thresholds and relative noise levels. The figure shows that the resolution is affected by the gas gain only through the minimum threshold level that we can apply. The  $5\sigma$  noise level for a gas gain of  $2 \times 10^4$  is  $\approx 16$  electrons as shown in fig. 3.11. Raising the gas gain we can lower the threshold and improve the resolution. The comparison of the resolution for different noise levels at a certain threshold shows that the direct influence of the noise is quite small, e.g. for a peaking time of 15ns and a threshold of 20 electrons the difference in resolution for 'no noise' and the 'nominal noise' is only  $\approx 6\mu m$ .

The decrease in resolution by raising the threshold has two reasons: Using a high threshold one triggers on 'late' electrons which have a wider arrival time distribution compared to early electrons. The second and main effect is 'time slewing'. Because of charge fluctuations in the leading edge of the signal, the rise time of the signal varies. This results in different threshold crossings times and therefore degraded resolution. This is also the reason for the decrease in resolution for long preamp peaking times since long signal rise times result in increased time slewing.

The information about the time slewing is however still contained in the signal rise time. A classical constant fraction discriminator can not be used in our case due to the high noise level and the fact that a delay line is difficult to implement on an integrated circuit.

One can correct for the slewing effect by measuring the leading edge rise time and correcting for the time slewing offline. The rise time can be measured in two ways:

- applying 2 thresholds to the signal and taking the time difference as a measure of the rise time.
- measuring the leading edge charge with a short gate ADC ( $tp < gate < 2tp$ ).



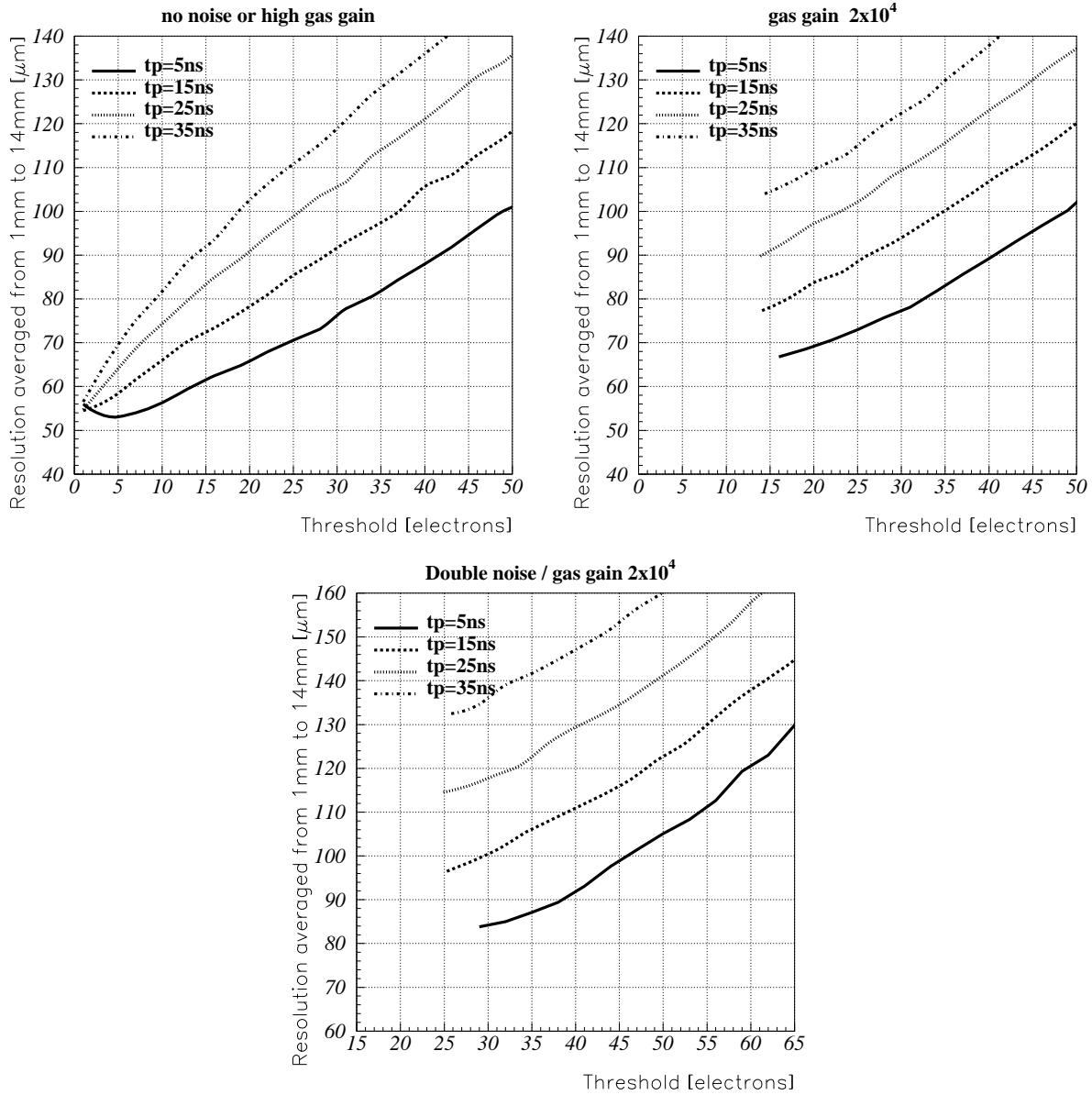


**Figure 6.6** : MDT resolution linearly averaged from 1mm to 14mm assuming different noise levels. We see that the resolution is good for fast preamplifiers and low thresholds. The noise affects the resolution mainly through the threshold limit. The direct influence of the noise is only small i.e. the resolution for the same threshold with and without noise is quite similar.

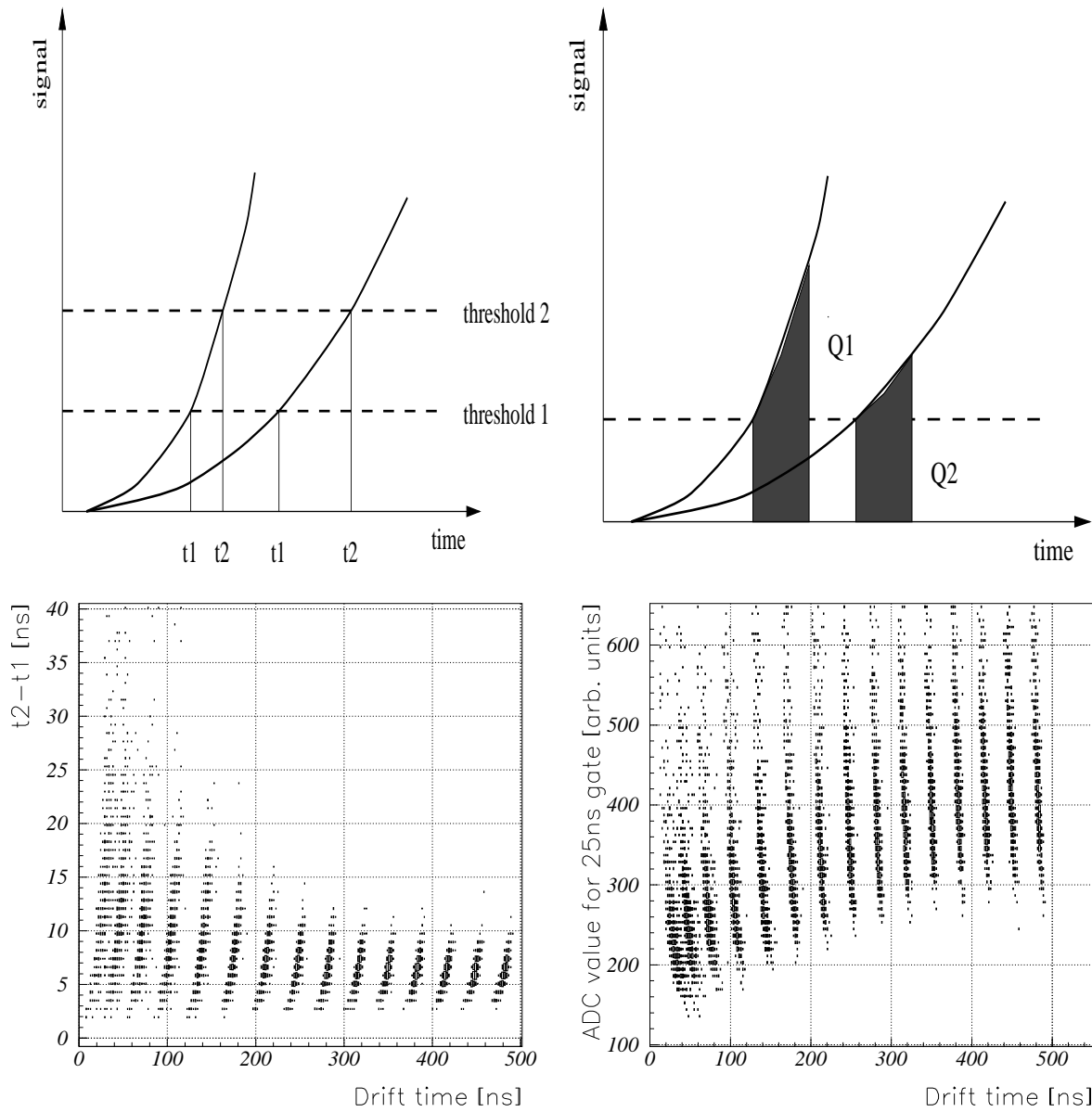
Fig. 6.7 shows the principle as well as some simulation results. The individual bands correspond to tracks generated at distances of 1, 2...14mm from the wire.

Fig. 6.8 shows the improvement in resolution applying a time slewing correction with a double threshold discriminator. Fig. 6.9 shows the improvement in resolution with a time slewing correction with a short gate ADC.

We see that for the 'no noise' case the dependence of the resolution on the peaking time and the threshold is reduced a lot and that the remaining threshold dependence is the component resulting from the arrival time statistics of the electrons. We also see that the time slewing corrected resolution is affected by the noise much more than the uncorrected resolution and also the loss in resolution for long peaking times can not be recovered. The reason for that can be seen in fig. 6.9. Since the signal rise time is smaller for long peaking times the time 'jitter' at the threshold level due to noise is bigger. We see that the slewing correction done with an ADC is more effective compared to the slewing correction with the double threshold discriminator.

We can conclude:

- The resolution is best for short peaking times and low thresholds.
- A time slewing correction helps to improve the resolution.
- The time slewing corrected resolution is strongly affected by the noise.



**Figure 6.7** : Correlation of threshold crossing time with the leading edge charge and the double discriminator time difference. The individual bands correspond to the distances 1mm, 2mm ...15mm. The uncorrected resolution at a certain distance is given by the projection of the distribution on the time axis. The time slewing corrected resolution corresponds to the width of the bands.

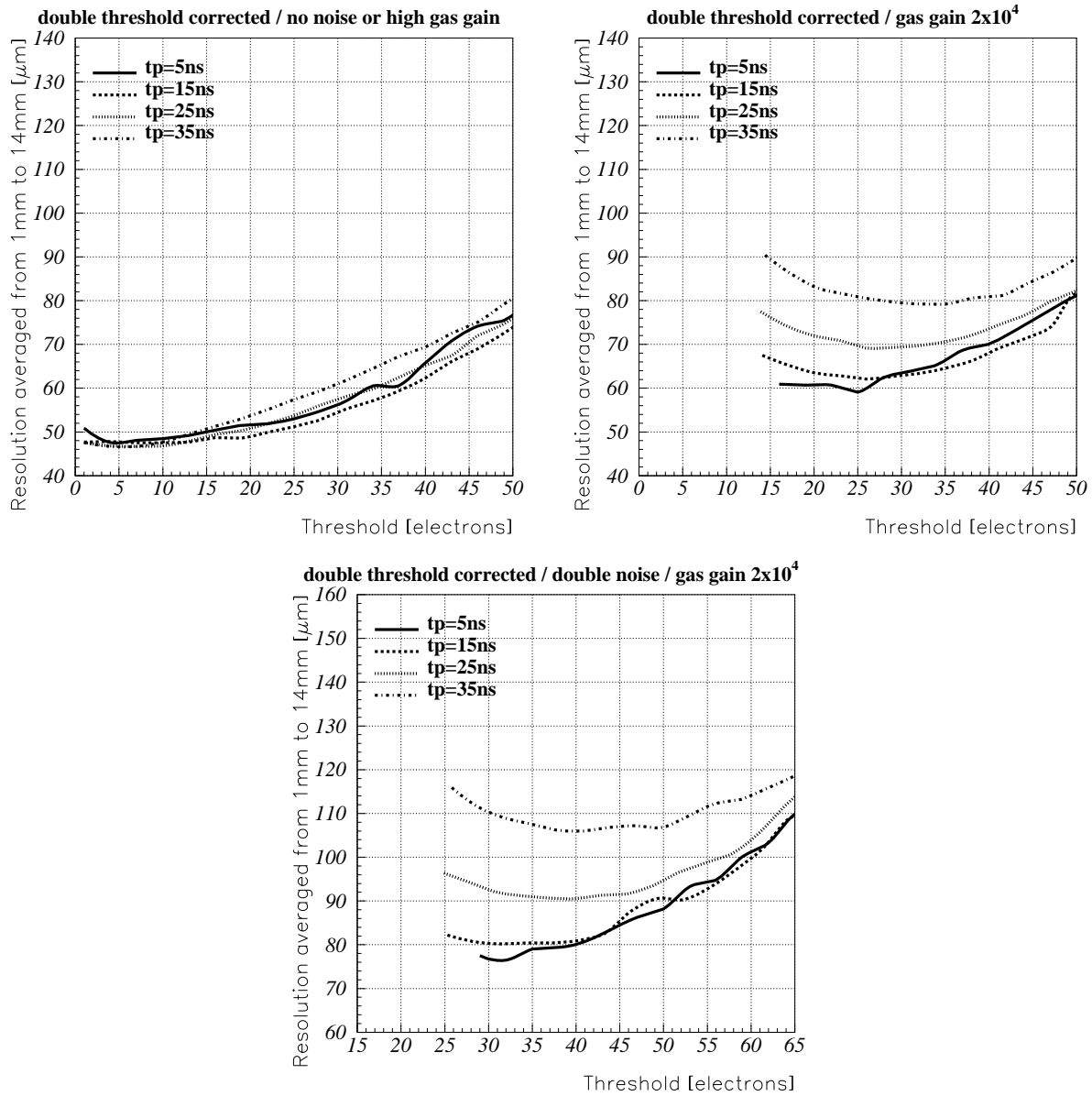


**Figure 6.8 :** Performing a time slewing correction with a double threshold discriminator one can improve the resolution and reduce the dependence of the resolution on peaking time and the threshold.

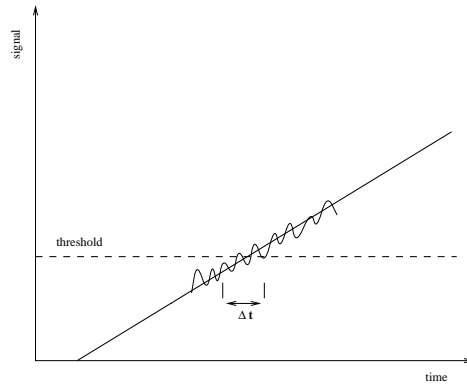
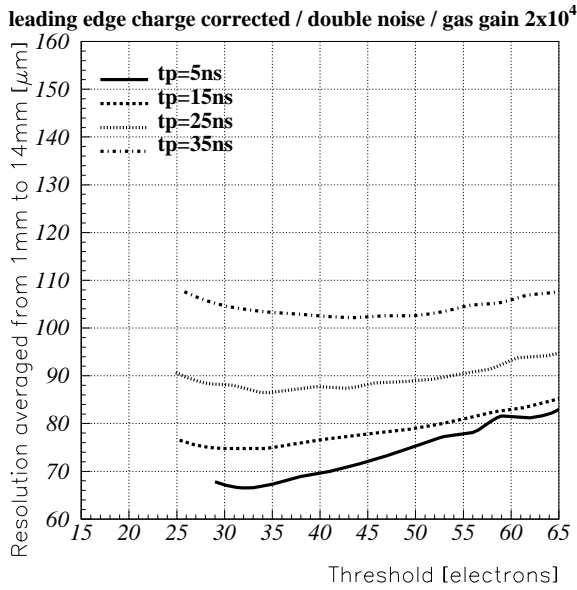
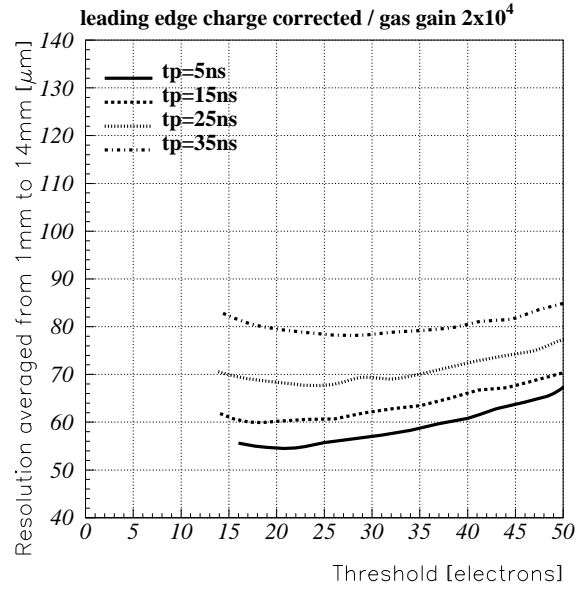
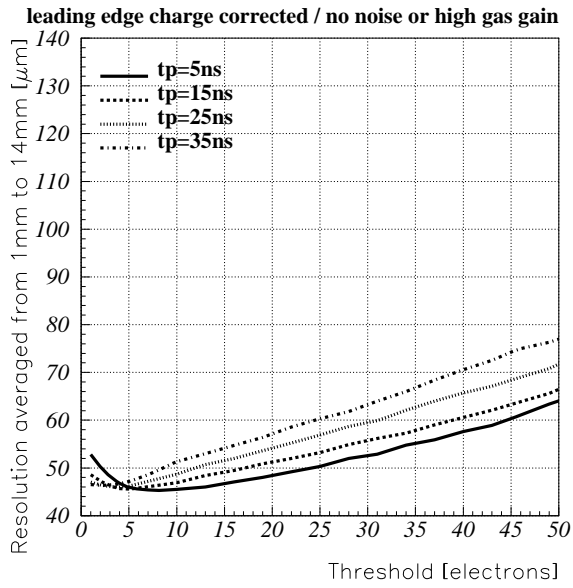


**Figure 6.9** : Performing a time slewing correction with a short gate ADC one can improve the resolution and reduce the dependence of the resolution on shaping time and threshold. The influence of noise on the time slewing corrected resolution is bigger for long preamp peaking times. From the last figure we can deduce that the time jitter from the noise for a slower rise time (long peaking time) is bigger since the intersection angle of the leading edge and the threshold becomes smaller.

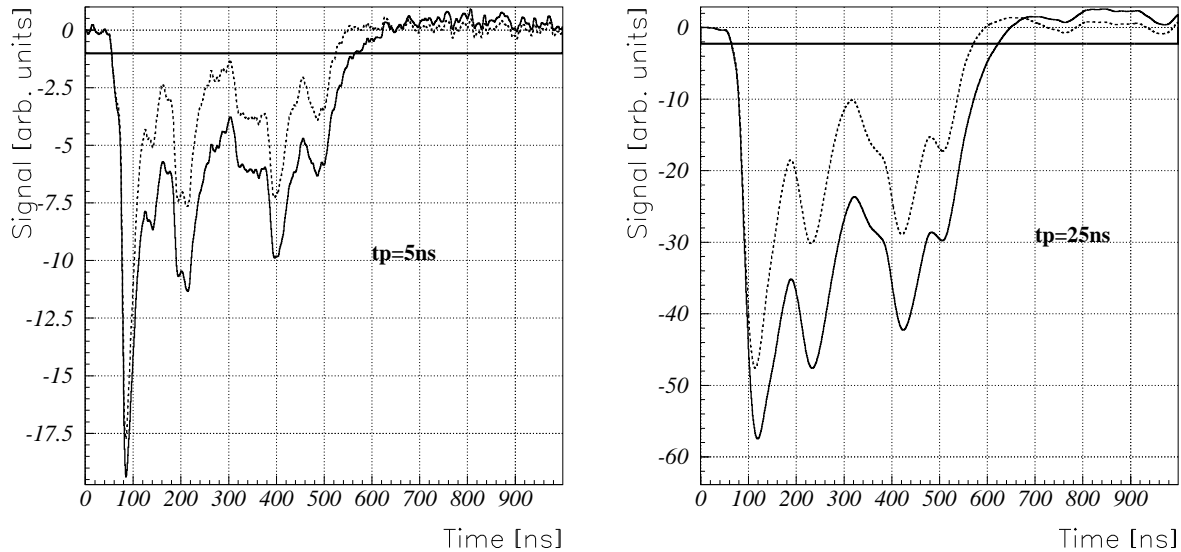


**Figure 6.10** : The same signal for 2 different sets of pole/zero constants. Cancelling the tail not so strongly reduces the number of hits but introduces dead time. One also can imagine that the trailing edge resolution will suffer since the intersection angle of the signal tail and the threshold becomes smaller.

## 6.4 Optimization of filter time constants

In case of a level 1 trigger in ATLAS, all tubes with at least one hit in the maximum drift time window are read out. To minimize the amount of data our aim is to get only one leading and one trailing edge per signal.

From fig. 6.10 we can immediately infer the general tendencies for different peaking times and filter constants. There is a threshold region with typically one threshold crossing per signal which becomes smaller for short peaking times. One can of course avoid multiple threshold crossings by using longer tail cancellation time constants, but this introduces additional dead time and also degrades the trailing edge resolution since the 'intersection angle' of the signal tail with the threshold becomes smaller.

We also have to keep in mind that signals from long tubes are attenuated because of the wire resistance and that they are shaped differently because of different transfer functions from different impact points. These two effects result in an effectively higher threshold and more threshold crossings ('hits').

For this study the following time constants were used for the double pole/zero network [21]:

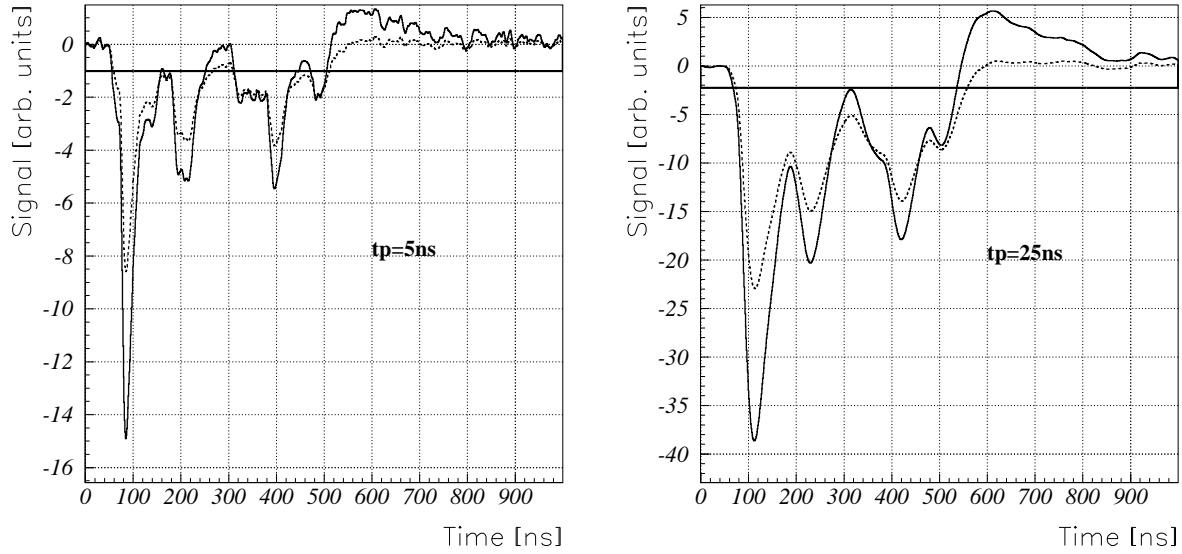


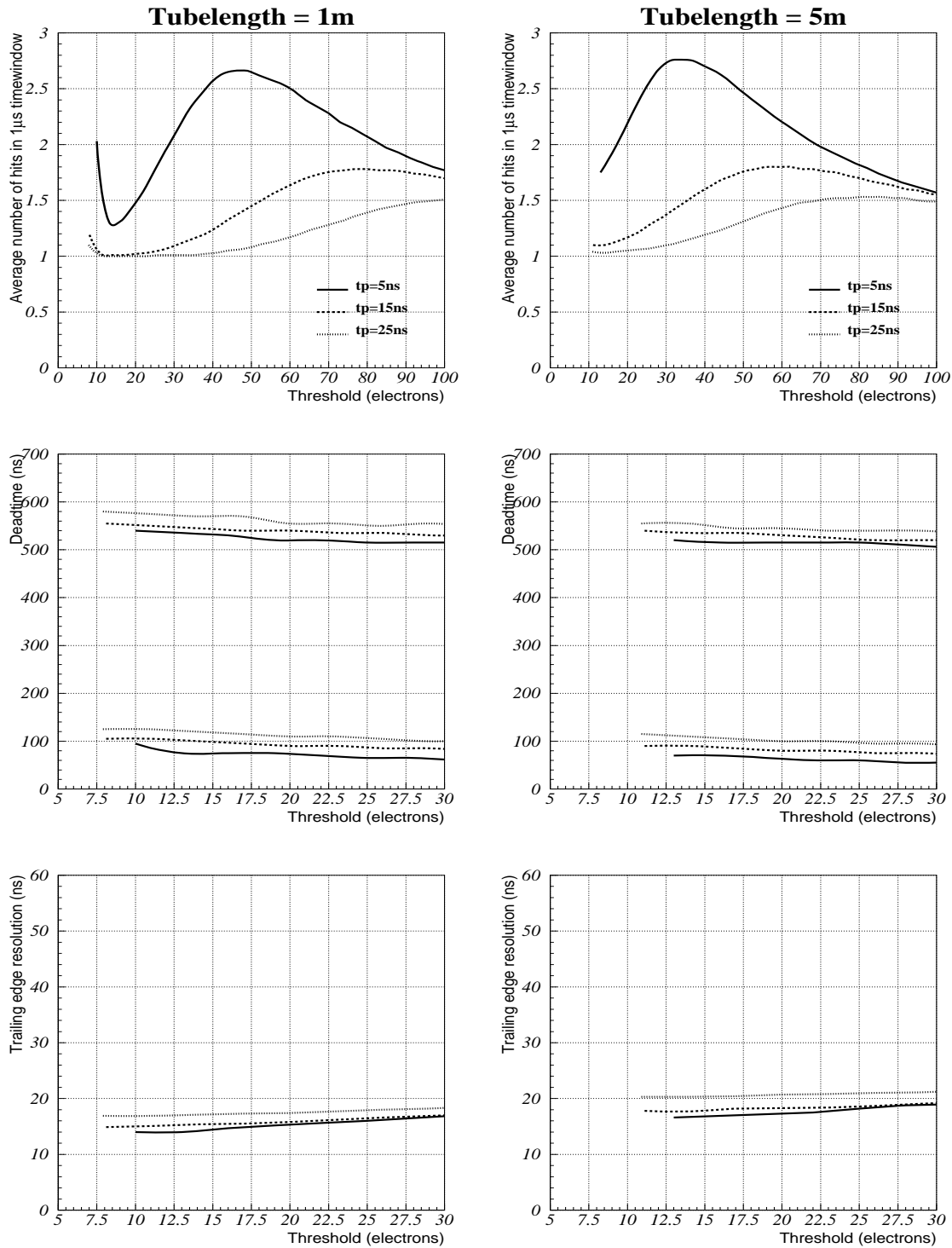
**Figure 6.11** : The same signal for muon impact on both ends of a 6m tube. The signal close to the terminator side (dashed line) is attenuated while the signal close to the preamp (solid line) side is overcompensated.

$$\begin{aligned}
 \tau_1 &= 133ns & \text{and} & & \tau_3 &= 1125ns \\
 \tau_2 &= 55ns & & & \tau_4 &= 587ns
 \end{aligned}
 \tag{6.1}$$

The average number of hits for tube lengths of 1m and 5m is shown in fig 6.12. The signals were randomly distributed over the whole length of the tube.

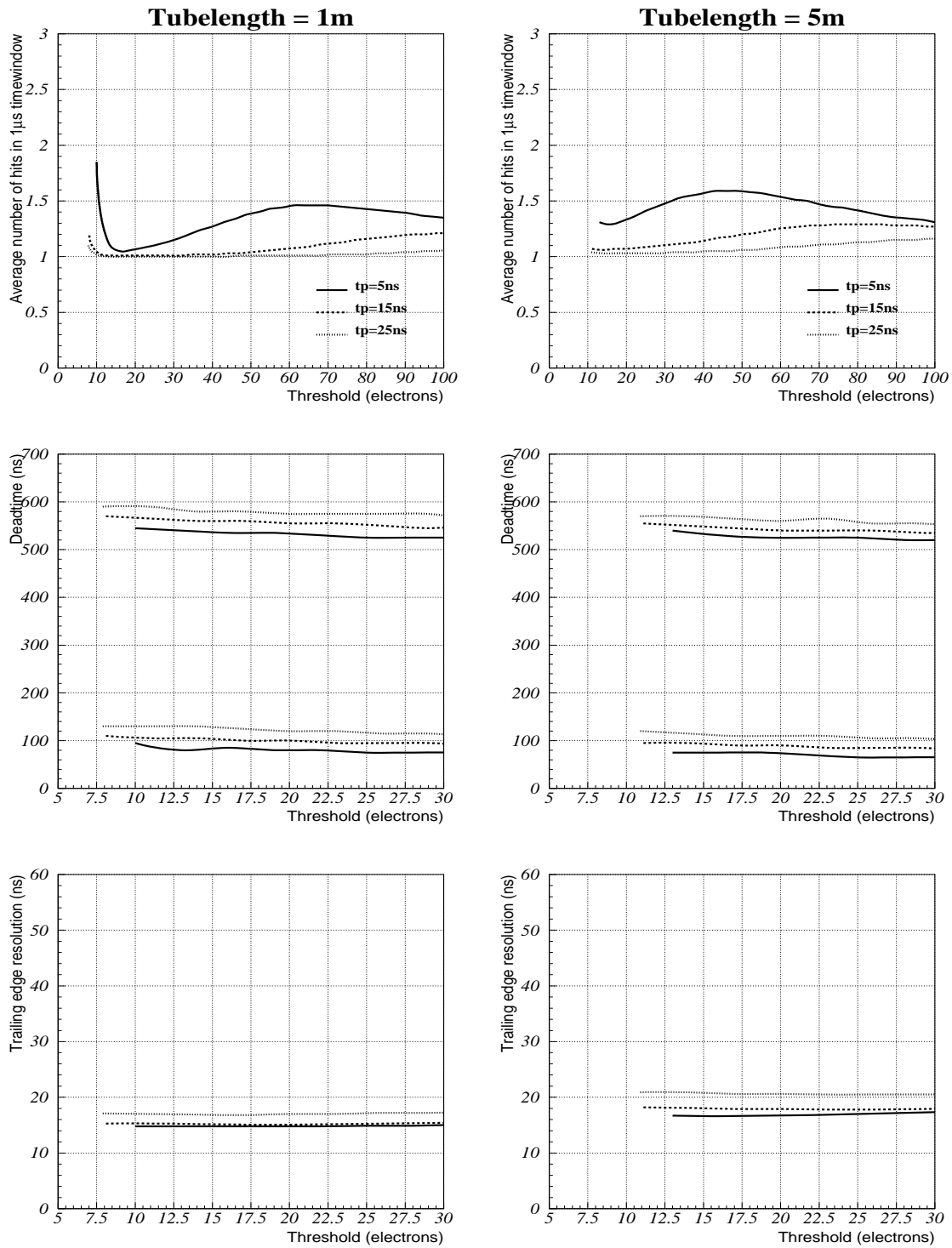
A discriminator hysteresis can help to reduce the amount of threshold crossings i.e. one applies a lower threshold for the trailing edge. The discriminator output is set high when the signal goes above threshold and it is set low when it goes below a lower threshold. The difference between the 'leading edge threshold' and the 'trailing edge threshold' is called hysteresis.

Fig. 6.13 shows the effect of a hysteresis value set to half the threshold. We see that the number of hits is reduced considerably.



**Figure 6.12 : Standard tail cancellation, hysteresis = 0.** The first row of figures shows the average number of hits for different peaking times and tube lengths. The muon impacts were randomly distributed over the whole tube length. The second row shows the minimum pulse width (lower curves) and the maximum pulse width (upper curves) for different peaking times. For a magnetic field of 0.5 T the maximum pulse width is about 100ns longer. The bottom figure shows the trailing edge resolution neglecting B-field and propagation time effects. A preamp with  $n=2$  was assumed.





**Figure 6.13 : Standard tail cancellation, hysteresis =  $0.5 \times$  threshold.** For explanation see fig. 6.12. The reduction of hits is considerable by introducing a hysteresis.

# Chapter 7

## Comparison of time slewing corrections with measurements

The simulation shows that we can improve the MDT resolution by performing a time slewing correction with the leading edge charge measured with a short gate ADC (gate  $< 2 \times tp$ ). The simulation was checked by using the data from the setup described in chapter 5. The leading edge charge was found by integrating the pulse (from the FADC) in a gate of 20ns after the threshold crossing time. The leading edge charge distribution is shown in fig. 7.1.

The slewing correction was done the following way:

The  $rt$ -relation and the resolution were found as described in chapter 5. The individual hit times  $t_i$  were corrected by

$$t_i^{corr} = t_i + c_1 \frac{ADC_i - \overline{ADC}}{\overline{ADC}}$$

where  $\overline{ADC}$  is the average of all ADC values and  $ADC_i$  is the leading edge charge corresponding to the threshold crossing time  $t_i$ . The parameter  $c_1$  is varied in order to minimize the residuals. Since the mean value of the charge changes with the distance from the wire the value of  $c_1$  also depends on the wire distance  $d$ . A straight line fit gives the distance dependence of the correction factor  $c_1(d)$  (fig. 7.2) and the drift times are corrected

$$t_i^{corr} = t_i + c_1(d) \frac{ADC_i - \overline{ADC}}{\overline{ADC}}$$

With the corrected hit times one repeats steps 1-5 described in chapter 5 and finds the corrected resolution.

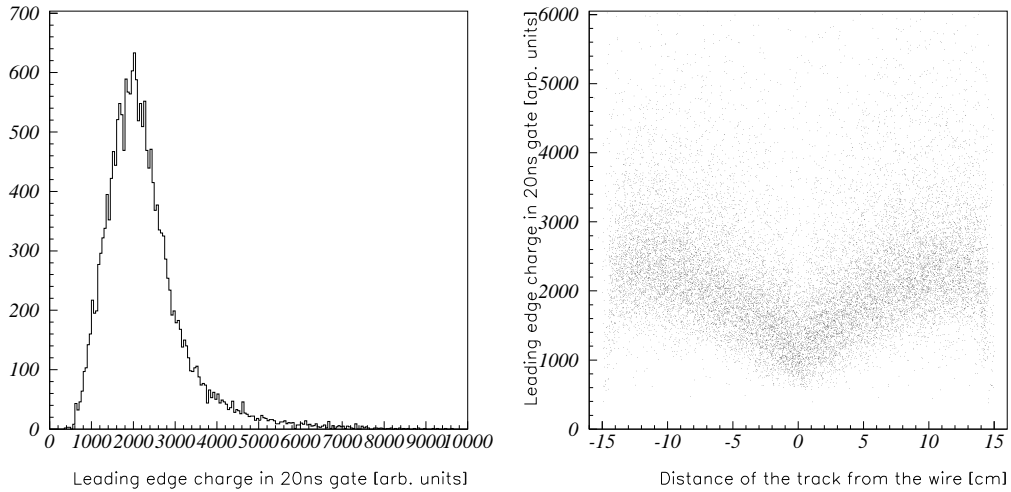


**Figure 7.1** : Leading edge charge in a 20ns gate. The increase of the average charge for long drift distances is due to a focusing effect shown in fig.12.4.

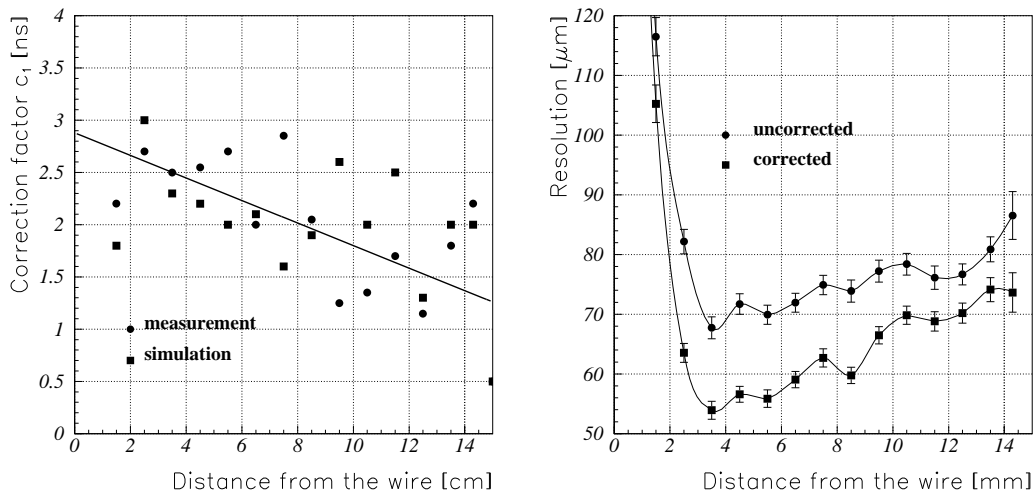


**Figure 7.2** : Distance dependence of the correction factor  $c_1$ . The right figure shows the improvement in resolution for a threshold of 18 electrons.

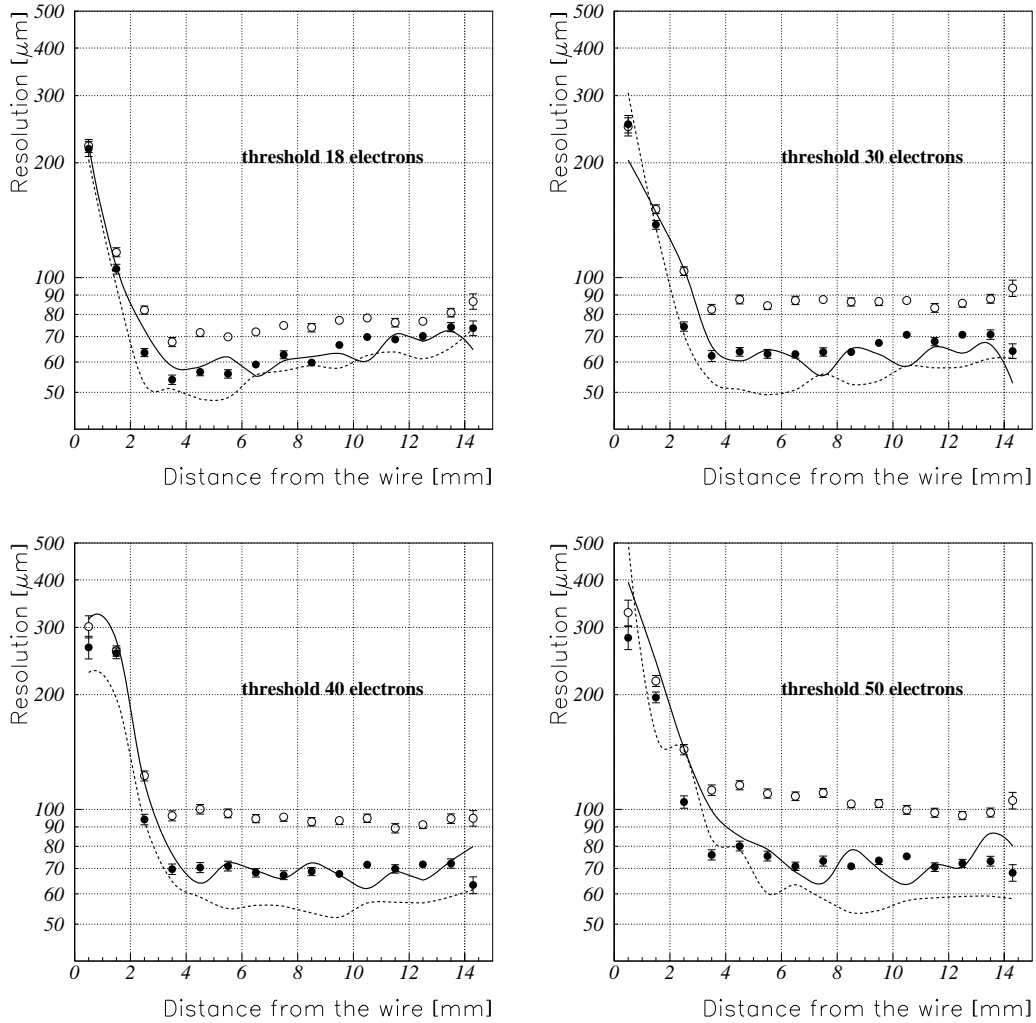


**Figure 7.3** : The radial dependence of the leading edge charge corrected resolution compared to simulation. The solid line is a simulation result using HEED to generate the ionization along the track. The dotted line shows a simulation using a cluster size distribution calculated by Lapique and Piuz [10]. The white points correspond to the uncorrected resolution. The resolution is plotted on a log scale to also show the decreased resolution close to the wire. The threshold dependence of the resolution can be reduced significantly.

Fig. 7.3 shows the corrected resolution for different thresholds compared to simulation. We see that the simulation using the cluster size distribution calculated with HEED fits the results best.

The resolution close to the wire can only marginally be improved by a time slewing correction. The reason for the reduced resolution at the wire is the high threshold in terms of electrons (18 electrons). Since we find on average 105 clusters per cm with 3 electrons per cluster when operating the chamber at three bars, there are on average 30 electrons/mm along the muon track, so 18 electrons are spread over a distance of  $600\mu m$ . Hence the arrival time of the 18th electron is the same for a track through the center of the wire and a track with a distance of  $600\mu m$  from the wire and also the slewing correction does not have any effect. The resolution close to the wire can only be improved by decreasing the threshold as shown in fig. 5.7.

# Chapter 8

## Space charge effects

The high counting rates in the muon system (up to  $500\text{Hz}/\text{cm}^2$  including a safety factor of 5) together with the long ion collecting time (ca. 4ms) can result in significant amounts of space charge in the MDTs which leads to gas gain reduction and systematic shifts of the rt-relation. If the counting rate would be constant this would be less severe but stochastic count rate fluctuations, fluctuations of the charge deposit as well as fluctuations due to changing accelerator luminosities translate the systematic shift of the rt-relation into an additive error that has to be added to the resolution at zero flux. Two effects lead to a change of the rt-relation:

- The change of the electric field causing a change of the electron drift time.
- The reduction of the gas gain causing a systematic shift of the threshold crossing time (systematic time slewing).

The first effect only depends on the space charge, the second one also depends on the preamplifier peaking time. The analysis of these issues is presented in the following chapter. We will use an average energy deposit of 32keV for the background events (see chapter 12.4). Assuming an effective ionization potential of 26eV for our counting gas (the main component is Ar) we obtain 1230 electrons per background event on average.

### 8.1 Theory of space charge effects

The ions created in the avalanche are moving towards the cathode with a velocity proportional to the electric field. If the irradiated part of the tube is longer than the tube diameter (which is the case) we can approximate the problem to be 2-dimensional. There are certainly limitations to this model since assuming a count rate of  $500\text{Hz}/\text{cm}^2$ , corresponding to  $1500\text{Hz}$  per  $\text{cm}$  of wire, together with a maximum ion drift time of  $4\text{ms}$  there

are on average only the ions of 6 events drifting in a 1cm slice of a tube, so a 2 dimensional approximation might not be sufficient. The following analysis shows however the relative sensitivity of different gases to space charge.

### 8.1.1 A first order model

The density of space charge in the MDT and the radial field dependence can be calculated the following way ( $\mu$  is the ion mobility):

$$\frac{dr}{dt} = \mu E(r) \quad \rightarrow \quad dt = \frac{dr}{\mu E(r)} \quad (8.1)$$

where  $dt$  is the time it takes an ion to get from  $r$  to  $r + dr$ . Dividing this by the area between  $r$  and  $r + dr$  and multiplying by the rate and the charge yields the charge density

$$\rho(r) = \frac{N_c G Q}{2r\pi\mu E(r)} \quad \begin{array}{l} N_c \dots \text{count rate per unit of length along the tube} \\ Q \dots \text{average charge deposited per background event} \\ G \dots \text{gas gain} \\ \mu \dots \text{ion mobility} \end{array} \quad (8.2)$$

For the given radial field dependence we get

$$E(r) = \frac{V_0}{r \log \frac{b}{a}} \quad \rightarrow \quad \rho = \frac{N_c G Q \log \frac{b}{a}}{2\pi\mu V_0} \quad (8.3)$$

To first order we find a uniform space charge in the tube. Using Gauss' theorem we can write down the following expression:

$$2r\pi E(r) = \frac{1}{\epsilon_0} \gamma + \frac{1}{\epsilon_0} \int_a^r 2r\pi \rho dr \quad (8.4)$$

where  $\gamma$  is the charge on the anode wire per unit of length and  $a$  is the anode wire radius. Since the HV supply adjusts a certain potential difference  $V_0$  between anode and cathode we find the parameter  $\gamma$  by the condition

$$\int_a^b E(r) = V_0 \quad (8.5)$$

where  $b$  is the cathode radius. Substituting  $\gamma$  into (8.4) gives:

$$E(r) = \frac{1}{r \log \frac{b}{a}} \left( V_0 - \frac{b^2 \rho}{4\epsilon_0} \right) + \frac{\rho}{2\epsilon_0} r \quad (8.6)$$

From this form we see that the space charge reduces the field on the wire and the loss in gas gain is in first order given by a voltage reduction of

$$\delta V = \frac{b^2 \rho}{4\epsilon_0} \quad (8.7)$$

The additional loss in gain from the fact that we have a voltage drop at the HV supply loading resistor ( $R_L = 1M\Omega$ ) is small since

$$\delta V_{RL} = R_L i = 10^6 N_{tube} Q G = 2V \quad (8.8)$$

$N_{tube} = 250kHz$  count rate per tube  
 $Q = 1230elec.$  average charge per event  
 $G = 2 \times 10^4$  gas gain  
 $\delta V_{RL}$  Voltage drop at the loading resistor.

### 8.1.2 Exact calculation

Since the space charge will change the radial field dependence it will also affect the dependence of  $\rho(r)$ . Here we study under which conditions the first order approximation can be used.

We start from equation (8.4) but now use the radial dependence of the charge density  $\rho(r)$  from (8.2).

$$2r\pi E(r) = \frac{1}{\epsilon_0} \gamma + \frac{1}{\epsilon_0} \int_a^r 2r\pi \rho(r) dr \quad (8.9)$$

where  $\gamma$  is again the charge on the anode wire per unit of length. Differentiation on both sides gives the equation

$$E(r)^2 + rE \frac{dE}{dr} = c_1 \quad c_1 = \frac{N_c G Q}{2\pi \mu \epsilon_0} \quad (8.10)$$

with the solution

$$E(r) = \sqrt{c_1} \frac{k}{r} \sqrt{1 + \frac{r^2}{k^2}} \quad k \dots \text{parameter} \quad (8.11)$$



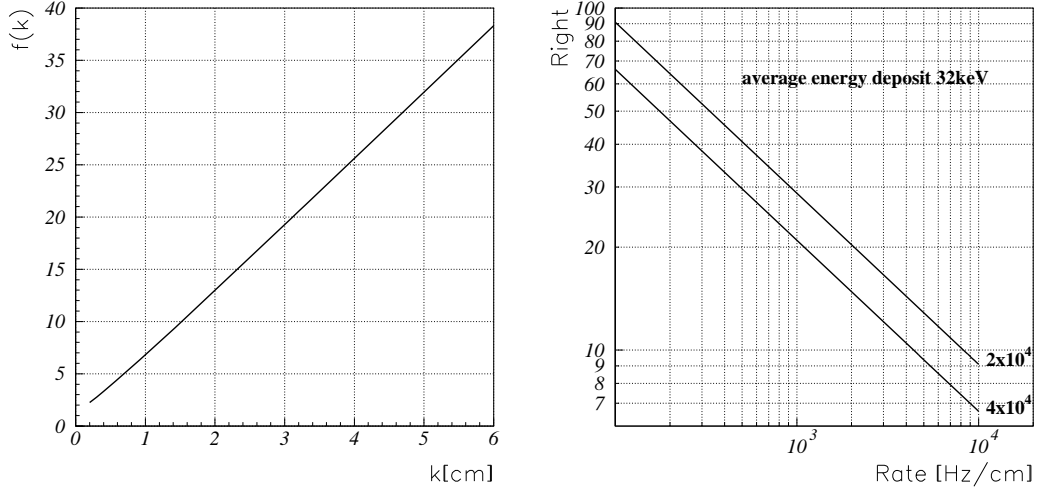


**Figure 8.1** : Left and right side of expression (8.12) for different rates and gas gains.

The parameter  $k$  is obtained from the constraint (8.5). This parameter is a characteristic length that will allow us to estimate the size of the space charge effect since it tells us how we can expand (8.11). By resubstituting  $E(r)$  into (8.4) we can find the connection between  $\gamma$  and  $k$ . The condition (8.5) results in the transcendental equation

$$k \log \frac{b(k^2 + k\sqrt{k^2 + a^2})}{a(k^2 + k\sqrt{k^2 + b^2})} + \sqrt{k^2 + b^2} - \sqrt{k^2 + a^2} = V_0 \sqrt{\frac{2\pi\mu\epsilon_0}{N_c G Q}} \quad (8.12)$$

The left side depends only on  $a, b$  and  $k$  and since  $a$  and  $b$  are fixed:

$$f(k) = V_0 \sqrt{\frac{2\pi\mu\epsilon_0}{N_c G Q}} \rightarrow k \rightarrow E(r) \quad (8.13)$$

This equation can easily be solved numerically. The reduced field will of course reduce the gas gain, so this effect we have to calculate from iterating (8.11) and (8.13). From plotting (8.13) we can find the order of  $k$  for our case (fig. 8.1).

If  $r \ll k$ , so if  $k \gg 1.5\text{cm}$  we can expand (8.13) and (8.11) and the two expressions reduce to

$$E(r) \approx \sqrt{c_1} \frac{k}{r} + \sqrt{c_1} \frac{r}{k} \quad \text{and} \quad k \log \frac{b}{a} - \frac{b^2}{4k} = \frac{V_0}{\sqrt{c_1}} \quad (8.14)$$

Solving for  $k$  gives the field

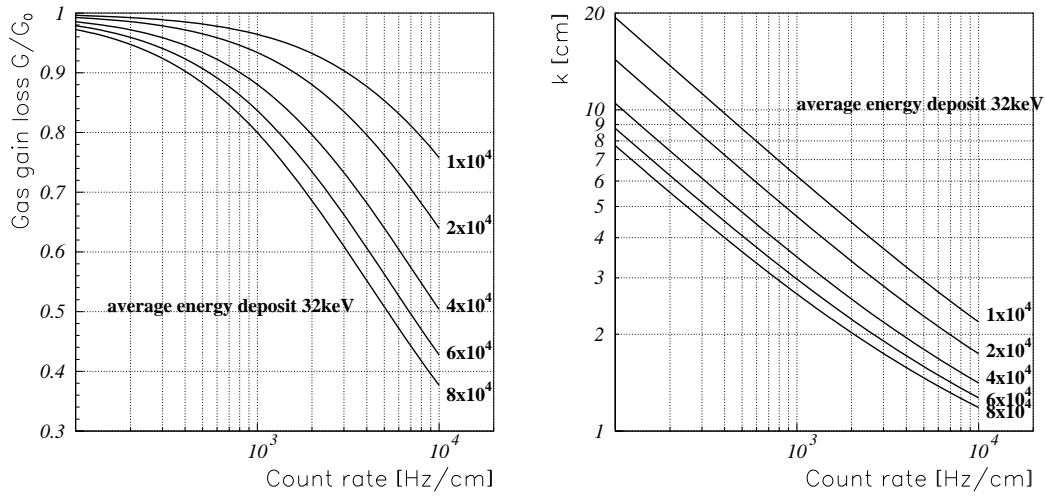


**Figure 8.2** : Gas gain loss and the parameter  $k$  as a function of the count rate per  $cm$  of wire.

$$E(r) = \frac{V_0}{r \log \frac{b}{a}} \left( 1 - \frac{b^2 N_c G Q \log \frac{b}{a}}{8\pi\epsilon_0\mu V_0^2} \right) + \frac{N_c G Q \log \frac{b}{a}}{4\pi\epsilon_0\mu V_0} r \quad (8.15)$$

which is the field configuration that we found in the first order calculation (8.6).

## 8.2 Gas gain reduction due to space charge

For all the following calculations the exact expression for the field (8.11) was used. The gain loss was found by iterating the formulas. Fig. 8.2 shows the dependence of the parameter  $k$  and the gas gain on the counting rate for different gas gains. Assuming a rate of  $500 Hz/cm^2$  which already includes a safety factor of five we have a count rate of  $1.5k Hz$  per  $cm$  of wire. For a gas gain of  $2 \times 10^4$  we find a gas gain loss of about 10%.

## 8.3 Shift of the $rt$ -relation

Using this formulation we are able to calculate the shift of the  $rt$ -relation due to the change of the electric field and the gas gain reduction. The following chapter will treat these effects.

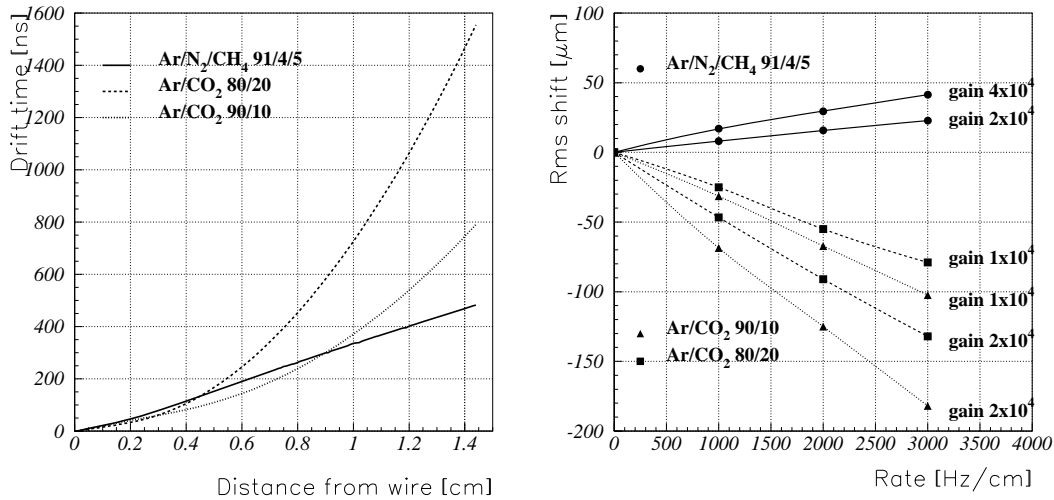


**Figure 8.3** : The left figure shows the  $rt$ -relations of the gases that were studied. The right figure shows the rms bias due to the change of the radial field dependence for different count rates, so applying the  $rt$ -relation for zero count rate to data taken at a given count rate will cause a bias in resolution as given by this plot. Note that for the  $Ar/N_2/CH_4$  mixture the space charge 'slows the gas down' while for the  $Ar/CO_2$  mixtures the gas speeds up i.e. the maximum drifttime becomes smaller. The effect of gain reduction is not introduced (see fig. 8.5).

### 8.3.1 Shift of the $rt$ -relation due to drift time changes

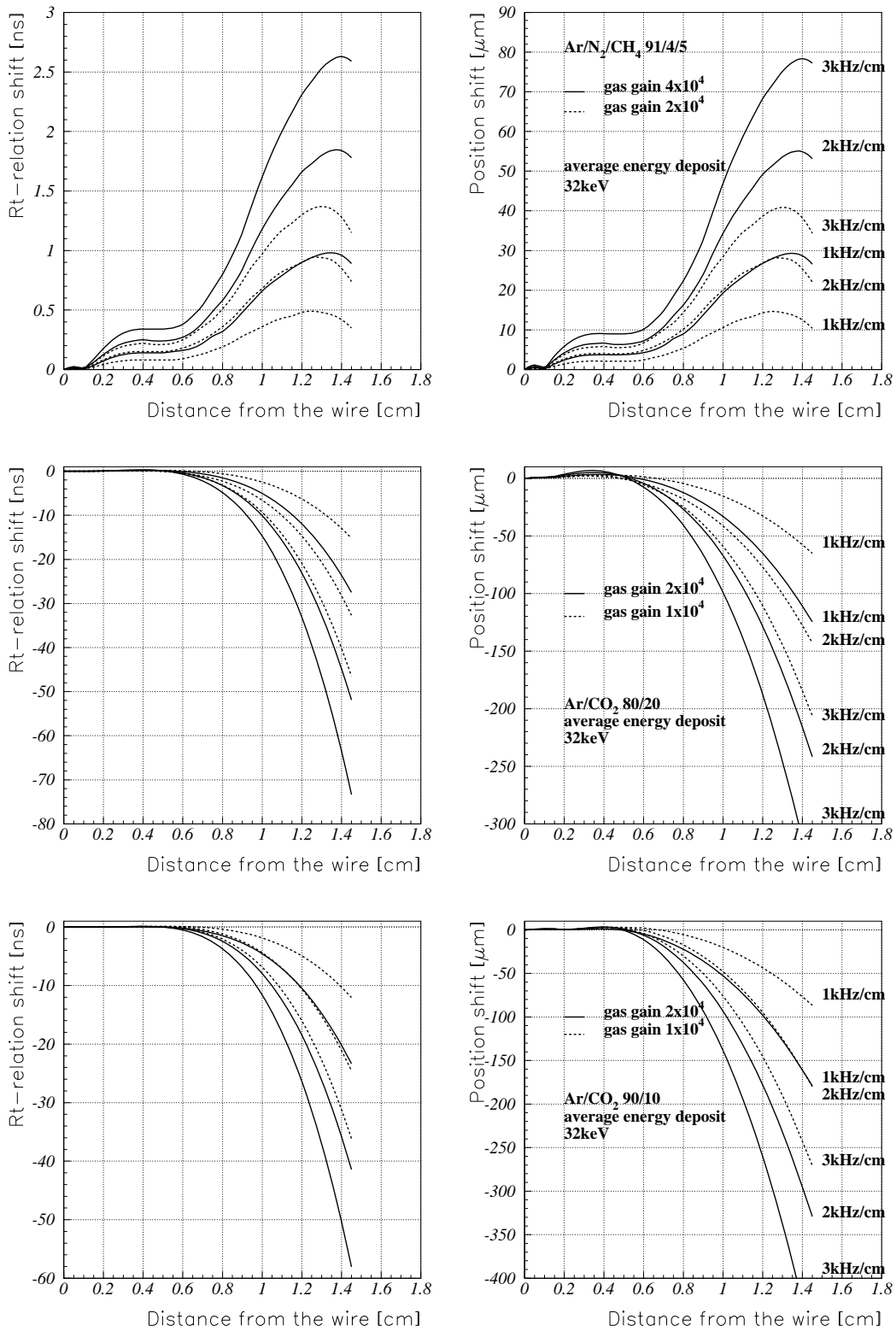
The changes of the  $rt$ -relation for different rates are shown in fig. 8.4. To get a feeling for the worst case loss in resolution the figure also shows the bias in resolution that we get from applying a  $rt$ -relation for zero rate to data taken at a certain rate. The rms value of this shift is shown in fig. 8.3.

### 8.3.2 Shift of the $rt$ -relation due to gas gain reduction

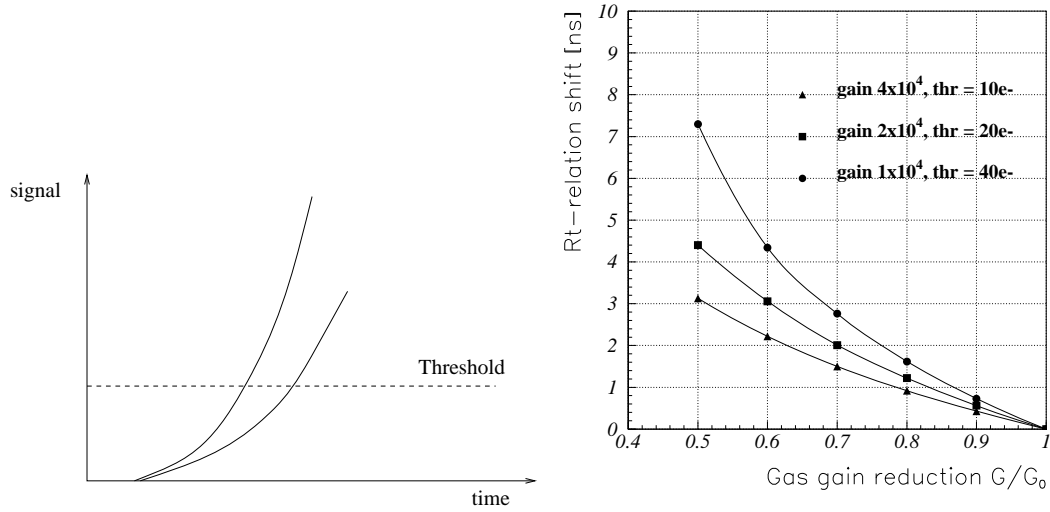
In addition to the error due to change of the electron drift time a further error due to reduced gas gain has to be considered (fig. 8.5). We see that the change of the  $rt$ -relation due to this effect is approximately  $1ns$ . The change of the  $rt$ -relation due to gain loss for  $Ar/N_2/CH_4$  will be an additional effect since  $1ns$  is comparable to the shift discussed above. For  $Ar/CO_2$  we expect only a very small effect since the  $rt$ -relation shift from space charge is already of the order of  $20ns$ .

Fig. 8.6 shows the  $rt$ -relation shift due to space charge and gain loss for  $Ar/N_2/CH_4$ . Fig. 8.7 shows the average bias in resolution from both effects.

As expected the effect is big for the  $Ar/N_2/CH_4$  mixture while for the  $Ar/CO_2$  mixtures we even see a small improvement compared to fig 8.3. This is due to the counteraction of



**Figure 8.4 :** The left row of figures shows the change of the  $rt$ -relation for different counting rates, the right row of figures shows the associated bias in resolution.



**Figure 8.5 :** Due to the finite rise time of the signal there is a systematic shift of the threshold crossing time if the pulse height is reduced.

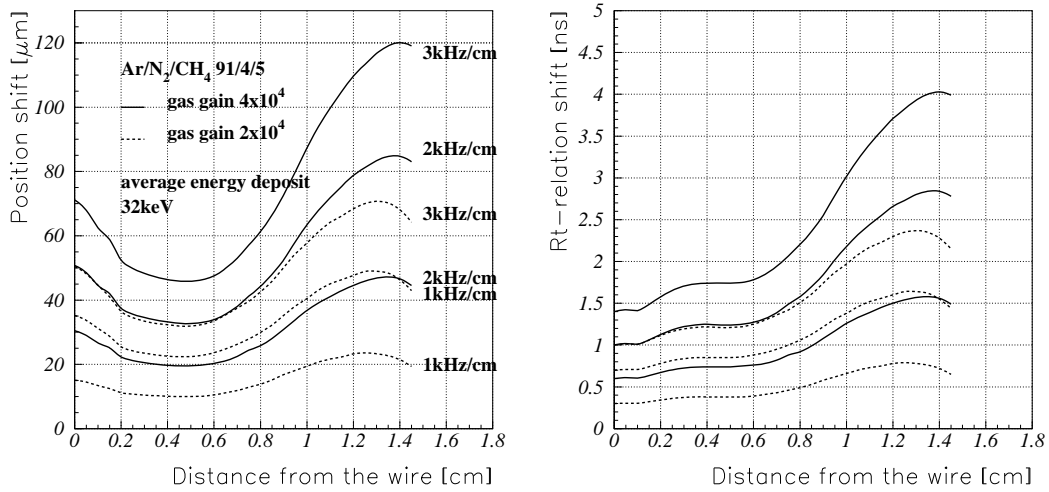


**Figure 8.6 :** Shift of the  $rt$ -relation and associated bias in resolution due to field changes and gas gain loss.

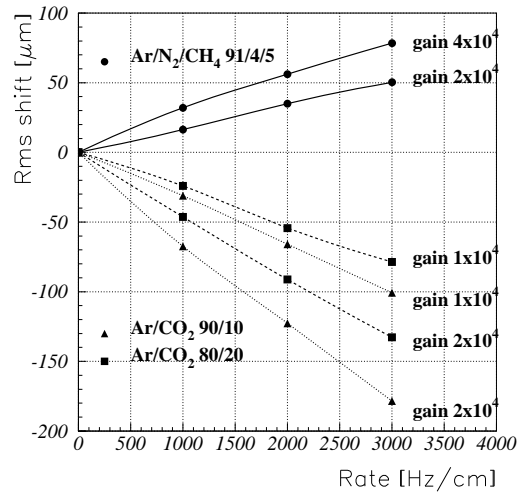


**Figure 8.7** : Rms bias of the resolution including the change of  $rt$ -relation and gas gain loss.

two effects: the space charge 'speeds up' the  $Ar/CO_2$  mixture; the gain reduction shifts the  $rt$  relation to larger times.

From this analysis we conclude that space charge effects impose a severe requirement on the linearity of the gas. The  $Ar/N_2/CH_4$  mixture meets the requirement that the average resolution of  $80\mu m$  is not affected by space charge effects. At a count rate of  $1.5kHz/cm$  the  $Ar/CO_2$  mixtures do not meet these requirements for a gas gain of  $2 \times 10^4$ .

# Chapter 9

## Temperature effects

Similar to space charge the temperature affects the resolution in two ways:

- The shift of the  $rt$ -relation due to drift velocity changes because of
  1. the change of the gas density
  2. the change of the energy distribution of the gas atoms.
- The change of the gas gain and the associated systematic shift of the threshold crossing time due to the finite signal rise time.

The MDT gas system will control the density of the gas, so in principle there should be no change in  $rt$ -relation since the drift velocity and gas gain are a function of  $E/P$ . The change in drift velocity with temperature due to the change in the energy distribution of the gas atoms is very small. A MAGBOLTZ calculation shows a bias in resolution of  $< 1\mu m$  for a temperature difference of  $50K$ , so we can assume that the  $rt$ -relation is affected by temperature only through a change in gas density.

Since we expect temperature variations of up to  $2K$  across a chamber we have to consider a change in density even if the total chamber is density controlled.

### 9.1 Shift of the $rt$ -relation due to drift time changes

Fig. 9.1 shows the  $rt$ -relation shift and the associated bias in resolution due to a change in temperature assuming constant pressure. As for the space charge effects we find that a linear gas is much less sensitive than a nonlinear gas.

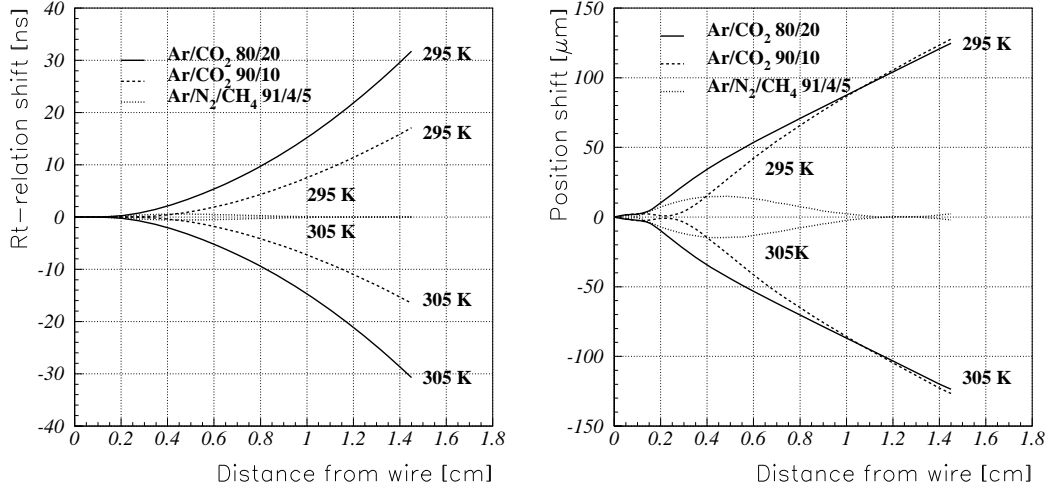


**Figure 9.1** : Shift of the  $rt$ -relation and associated position shift for a change in temperature with respect to 300K at constant gas pressure.

## 9.2 Shift of the $rt$ -relation due to gas gain changes

According to Diethorn's formula [33] the gas gain dependence on voltage  $V$ , wire radius  $a$ , tube radius  $b$  and gas density  $\rho$  is given by

$$\log G = \frac{\log 2}{\log \frac{b}{a}} \frac{V}{\Delta V} \log \frac{V}{\log \frac{b}{a} E_{min}(\rho) \frac{\rho}{\rho_0}} \quad (9.1)$$

where  $\Delta V$  and  $E_{min}$  are characteristic constants for the specific gas mixture. Assuming that we have a system where the pressure is controlled to be constant, the gas density is inversely proportional to the temperature, so using the above formula, the temperature dependence of the gain is given by

$$\log \frac{G}{G_0} = \frac{\log 2}{\log \frac{b}{a}} \frac{V}{\Delta V} \log \frac{T}{T_0} \quad (9.2)$$

Fig. 9.2 shows this dependence for some gas mixtures. As the temperature increases the mean free path of the electrons in the avalanche increases, they gain more energy in between collisions and therefore the gain increases. Taking into account the time slewing from the change in gain and the change of the drift velocity with temperature we find the total rms resolution bias as shown in fig. 9.2.



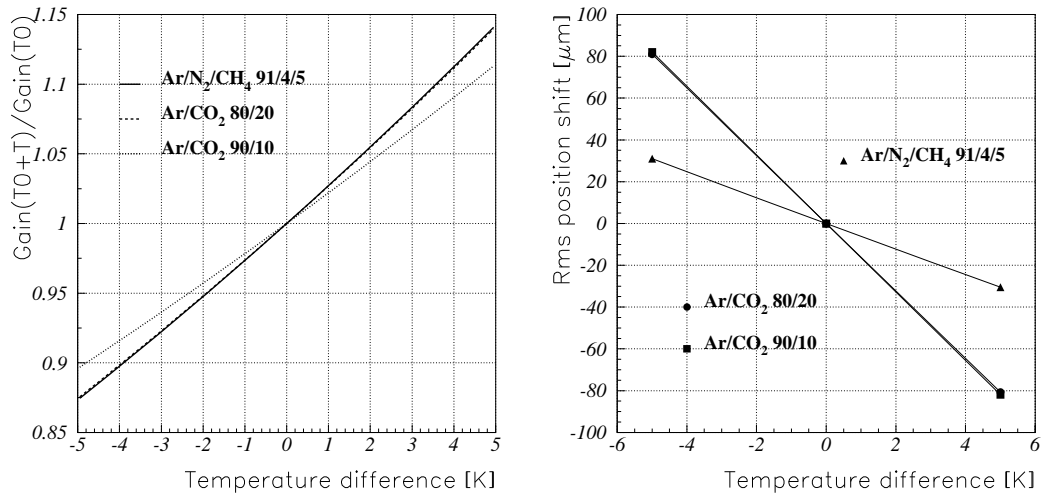


**Figure 9.2** : The left figure shows the change of gas gain with temperature. The right figure shows the rms resolution bias taking into account the gas gain and the drift velocity change due to temperature changes.

# Chapter 10

## Baseline shift

In addition to space charge effects, the high count rates can deteriorate the resolution through another effect namely baseline shift. Since all the charge deposited on the wire by the incident particles is fed back to the wire from the power supply through the loading resistor, the current seen by the preamplifier must integrate to zero over long time scales. E.g. a regular sequence of rectangular pulses causing an occupancy of 20% would shift the baseline by 20% of the pulse height (fig. 10.1).

Since there will be occupancies up to 10% in the MDT system corresponding to a counting rate of 400kHz (including a safety factor of 5) we definitely have to consider this problem. The fluctuation in the time separation of the incident particles together with the charge deposit fluctuations will not only cause a systematic shift but also a time dependent fluctuation of the baseline.

The degree of baseline shift depends crucially on the tail cancellation applied to the signal. Fig. 10.2 shows the response of the MDT to a single ionization electron. The induced current signal is of the form

$$i(t) = c_1 \frac{1}{t + t_0} \quad t = 0 \dots T_{max} \quad \text{with} \quad t_0 = 11ns \quad \text{and} \quad T_{max} = 4ms$$

We see that the long undershoot of the signal resulting from the the AC coupling of the

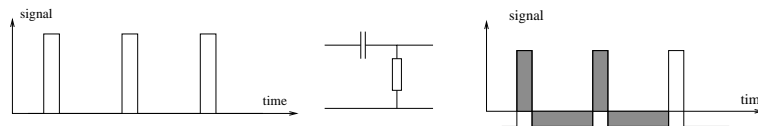


**Figure 10.1** : In an AC coupled system the total signal integrates to zero which results in baseline shift. The figure shows the result of sending a sequence of square pulses through a high pass CR filter.

system is smaller if we cancel the signal tail. The figure also indicates that the signal still affects the baseline after a time of 10ms!

A Monte Carlo simulation was performed to evaluate the amount of baseline shift and baseline fluctuation. Most of the background in the MDT system is due to photons with an average energy deposit of 32keV corresponding to about 1300 primary electrons in 3 bars of argon (see chapter 12.4). Pulses with a pulse height distribution following the expected charge distribution with a mean value of 1300 electrons were distributed randomly in time over a period of 15ms. The time separation of the signals is exponentially distributed with a mean value of  $2.5\mu s$  corresponding to a count rate of 400kHz. The pulses were sent through MDT, preamp and filters. The value of the baseline at the end of the 15msec period was histogrammed. The procedure was repeated 1000 times. Fig. 10.3 shows the baseline fluctuations for the different filtering schemes in units of primary electrons. We see that for our signal processing system using two pole/zero filters we get an average baseline shift of 30 electrons with a big variation around this value.

Since we intend to use a threshold of 20 primary electrons such shifts are therefore not acceptable. Two possible solutions are the following:

- Using bipolar signal shaping or 'overcompensation' as shown in fig. 10.2 reduces the baseline shift and the baseline fluctuation to an acceptable level as one can see in fig. 10.3. The drawback of this scheme is that multiple threshold crossings for signals from single tracks are unavoidable (two crossings on average for a threshold of 20 electrons). Typical signal shapes using overcompensating filters are shown in fig. 12.17. In addition we would lose the trailing edge information and the possibility of double track separation if we want to encode the multi-hit information into one output channel (see chapter 12.4.2).
- Using active baseline restoration by means of a nonlinear feedback circuit one can restore the baseline without affecting the pulse shape (to first order) even in the case of unipolar pulse shaping [18]. The baseline restorer integrates the output signal and is connected to the preamp input by a nonlinear feed back loop to correct for the baseline offset. If the integration time is chosen to be short, the baseline will be restored quickly but the signal shape will be affected. Depending on the count rate, the integration time has to be chosen small enough to keep the baseline fluctuations within the desired limits ( $< 3$  electrons) but large enough in order not to affect the pulse shape. Whether this is possible for rates up to  $400kHz$  is under investigation at the moment. This scheme would be recommended since we would keep all the information contained in the signal like trailing edge and multi-hit information and we would still expect only one threshold crossing per signal.

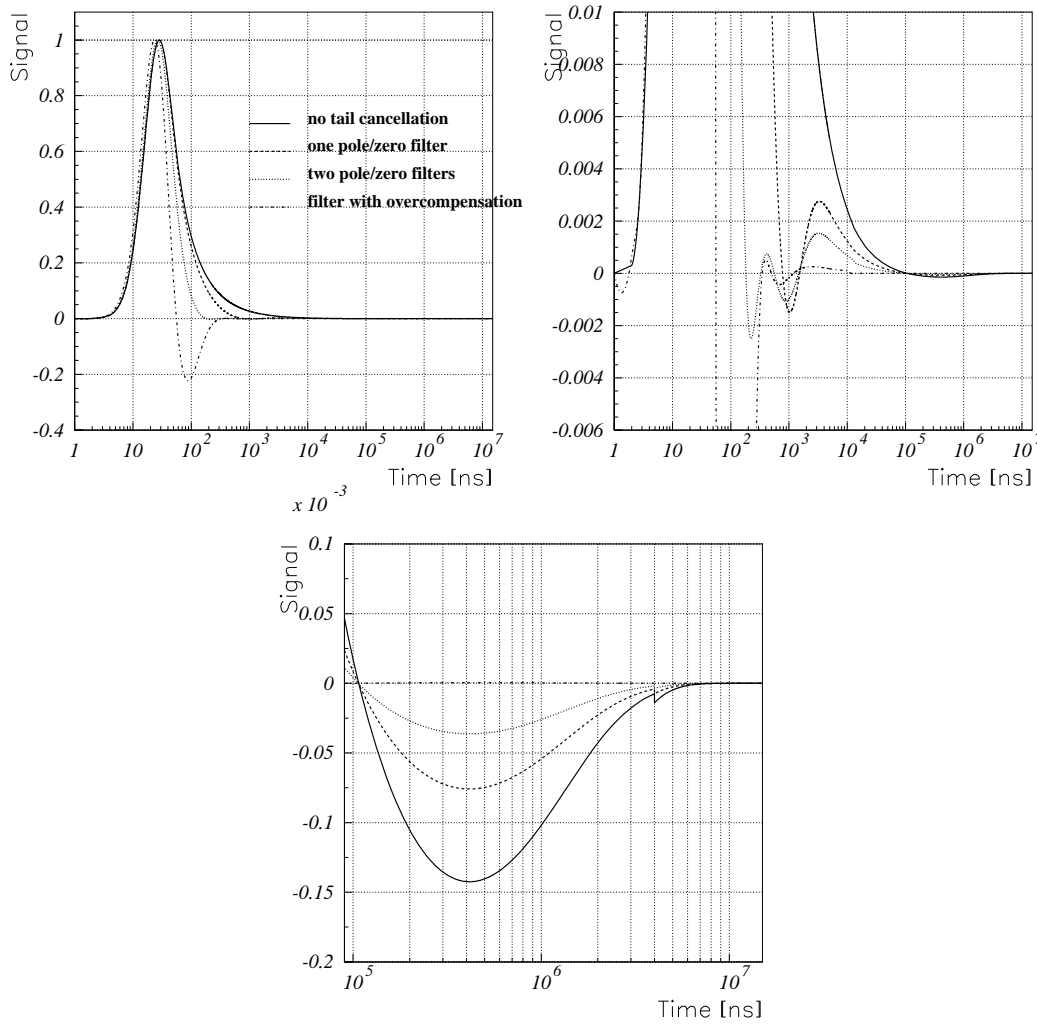


**Figure 10.2** : Response of the MDT to a single ionization electron. The first figure shows the output signal for different filters. Note that the time axis is a log scale from 0 to 15ms. The second figure is a zoom of the first one and displays the action of the filters. The third figure is again a zoom of the second one and shows the action of the loading resistor that brings the voltage of the wire back to the desired value. Since the area of the signal below the zero line must equal the area above the zero line, the undershoot is reduced by using tail cancellation. In the case of overcompensation the long undershoot is almost removed since a large part of the 'signal area' is already compensated very early. Using tail cancellation compensating the area above and below the zero line immediately after the signal is called bipolar shaping.

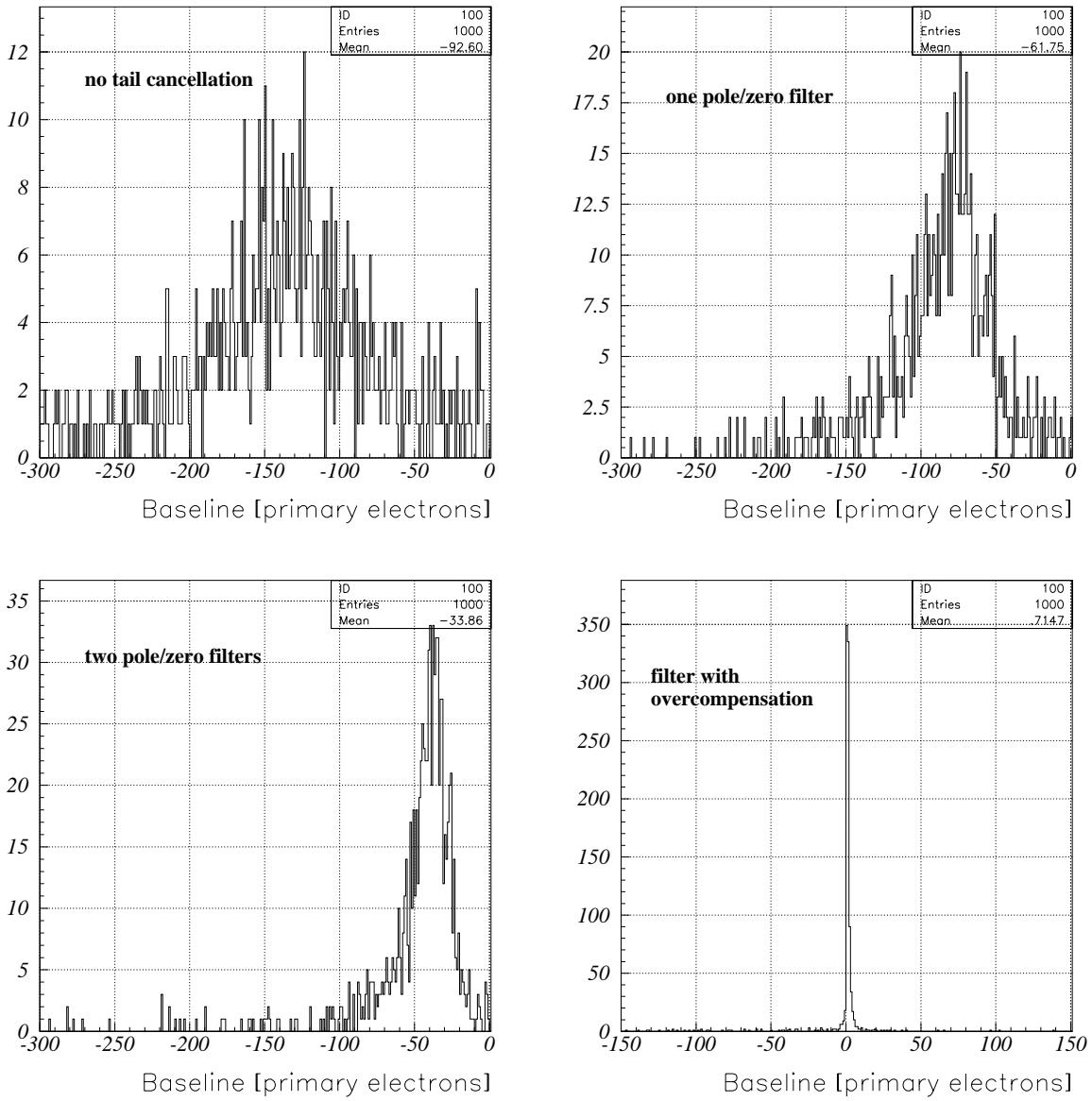


**Figure 10.3** : The histograms show the result of the Monte Carlo simulation. The four histograms correspond to the four tail cancellation schemes indicated in fig. 10.2. Since our goal is a baseline fluctuation of less than 3 electrons we have to use either bipolar shaping or an active baseline restoration circuit.

# Chapter 11

## MDT wire vibrations

Since we measure the distance of the muon track from the wire we must be sure that the wire is at the nominal position. As an example, vibrations of the wire with  $> 20\mu m$  rms around this position must be avoided. In case a wire vibrates, two measurement errors occur:

- the rt-relation is distorted since the wire moves out of the center of the tube (fig. 11.1). This effect is very small for gases with the desired linearity.
- since we measure the distance of the track from the wire and since the electron drift time is much shorter than the wire vibration periods, the measurement error is equal to the displacement of the wire at the time of the particle passage.

There are two possible sources for wire vibrations. Vibrations induced by the electrostatic repulsion of the wire from the ions created in the avalanche, an effect that was discovered only recently, and vibrations induced externally by movements of the chamber supports.

### 11.1 General frequency and damping characteristics of the MDT wires

The MDT wires can simply be modelled as a string. The differential equation describing a damped string is

$$\rho_0 \frac{\partial^2 y}{\partial t^2} + \gamma_0 \frac{\partial y}{\partial t} - T_0 \frac{\partial^2 y}{\partial x^2} - \kappa y = 0 \quad (11.1)$$

where

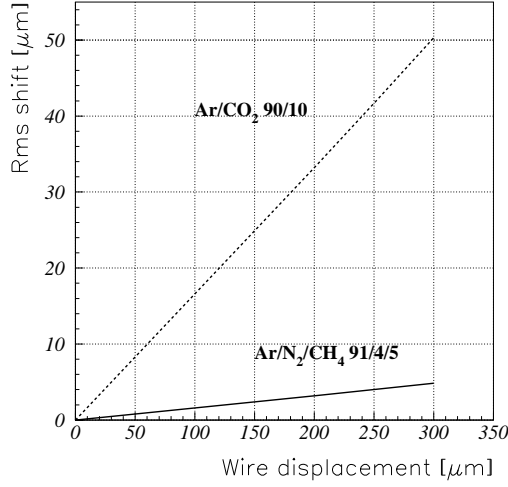


**Figure 11.1** : Rms shift of the position measurement due to a shift of the tube with respect to the wire. For a linear gas like  $\text{Ar}/\text{N}_2/\text{CH}_4$  the bias in resolution is  $< 5\mu\text{m}$  even if the wire is off center by  $300\mu\text{m}$ .

$\rho_0$	mass of the wire per unit of length	
$\gamma_0$	damping coefficient	
$\kappa = \frac{2\pi\epsilon_0 V^2}{(R \log R/r)^2}$	coefficient for the electrostatic force	(11.2)
$r, R$	wire and tube radius	
$V$	Voltage on the wire	

We can omit the term for the gravitational force since the tubes in the MDT chambers will be bent such that they follow the sag of the wire. The damping is assumed to be proportional to the velocity of the wire and independent of the frequency which is not a very good approximation in our case as will be shown below. The solution of the above equation for the boundary conditions  $y(0) = 0$  and  $y(L) = 0$  is

$$y(x, t) = \sum_{n=0}^{\infty} \sin(k_n x) e^{-\frac{\Gamma}{2}t} [A_n \cos(\omega_n t) + B_n \sin(\omega_n t)] \quad (11.3)$$

where

$$\begin{aligned} \Gamma &= \gamma_0 / \rho_0 \\ k_n &= n\pi / L \\ \omega_n &= \frac{n\pi}{L} \sqrt{\frac{T_0}{\rho_0} - \frac{\kappa L^2}{\pi^2 n^2 \rho_0} - \frac{\Gamma^2 L^2}{4n^2 \pi^2}} \end{aligned} \quad (11.4)$$

Using the design numbers

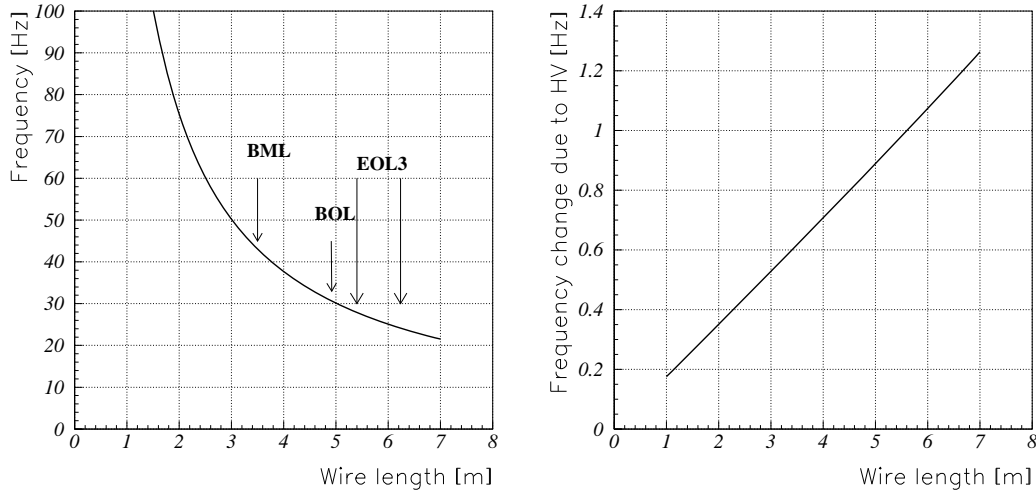


**Figure 11.2 :** Frequency of the lowest vibration mode for different wire lengths. The right figure shows the change in frequency for a voltage of 3500V.

$$R = 1.46\text{cm} \quad r = 25\mu\text{m} \quad T_0 = 350\text{g} \quad \rho_0 = 3.78 \times 10^{-5}\text{kg/m} \quad V = 3500\text{V} \quad \Gamma \approx 2.51\text{s}^{-1}$$

we find

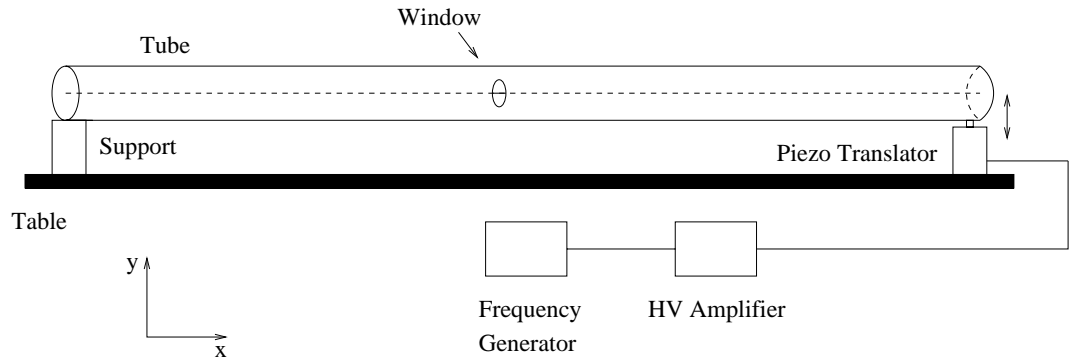
$$\omega_n = \frac{n\pi}{L} \sqrt{90793 - \frac{211L^2}{n^2} - \frac{0.16L^2}{n^2}} \quad . \quad (11.5)$$

Fig. 11.2 shows the frequencies of the first vibration mode versus wire length. If we would put a wire locator in the middle of the BOL tubes (4.99m) and the longest tubes in the endcap chambers (6.24m) we would double the lowest frequency.

To find out about the amplitude of the wire for a given excitation of the tube we have to measure the damping coefficient. The damping of the wire was determined experimentally with a setup shown in fig. 11.3. The wire was  $50\mu\text{m}$  W/Re 97/3. The tube diameter was 30mm with  $400\mu\text{m}$  walls. The wire length was 386mm with a tension of 348g.

The tube was supported at one end and fixed to the piezo vibrator at the other end. The piezo element expands  $40\mu\text{m}$  for a voltage change of 1000V, so by applying a harmonic voltage wave of 25V amplitude one can excite a  $1\mu\text{m}$  amplitude to a very high precision. The wire amplitude was measured in the middle of the tube with a microscope. The microscope had a  $10\mu\text{m}$  scale and a total field of view of 1mm. The frequency dependence of the wire amplitude for an excitation amplitude of  $1\mu\text{m}$  measured in the middle of the tube is shown in fig. 11.4. At the resonance frequency we find wire amplitudes of 40-50  $\mu\text{m}$  for the first and the third mode.





**Figure 11.3** : Setup for measuring the MDT wire damping.

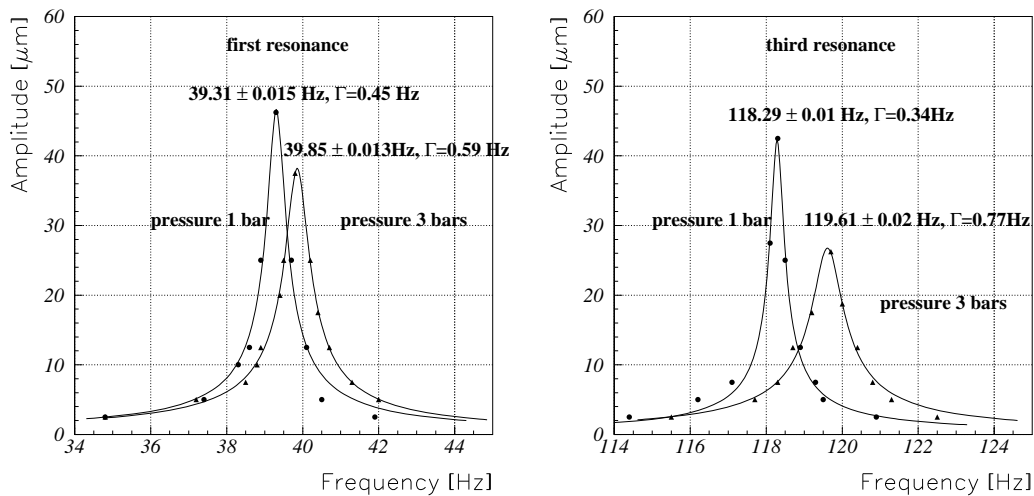


**Figure 11.4** : Wire resonant amplitudes for an excitation amplitude of  $1\mu\text{m}$ . The decrease in amplitude with pressure is due to friction of the wire with the gas, the change in frequency with pressure is due to an increased tension of the wire because of tube expansion and movement of the end plugs within the tube.

The main mechanism for the wire damping at low frequencies is structural damping i.e. internal damping of the wire. By increasing the gas pressure, because of the velocity dependence of the damping from friction with the gas, only the higher vibration modes show additional damping. The first mode is only moderately affected by the increase in pressure.

The damping factor  $\Gamma$  and the resonance frequency were obtained by fitting the function

$$f(\omega) = \frac{A_0}{\sqrt{(\omega_0^2 - \omega^2)^2 + \omega^2\Gamma^2}} \quad (11.6)$$

to the resonance curves. The wire amplitude was strictly linear with the excitation amplitude (checked up to an excitation amplitude of  $10\mu m$ ). The increase in the resonance frequency for a pressure of 3 bars is connected to an increased tension of the wire. Knowing the Young modulus  $Y$  of Al and W we can calculate the change in frequency due to the gas pressure.

$$Y_{Al} = 4 \times 10^5 N/mm^2 \quad Y_W = 7 \times 10^5 N/mm^2$$

The change in length of the tube and the wire  $\Delta L/L$  is given by

$$\frac{\Delta L}{L} Y_{Al} = \frac{\Delta F_P - F_W}{A_{tube}} \quad \frac{\Delta L}{L} Y_W = \frac{\Delta F_W}{A_{wire}}$$

where

$$\Delta F_P = R^2 \pi P \quad A_{tube} = 2R\pi d \quad A_{wire} = r^2 \pi$$

$d$  is the wall thickness of  $400\mu m$ .  $\Delta F_W$  is the additional force on the wire and  $\Delta F_P$  is the force on the end plug which for  $P = 2$ bars (3bars absolute) is  $14kg$ . Solving for  $\Delta F_W$  gives

$$\Delta F_W \approx \Delta F_P \frac{Y_W A_{wire}}{Y_{Al} A_{tube}}$$

Finally we find a change in tension of  $4.12g$  which is  $1.18\%$  for a tension of  $350g$ . The change in frequency is  $0.25Hz$  for the first mode and  $0.69Hz$  for the third mode, so this accounts only for half of the shift observed in fig. 11.4 where we find a frequency shift of  $0.54Hz$  and  $1.32Hz$ . The change in length of the 4m tube is  $200\mu m$ .

Measuring the expansion of the tube gave a value of  $170\mu m$  for a pressure change from 1 to 3 bars. Measuring the increase in distance between the two end plugs that hold the wire

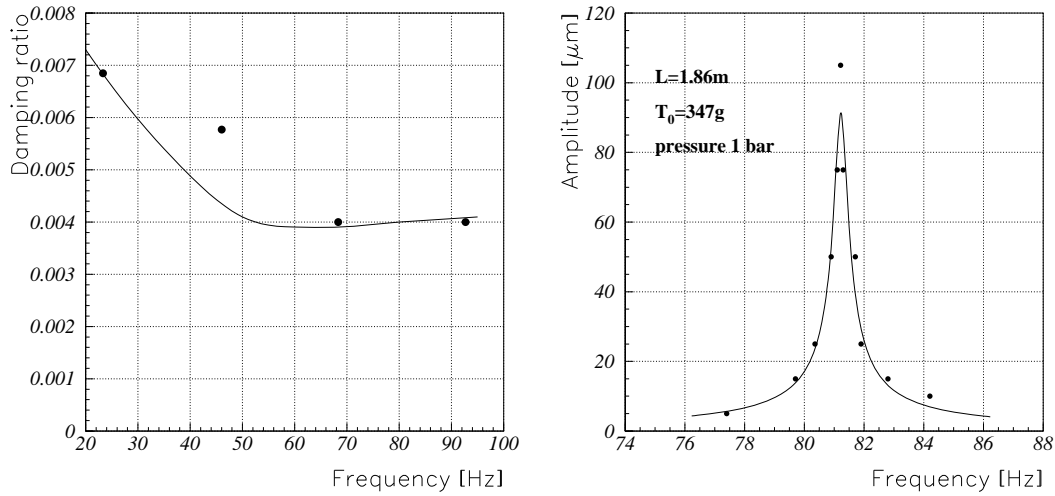


**Figure 11.5 :** The left figure shows the frequency dependence of the damping ratios, the points are measurements and the curve indicates a calculation [34]. the right figure shows the resonant amplitude for a wire length of 1.86m for an excitation amplitude of  $1\mu m$ .

gave a value of  $430\mu m$  which explains the observed frequency change. So in addition to the tube expansion the end plugs moved with respect to the tube which should definitely be avoided in the final tube design.

Since the chamber multilayers are fixed rigidly to the spacer frame only in the middle of the tubes and the connection to the spacer at the tube ends is flexible we have to take the change in tension with pressure into account in the final design.

If the damping would be independent of the frequency, the amplitude of the wire at the resonance frequency for a given excitation amplitude would be independent of the length.

Since the damping of the wire changes with frequency, the amplitude of the wire at the resonance frequency depends on the length of the wire. The shorter the wire, the higher is the amplitude at the resonance frequency for a given excitation amplitude since the damping ratio of the wire is smaller for high frequencies as shown in fig. 11.5. The damping ratio is defined as  $\Gamma/\Gamma_c$ , where  $\Gamma$  is the actual damping coefficient at the given frequency and  $\Gamma_c$  is the critical damping coefficient at that frequency. The behaviour of a wire within a chamber will be discussed later.

## 11.2 Vibrations induced by radiation

The effect was discovered by a group from Dubna and is described in [35]. The ions created in the avalanche process move only slowly towards the tube walls and apply a repulsive force on the positively charged wire. The effect can be calculated by putting randomly

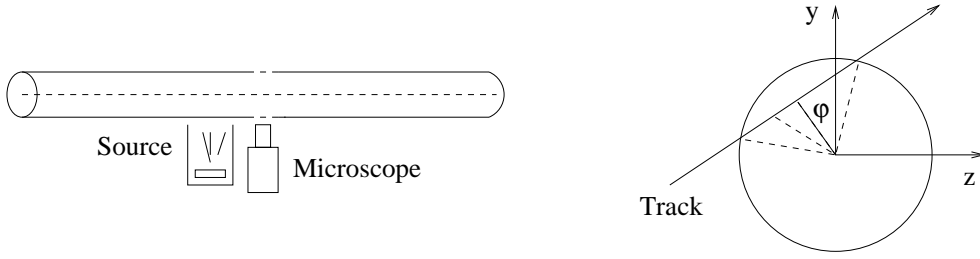


**Figure 11.6** : Setup for the measurement of avalanche induced wire vibrations.

distributed forces to equation (11.1).

A charge  $Q_i$  at a distance  $d$  from a wire at voltage  $V$  causes a force of

$$f_i = \frac{q_i V}{d \log R/r} \quad (11.7)$$

Since the time it takes the ions to move from the wire to the tube wall is smaller than the period of the wire vibration modes (the ion collecting time is around  $4ms$  and the period of the lowest modes is around  $10 - 20ms$ ) the integrated force on the wire can be approximated to be instantaneous.

$$F_i = P_i \delta(t) \quad P_i = \int f_i(t) dt = \frac{q_i}{\mu} \int v dt \approx \frac{q_i R}{\mu} \quad (11.8)$$

where  $\mu$  is the ion mobility. The resultant force on the wire in the  $y$  direction from one particle track can now be written as

$$F_i(x, t) = \sqrt{K} \frac{R}{\mu} \sum_i Q_i \delta(t - t_i) \delta(x - x_i) \cos \phi_i \quad (11.9)$$

where  $Q_i$  is the total charge of one event,  $x_i$  is the position of the event along the wire,  $t_i$  is the time of the event,  $\phi_i$  is the incidence angle of the particle track (fig. 11.6) and  $K$  is a geometry factor depending on the distance of the track from the wire and the avalanche distribution around the wire. If the avalanche would completely surround the wire there would be no resultant force at all. The avalanche distribution around the wire depends on the gas mixture, the gas gain and the wire diameter. For our  $50\mu m$  wire and the low gas gains ( $2 \times 10^4$  to  $6 \times 10^4$ ) the avalanche spread around the wire is only small and we can assume that the ion drift lines are the same as the drift lines of the primary electrons.

With this assumption the value for  $K$  for a localised charge deposit in the MDT would be  $K = 1$ . For particle tracks there is a geometry factor since for particle tracks through the

Voltage	gas gain	rms ampl. 13kHz	rms ampl. 400kHz
3300 V	$1.8 \times 10^4$	$< 2\mu m$	$< 11\mu m$
3400 V	$3.5 \times 10^4$	$2.5\mu m$	$< 14\mu m$
3450 V	$4.4 \times 10^4$	$5\mu m$	$< 28\mu m$
3500 V	$5.3 \times 10^4$	$6.5\mu m$	$< 35\mu m$

Table 11.1: Measured rms wire amplitudes for a counting rate of 13kHz (over a distance of 10cm) and extrapolation to 400kHz for the gas  $Ar/N_2/CH_4$ 91/4/5.

center of the tube there is no resultant force, but tracks close to the wall will cause a force. Averaging over all track distances gives a value of  $K \approx 0.4$ .

Solving equation (11.1) with (11.9) as a source term and averaging over time and positions one arrives after a long calculation at an rms value for the wire position of

$$\bar{U} = \sqrt{\frac{1}{L} \int_0^L \overline{y^2(x,t)} dx} = \frac{\bar{Q}R}{\mu} \sqrt{\frac{KK_1K_2\nu}{12T_0\rho_0\Gamma}} \quad (11.10)$$

where  $L$  is the wire length,  $\bar{Q}$  is the average charge per event,  $K_1 = \overline{\cos^2 \phi}$  depends on the angular distribution of the tracks,  $\nu$  is the particle rate and  $K_2 \approx 1$  for radiation flux distributed uniformly over the tube length and  $K_2 \approx \frac{3}{2} \left[1 - \left(\frac{2s}{L}\right)^2\right]$  if the tube is irradiated only at a distance  $s$  from the tube center. Note that the rms amplitude does not depend on the wire length but only on the total count rate.

Fig. 11.6 shows the setup for the vibration measurement. A Sr90 source with an activity of 30MBq was used to illuminate the tube over a length of 10cm. The average energy deposit from the Sr90 beta electrons in the MDT filled with 3 bars of Argon is 35-40keV and is close to the average energy deposit that we expect from the high energy photons in ATLAS. Formula (11.10) gives the rms deviation of the wire averaged over the whole tube length. Since the wire amplitude was only measured in the middle of the tube it is not easy to connect the measurements with the theory. Also it is not easy to judge the rms amplitude of the randomly vibrating wire by eye. We therefore measure the amplitude that is exceeded for less than 5% of the time, which was interpreted as  $2 \times$  the rms amplitude. The gas gain was corrected for the gain loss due to space charge effects. The results are shown in tab. 11.1.

We have to keep in mind that the values in this table are worst case numbers since they show the rms amplitude in the middle of the tube with the source positioned in the middle as well. Distributing the 400kHz rate over the whole tube length and averaging the amplitude over the whole tube length will give a reduction factor of  $\approx 0.5$ .

To check if the amplitudes change with the gas mixture, the same study was done with an  $Ar/CO_2$ 90/10 mixture. The results were very similar to the  $Ar/N_2/CH_4$ 91/4/5 mixture.

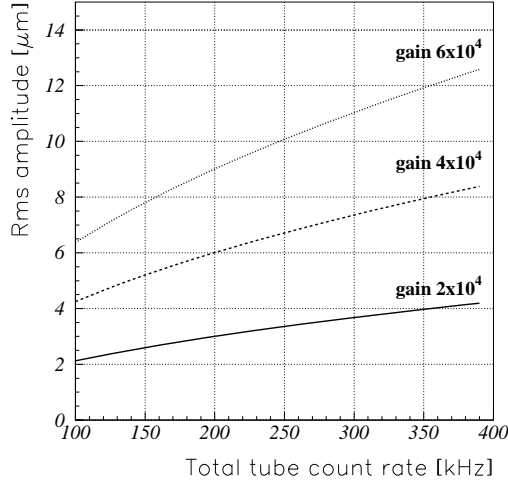


**Figure 11.7** : Rms wire amplitudes as predicted by the model assuming an average energy deposit of  $32keV$ .

The count rate in the MDTs will be dominated by tracks from high energy photons depositing an average energy of  $32keV$  isotropically in the tube. The parameters that determine the wire amplitude rms for this environment are

$$\begin{array}{lll}
 Q = Gain \times 32keV/26eV \times 1.609 \times 10^{-19}C & \mu = 0.55 \times cm^2/(Vs) & R = 1.5cm \\
 K = 0.4 & K_1 = 0.5 & K_2 = 1 \\
 T_0 = 350g & \rho = 19.26(25 \times 10^{-4})^2\pi g/cm & \Gamma = 2\pi 0.4s^{-1}
 \end{array}$$

Fig 11.7 shows the rms amplitude versus total count rate of the tube as predicted by (11.10).

From the measurements and the models we can conclude that up to a gas gain of  $4 \times 10^4$  the rms wire amplitude will not exceed  $20\mu m$  for the worst case flux expected in ATLAS. However the streamer rate should be as low as possible since streamer pulses normally contain a considerable amount of charge ( $10 - 100 \times$  the charge of proportional pulses) producing increased force on the wire. Still there is evidence that in streamer mode the avalanche starts to surround the wire, so the resultant force on the wire by a streamer pulse could be reduced by this effect.

### 11.3 Externally induced vibrations

The problem arising from externally induced vibrations in the experiment is difficult to quantify since we do not know what kind of vibrations to expect. However we can provide a few comments about the vibration issue. In big experiments the vibrations are mainly due

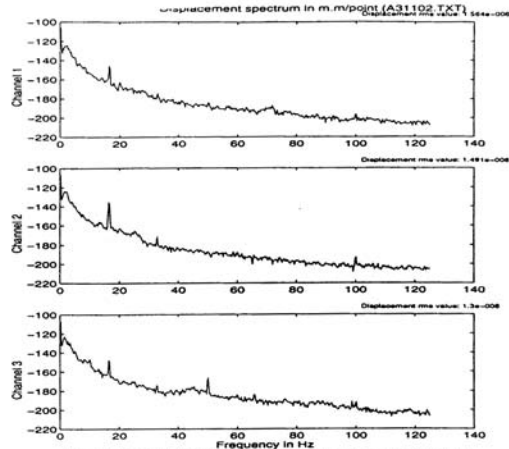


Figure IV.3: Spectral density (in dB) of the movements with field/beam

**Figure 11.8** : Vibration spectrum measured on the support structure of the ALEPH TPC [36]. The three figures show the acceleration spectrum in three orthogonal directions. An interval of 20dB corresponds to a factor 10 in acceleration. The peak at 16.3 Hz is equivalent to a sinus of  $0.36\mu\text{m}$  amplitude and is caused by cryogenic pumps connected to the structure. We see that from 20Hz to 40Hz the acceleration drops by more than 20dB which is a factor 10 in acceleration and a factor 40 in amplitude ( $a = A_0\omega^2$ ).

to pumps, ventilators and the flow of liquid in pipes. The amplitude spectrum typically falls off strongly up to a frequency of 50Hz, so to have wire resonant amplitudes in a range below 50Hz can cause a problem. Fig. 11.8 shows the vibration amplitude spectrum measured on the support structure of the ALEPH TPC [36]. Since not only the wires but also the MDT chambers have resonance frequencies in the 20-40Hz range it is very important to avoid coupling of the wire to the chamber modes. Fig. 11.9 shows an example of coupling of tube and wire resonance. The piezo element was moved towards the center of the tube. At the distance where the part of the tube between the piezo and the tube has a resonance frequency that is equal to the wire resonance frequency the amplitude is increased by a factor 7. Supporting the tube at the points where the wire is fixed one forces the tube to have a node at the same point where the wire has a node, so also if the tube would have the same resonance frequency as the wire, the two would have no influence on each other to first approximation. By putting a wire locator in the middle of the tube one would raise the wire resonance frequency by a factor 2 but one would couple tube and wire strongly which could cause a problem.

Two vibration tests with the 3.8m tube were done at experiment sites at CERN, one in the UA1 pit where the DATCHA setup is placed [37] and one test was done at the ALEPH experiment.

The support structure for the MDT chambers at DATCHA is a huge frame of concrete blocks. There are no vibrating elements attached to this structure, so this test intended to check if the ground floor vibrations would cause any vibration of the wire. All tests showed

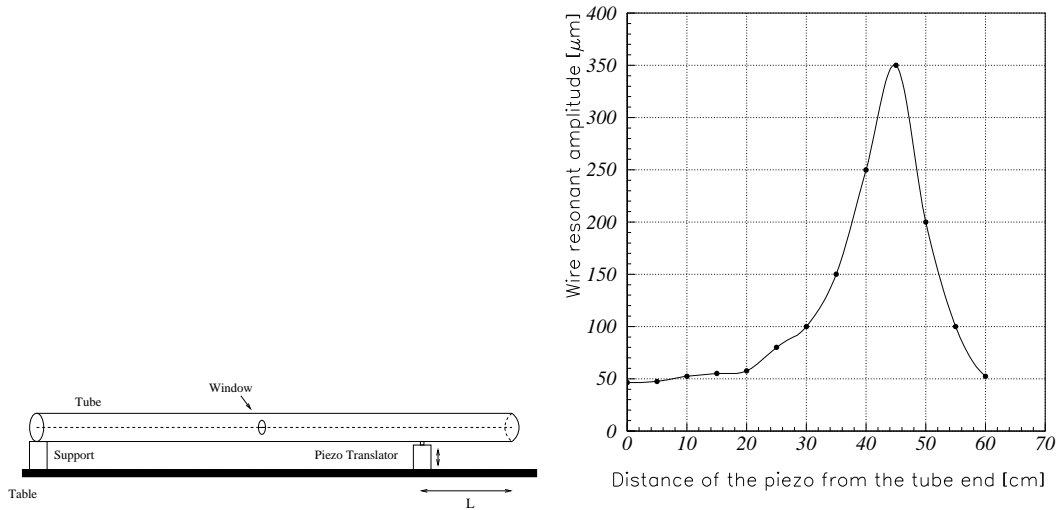


**Figure 11.9** : *By coupling the tube resonances to the wire resonances the wire amplitude increases by a big factor.*

no measurable wire amplitude. In case people were walking on the structure amplitudes up to  $20\mu\text{m}$  could be observed.

The measurement in ALEPH was done on a platform on which transformers and pumps are localised and one could definitely feel the floor vibrations. The 3.8m tube was supported at both ends and an amplitude of  $\approx 20\mu\text{m}$  was observed. By moving the supports away from the tube ends the wire amplitude increased up to  $250\mu\text{m}$  which again shows that coupling of the chamber resonances to the wire resonances is dangerous.

These two examples should just give a feeling for the size of the problem, the extrapolation to the ATLAS experiment is very difficult. One may also not rely on damping of the chamber supports since damping of frequencies as low as 25Hz is very difficult.

To quantify the problem better, the following procedure would be appropriate:

- Assuming that there will not be a middle wire locator in the tubes and that the tube ends are very close to the chamber support we can assume that the chamber and the wire modes are decoupled.
- The wire movement for a given movement of the support structure can be modelled by moving the two ends of a string with the given vibration spectrum which can be done with a finite element program like ANSYS.
- The vibration spectra for the simulation should be taken from measurements at sites that are considered representative for the conditions in the ATLAS detector.



# Chapter 12

## MDT efficiency

### 12.1 Introduction

Inefficiencies in the MDTs are due to two main reasons:

- The induced current signal stays below the threshold or the threshold exceeds the first maximum following the leading edge (fig. 12.1).
- A particle which is either created by the muon along its track or is coming from some other source deposits charge in the MDT at the same time as the muon such that the leading edge of the corresponding signal precedes the muon leading edge. The signals of the 2 events overlay and the muon track is lost (fig. 12.2).

The inefficiency due to signals not exceeding the threshold is negligible in our case since the signal to noise ratio is very high for our choice of gas gain and pressure (3 bars, gas gain  $2 \times 10^4$ ).

Shadowing of the muons by signals from other particles is a more serious problem. There is a fundamental efficiency limit from delta electrons created by the muon in the tube wall or the counting gas.

Another source of inefficiency are tracks from uncorrelated background particles like neutrons and photons. This kind of inefficiency clearly is background rate dependent.

Using strong tail cancellation filters or two discriminators with different thresholds one can identify 'piled up' leading edges and increase the efficiency.

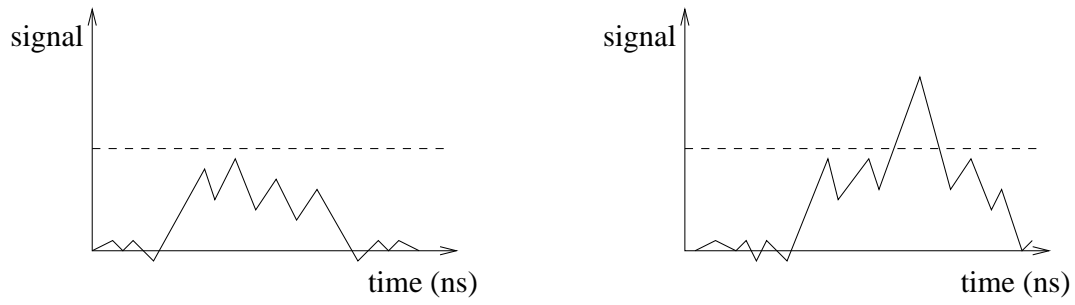


**Figure 12.1** : Inefficiency due to signals staying below the threshold and signals where the threshold misses the leading edge.

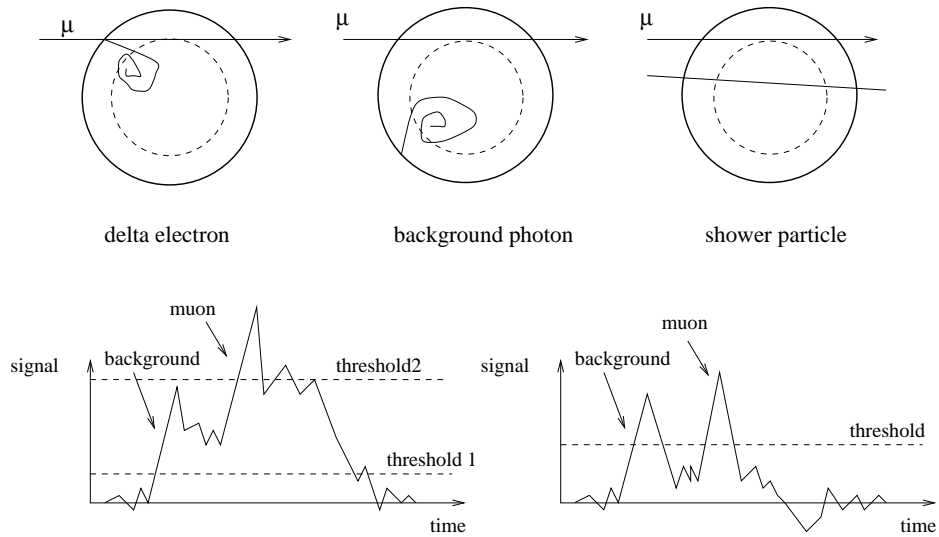


**Figure 12.2** : Inefficiency due to a particle shadowing the muon. A second discriminator or strong tail cancellation together with a higher threshold can help to recuperate some of the shadowed hits.

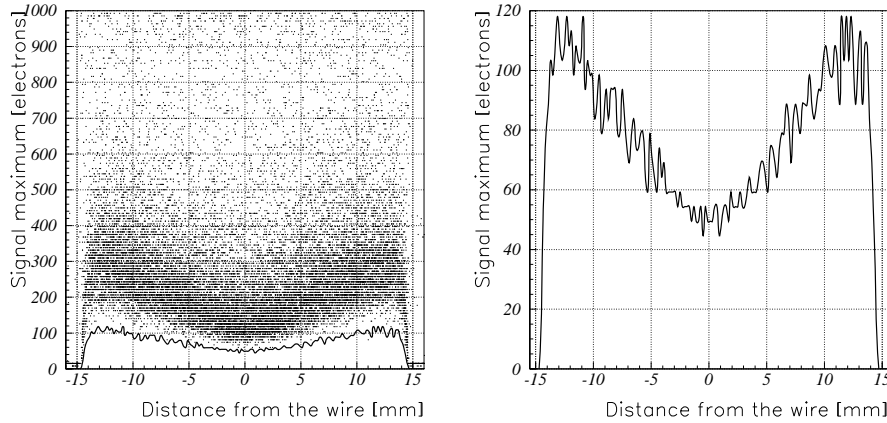


**Figure 12.3** : Signal maxima versus distance of the track from the wire. The left figure shows all the events. 99.5% of the pulses are larger than the values indicated by the solid line. The right figure shows a magnification of this line.

## 12.2 Inefficiency due to signals not exceeding the threshold

The setup for the measurement was already described in chapter 5. Fig. 12.3 shows the signal maxima versus position of the muon track. The average pulse height increases towards the tube wall and then falls off steeply because the track length goes to zero. 99.5 % of the pulse heights are larger than the values indicated by the solid line. The reason for the increase of pulse height towards the wall can be seen from fig. 12.4.

By fitting a straight line to both edges of the curve shown in fig. 12.3 we find the region where the MDT starts to be efficient (fig. 12.5).

Up to a threshold of 40 electrons the central region of the tube is very efficient ( $\epsilon > 99.5\%$ ). However we have to be careful in interpreting this since the signal maximum is not necessarily the maximum following the leading edge, in fact it can be anywhere within the whole signal (fig. 4.8). The interesting number is the fraction of hits outside  $3\sigma$  and  $5\sigma$  of the resolution. These values are discussed in the next chapter.

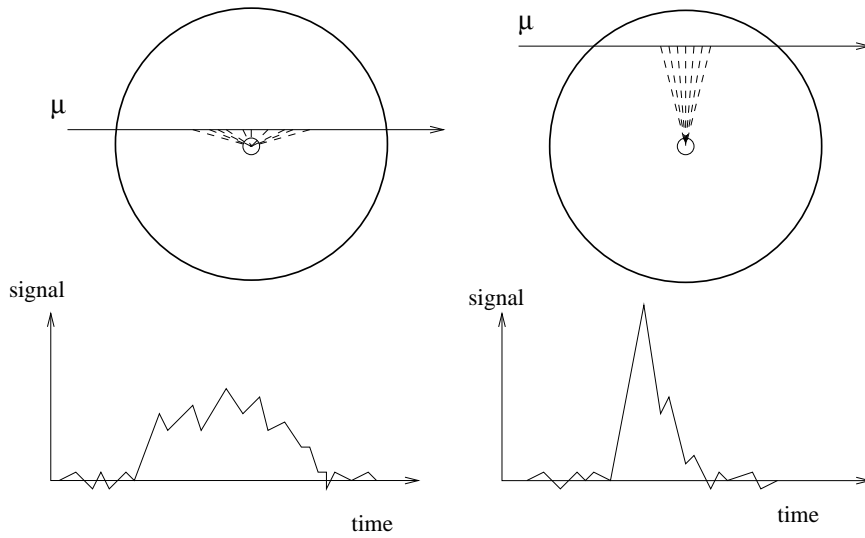


**Figure 12.4** : Charge focusing effect. For tracks close to the wire the electrons come in 'one after the other', whereas for tracks far from the wire most of the charge arrives instantaneously at the wire which results in an increased pulseheight.

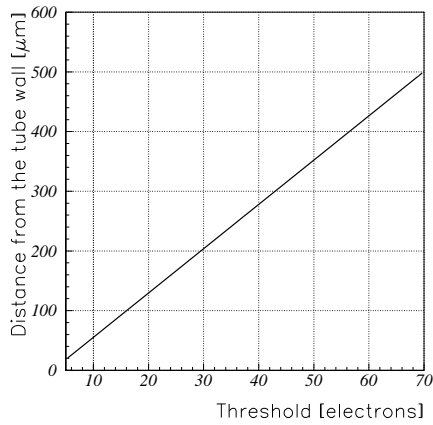


**Figure 12.5** : This graph indicates the distance from the tube wall where the hit-efficiency is 99.5%.

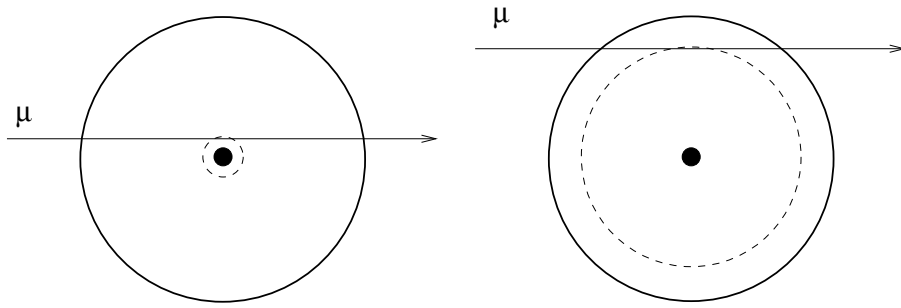


**Figure 12.6** : Only if a secondary particle from the tube wall or the counting gas enters the region indicated by the circle it will hide the muon. There can not be any inefficiency from secondaries for tracks very close to the wire.

### 12.3 Inefficiencies due to electromagnetic secondaries and charge fluctuations

Secondary particles that are created in the tube wall or the gas deposit the charge at the same time as the muon. They can only spoil the muon hit if the corresponding signal precedes the muon leading edge by more than  $2 - 3\sigma$  of the MDT resolution (fig. 12.6). By definition there can not be any inefficiency from secondary particles for tracks through the center of the tube.

For tracks close to the wire, where the charge arrives at the wire only within a long time, one loses the signal leading edge by using high thresholds.

We define an event as inefficient if the position, predicted by the  $rt$ -relation, is outside  $3\sigma$  or  $5\sigma$  of the position predicted by the silicon telescope where  $\sigma$  is the MDT resolution at the given position for the given threshold. The resolution for different thresholds can be seen in fig. 12.7.

Fig. 12.8 shows the track positions versus threshold crossing time for different thresholds. The width of the 'V-band' corresponds to the MDT resolution. The two types of inefficiencies are immediately visible from these plots:

- The points 'below' the curve correspond to hits from delta electrons. The number of them is almost independent of the threshold.
- The hits 'above' the curve correspond to events where the threshold exceeds the first leading edge. This kind of inefficiency is of course threshold dependent.

To check whether the inefficiency is due to shower particles coming with the muon in the beam one counts the events that are inefficient in two adjacent tubes for the same event. About 0.8% of all events were inefficient in both tubes. Whether this is due to shower

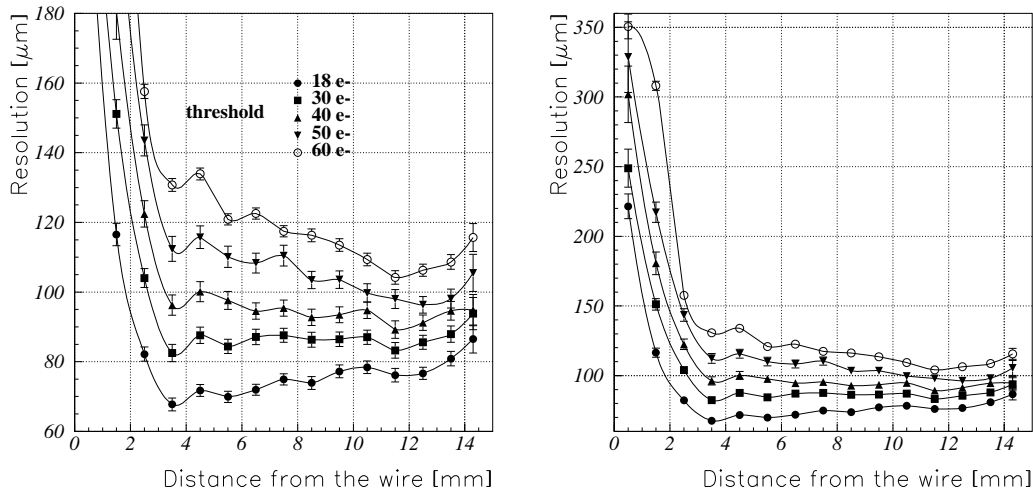


**Figure 12.7** : MDT resolution for different thresholds. The right figure shows the same plot on a different scale to indicate the decreased resolution at the wire.

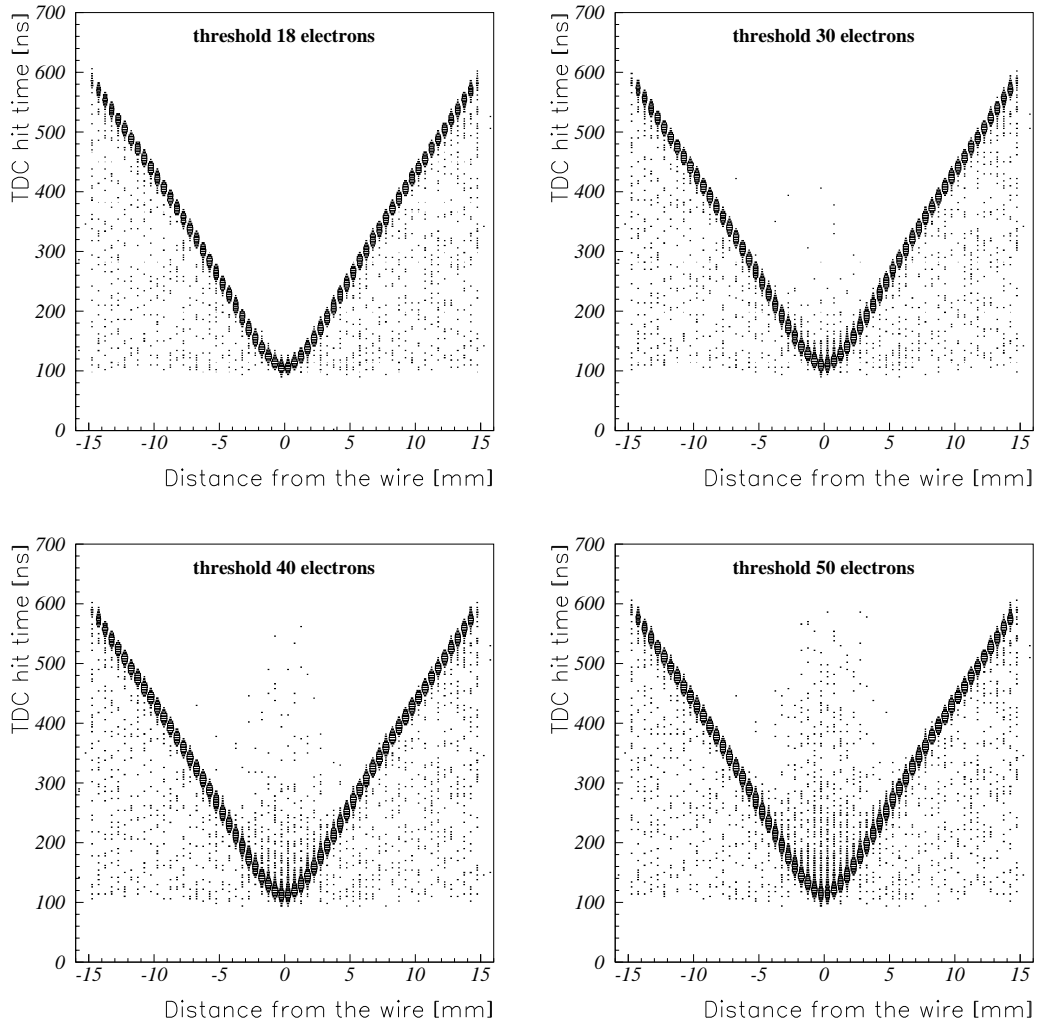
particles or due to particles created by the muon in the first tube cannot be answered with this setup.

Fig. 12.9 shows some of the events where a delta electron spoiled the muon hit. Fig. 12.10 shows the inefficiency versus drift distance for different thresholds.

Fig. 12.11 shows the total inefficiency i.e. the fraction of hits outside  $3\sigma$  and  $5\sigma$  of the predicted position for the entire tube range ( $-14.6\text{mm}$  to  $14.6\text{mm}$ ).

We conclude:

- For the nominal threshold of 20 electrons the muon efficiency i.e. the probability that the muon signal exceeds the threshold is very close to 100% if the muon crosses the tube at a distance of  $> 150\mu\text{m}$  from the wall.
- The inefficiency due to secondaries created by the muon in the tube wall or the counting gas is 6-7% and is independent of the threshold (7% of the hits outside  $3\sigma$  and 6% of the hits outside  $5\sigma$  of the position).
- The inefficiency due to the fact that the threshold exceeds the leading edge is negligible for a threshold of 20 electrons but increases by raising the threshold, so a threshold above 20 electrons is not recommended.



**Figure 12.8** : TDC hits versus track position. The hits 'below' the curve are delta electrons hiding the muon track. The hits 'above' the curve indicate events where the threshold exceeds the first maximum following the leading edge.

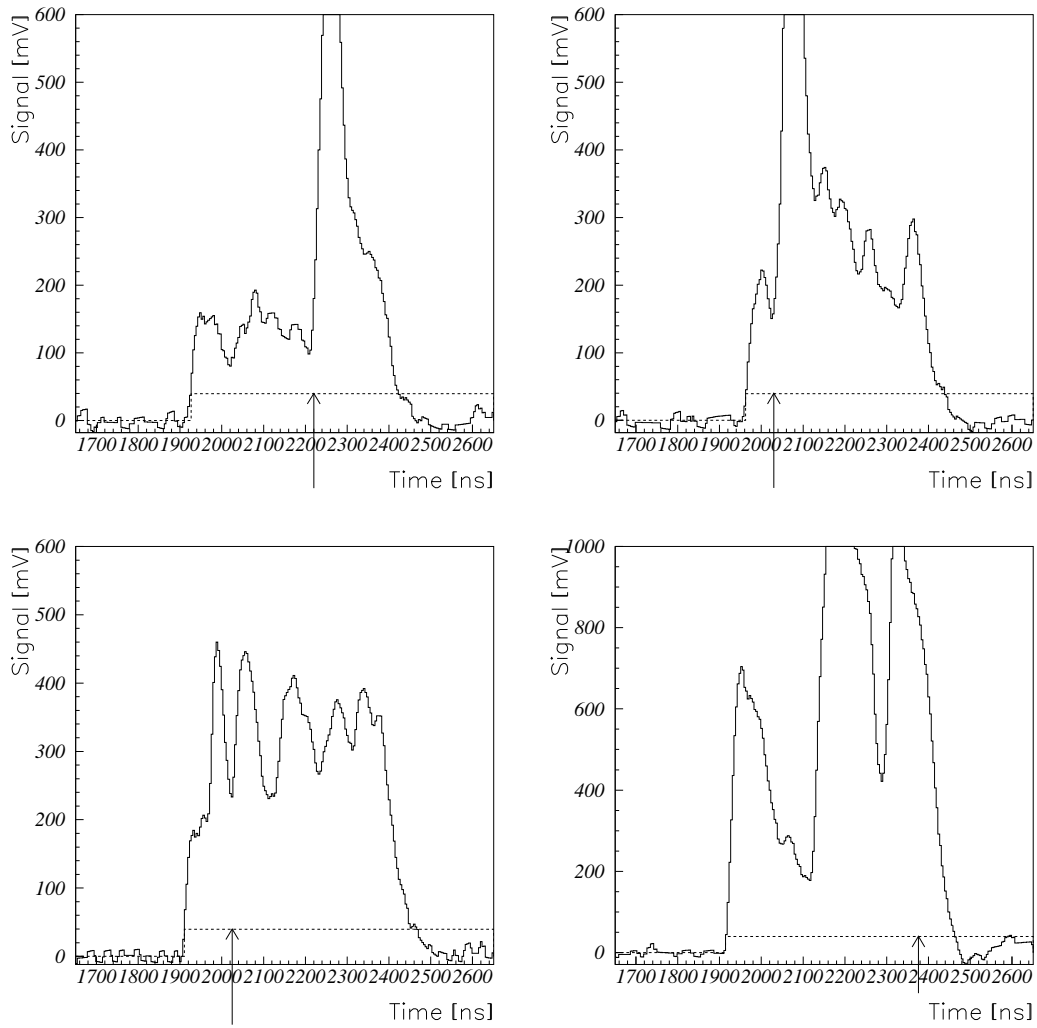


**Figure 12.9 :** Events where a delta electron shadows the muon hit. The horizontal line indicates the threshold of 18 electrons. The arrow indicates the hit time expected from the silicon telescope (calculated from the  $rt$ -relation).



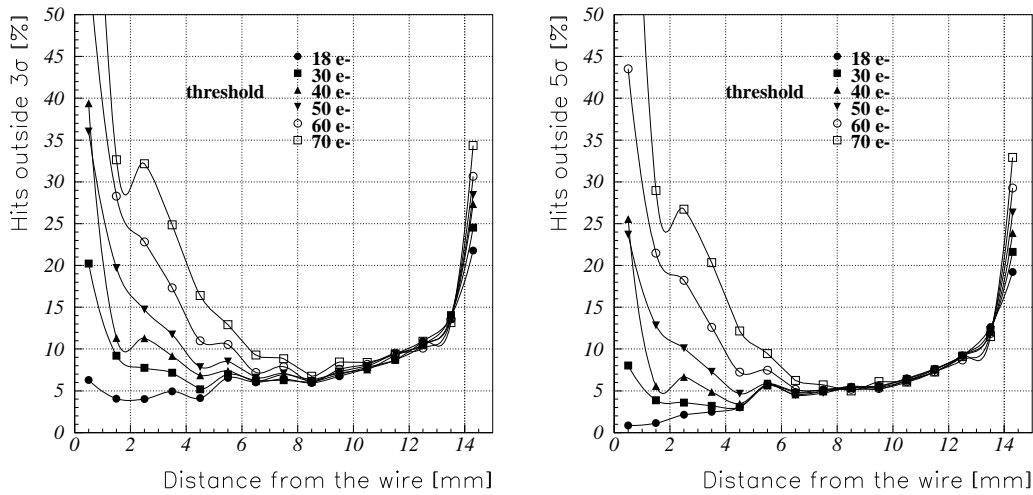


**Figure 12.10** : MDT inefficiency for different thresholds. The inefficiency for a threshold of 18 electrons is only due to delta electrons. By raising the threshold one starts to lose leading edges for tracks close to the wire and one also starts to exceed the pulses close to the wall. The points were evaluated in 1mm bins from 0mm to 14mm, the last point corresponds to a bin from 14mm to 14.6mm.

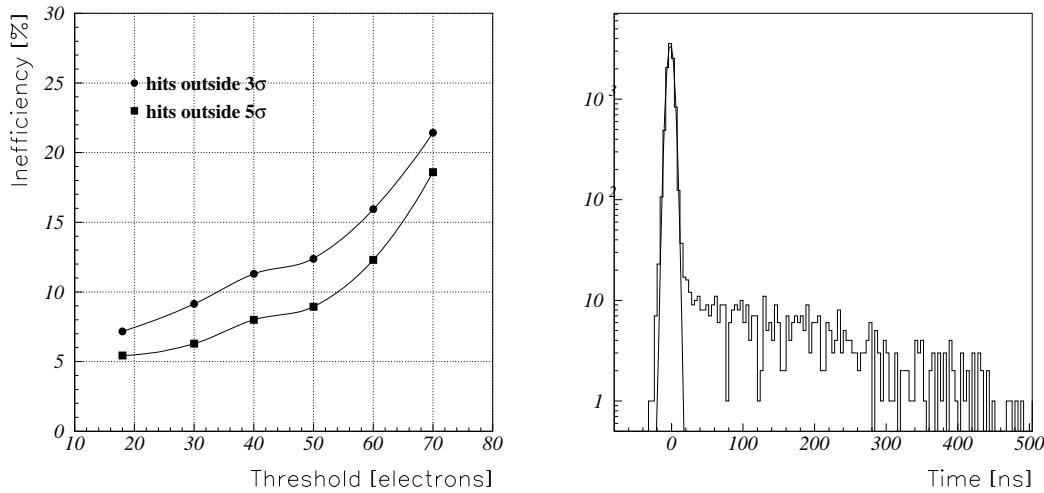


**Figure 12.11** : Total inefficiency for different thresholds. It is defined by the fraction of hits outside  $3/5\sigma$  of the position, predicted by the silicon telescope, in the entire region from  $-14.6\text{mm}$  to  $14.6\text{mm}$ . The right figure shows the difference of expected hit time (calculated from the silicon telescope track via the  $rt$ -relation) and the actual hit. The width of the peak corresponds to the resolution, the tails are the hits from delta electrons shadowing the muon. The small tails to the left are due to the reduced resolution at the wire.

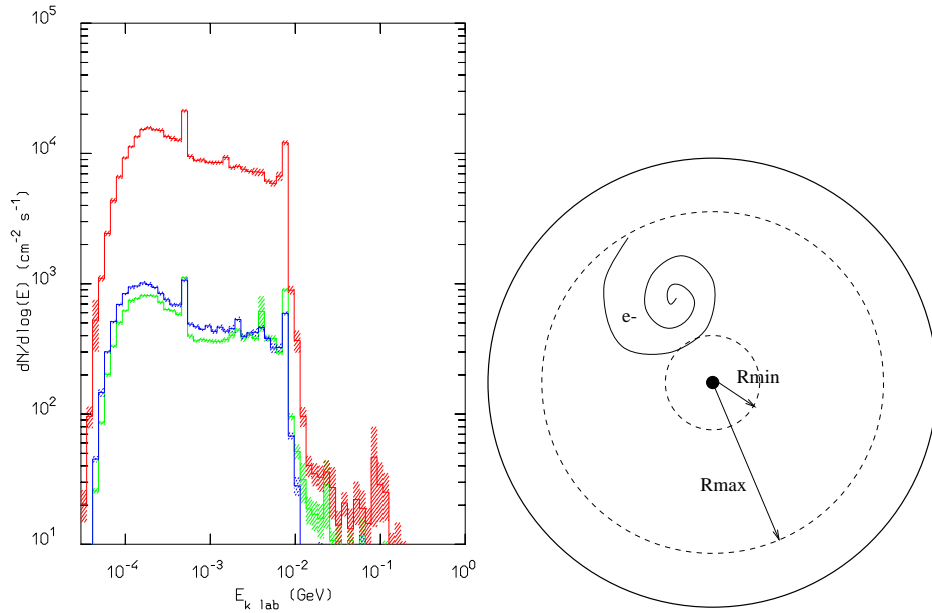


**Figure 12.12** : Photon spectrum for the barrel region. The high energy photons will mostly create Compton electrons. The numbers that determine the dead time are the outer and the inner enveloping radius of the track created by the electron.

## 12.4 Inefficiencies due to uncorrelated background

### 12.4.1 Background characteristics

All calculations on the characteristics of the uncorrelated background were done by A. Ferrari [38]. Fig. 12.12 shows the expected background photon spectrum for the ATLAS muon spectrometer. This spectrum has to be folded with the sensitivity of the detector gas and aluminium tubes. The relevant numbers for the dead time spectrum are the outer and inner enveloping radius of the background track (fig. 12.12) and the energy deposit. These numbers were calculated the following way:

1.  $6 \times 10^6$  photons were randomly taken from the above spectrum.
2. The photons were sent isotropically through 3 layers of 14 Al tubes ( $400\mu m$  wall) filled with 3 bars (absolute) of  $Ar/N_2/CH_4$  91/4/5. The magnetic field was assumed to be 0.4T parallel to the wire.
3. The inner and outer enveloping radius of the charged particle track together with the energy deposit were calculated for each interacting photon.

Fig. 12.13 shows the results of the calculation. The histogram showing the  $R_{max}$  distribution indicates that most of the electrons created by the background photons either come out of the tube wall or dump in the tube wall.

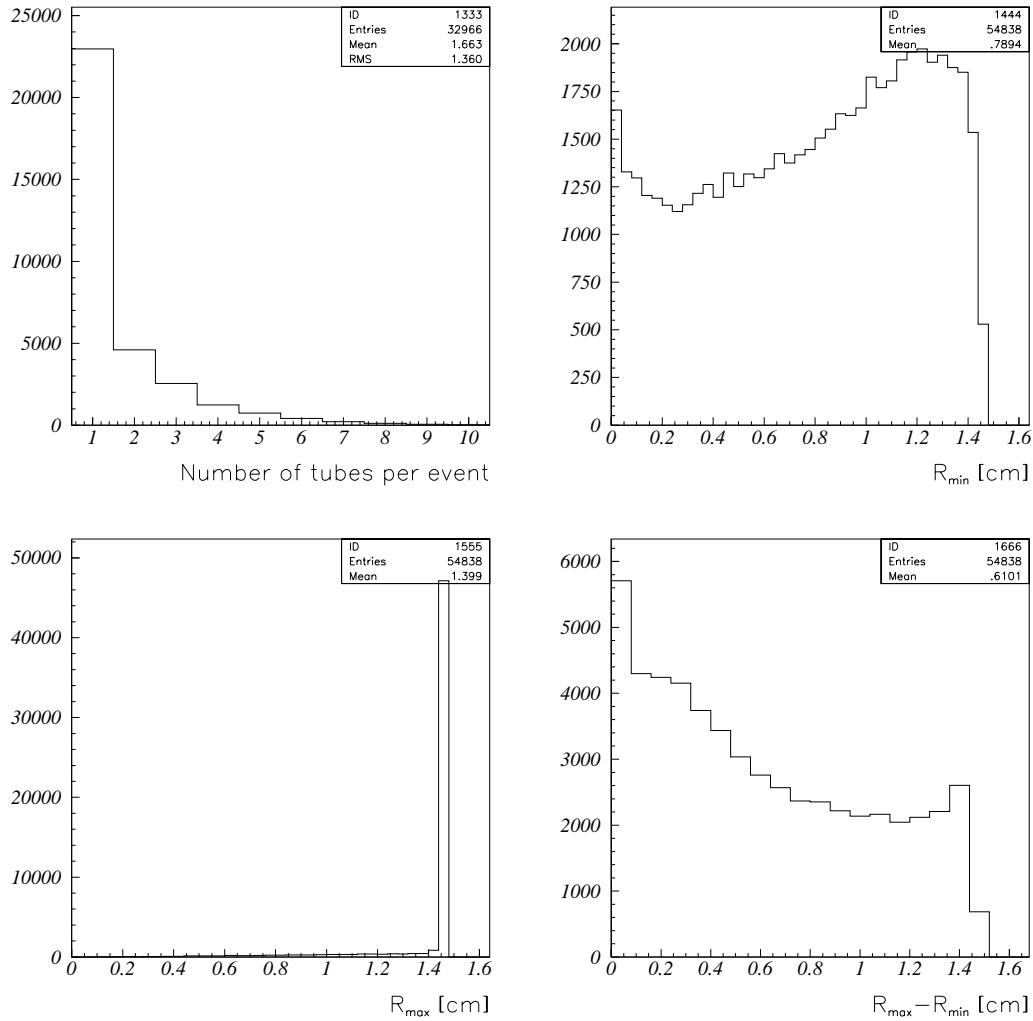


**Figure 12.13** : The first figure shows the number of tubes which are hit by a single background event. We see that many of the Compton electrons have enough energy to cross the tube walls and deposit charge in more than one tube. For explanation of the other histograms see fig. 12.12. The outer enveloping radius of the track is almost always equal to the tube radius which indicates that the Compton electrons either 'come out of the tube wall' or, when created in the gas, 'dump in the wall'. The simulations were done for a magnetic field of 0.4T.

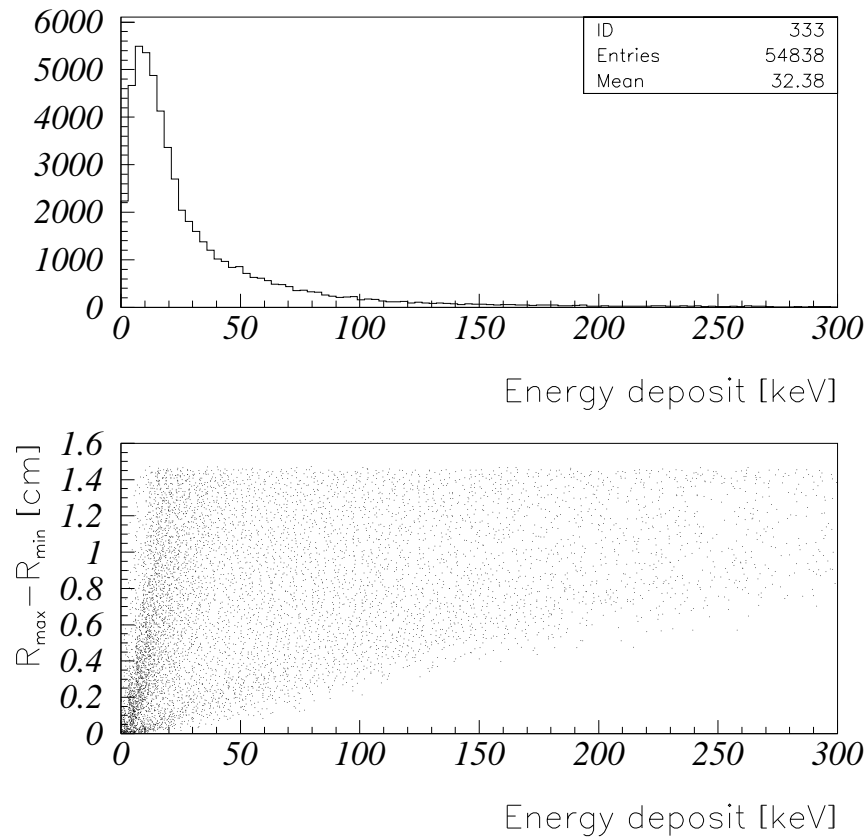


**Figure 12.14** : Energy deposited by background photons. The average energy deposit is 32keV which is about twice as much as the energy deposited by high energy muons perpendicular to the wire.

The energy deposit spectrum of the photon background can be seen from fig. 12.14. The average energy deposit is  $\approx 32\text{keV}$ .

## 12.4.2 Double track separation

For the nominal threshold of 20 electrons, inefficiencies are only due to secondary particles created by the muon or some other source. When the signal of the muon track 'piles up' with a signal from a background event, the muon leading edge may be lost.

Two schemes were studied to recuperate the 'piled up' signal:

1. a double threshold scheme,
2. a strong tail cancellation scheme

as pictorially shown in fig. 12.2.

To study these schemes a simulation was performed. Signals from muons and photons from a Bi207 source (0.57, 1.1, 1.8MeV gammas) were recorded with a FADC. Superimposing the signals and tail cancellation were performed in software. This provides a very realistic simulation of the case where there are really two tracks in the MDT since space charge effects, which could influence the different clusters, are negligible at the gain of  $2 \times 10^4$ . The experimental setup is the same as described in chapter 5. Typical signals from muons and Bi207 photons are shown in fig. 12.15.

The separation efficiency for a muon and a correlated background track perpendicular to the wire was determined the following way (note that in this case the two pulses have the same trailing edge):

- the leading edges of two muon pulses are determined;
- the two signals are superimposed;
- all leading edges ('hits') are determined;
- if the leading edge of the second pulse is within three times the rms spatial resolution of one of the 'hits' we call the two tracks separated.

The separation efficiency of a muon and an uncorrelated background event was simulated the following way:

- the photon pulse is shifted randomly within a window of  $2 \times$  maximum drift time;
- the leading and trailing edges of the muon signal and the photon signal are determined;

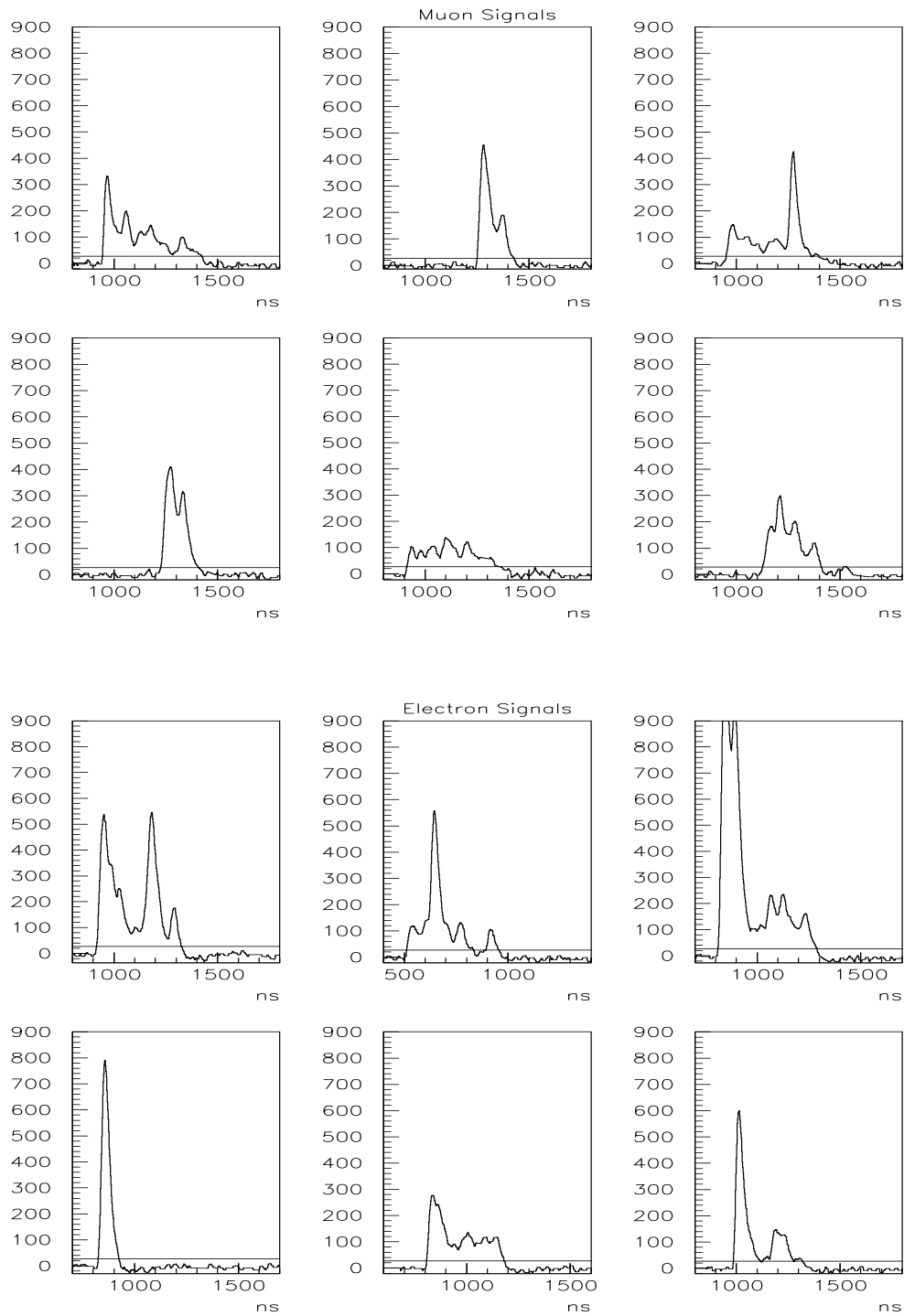


**Figure 12.15** : Typical muon signals and signals from Bi207 photons for a gas gain of  $2 \times 10^4$ . The horizontal line indicates the threshold of 20 electrons. The tail cancellation is done with a double pole/zero circuit. With a hysteresis of half the threshold the average number of hits per signal is very close to 1. Clearly if two of these signals pile up the second leading edge is lost.

- if the photon leading edge arrives before the muon leading edge and the last trailing edge of the photon signal arrives after the muon leading edge (only in that case we really have a shadowing event) the two signals are superimposed;
- all leading edges ('hits') are determined;
- if the leading edge of the muon signal is within three times the rms spatial resolution of one of the 'hits' we call the two tracks separated.

The results of the analysis for different front end schemes are discussed in the following sections.

### 12.4.3 Two filter scheme

The first schematic under study is given in fig. 12.16 [39]. It consists of two switchable filter chains, a time over threshold output and a leading edge+ADC output. Applying the strong tail cancellation filter and a high threshold we can perform double track separation. For this study, a filter consisting of three pole/zero stages with time constants of

$$\begin{array}{lll} \tau_1 = 200ns & \tau_3 = 200ns & \tau_5 = 1000ns \\ \tau_2 = 80ns & \tau_4 = 40ns & \tau_6 = 400ns \end{array}$$

was assumed. Fig. 12.17 indicates how this scheme works. Fig. 12.18 shows separation efficiencies for the overlay of two muon signals which corresponds to accompanying shower particles or other correlated background signals with tracks perpendicular to the wire. The separation efficiency is about 80%. The leading edge charge is encoded into a pulsewidth the following way: the discriminator output is set high when the signal goes above threshold, then the signal is integrated for  $20ns$  and the charge is stored on a capacitor. The capacitor is then discharged at a constant current and after crossing a certain threshold value the discriminator output is set low. Fig. 12.21 shows the separation efficiency for muons and electrons from background photons. The efficiency is only about 60% which is due to the fact that the isotropic electron tracks create signals that are about two times higher than the muon signals. Fig. 12.19, 12.20, 12.22 and 12.23 characterise the discriminator output. Fig. 12.24 shows the tendencies of hit numbers and resolution of the second hit versus threshold.

To find out if the separation efficiency depends on the preamplifier peaking time, the separation efficiency for muon pulses simulated with GARFIELD was studied for 3 different shaping times shown in fig. 12.25. The separation efficiency for  $t_p=5ns$ ,  $15ns$ ,  $30ns$  is almost identical. Increasing the peaking time reduces the number of hits but the resolution of the hidden track is reduced strongly ( $115\mu m$  for  $t_p=5ns$  and  $223\mu m$  for  $t_p=30ns$ ).

The performance of this scheme can be summarized as follows:

- for a threshold of 50 electrons the average number of hits per single signal is around 1.5. In case of a double track there are around 2.4 hits;
- the separation efficiency is  $\approx 80\%$  for a muon and a track perpendicular to the wire and  $\approx 60\%$  for a muon track and an isotropic background track if the leading edges are separated by more than  $80ns$ ;
- the resolution of the second track is  $150\mu m$  and  $175\mu m$  respectively;
- the separation efficiency does not depend on the preamplifier peaking time;
- however this scheme is not recommended since the principle track inefficiency for a threshold of 50 electrons is 9% compared to only 6% inefficiency for a threshold of 20 electrons as shown in fig. 12.11.



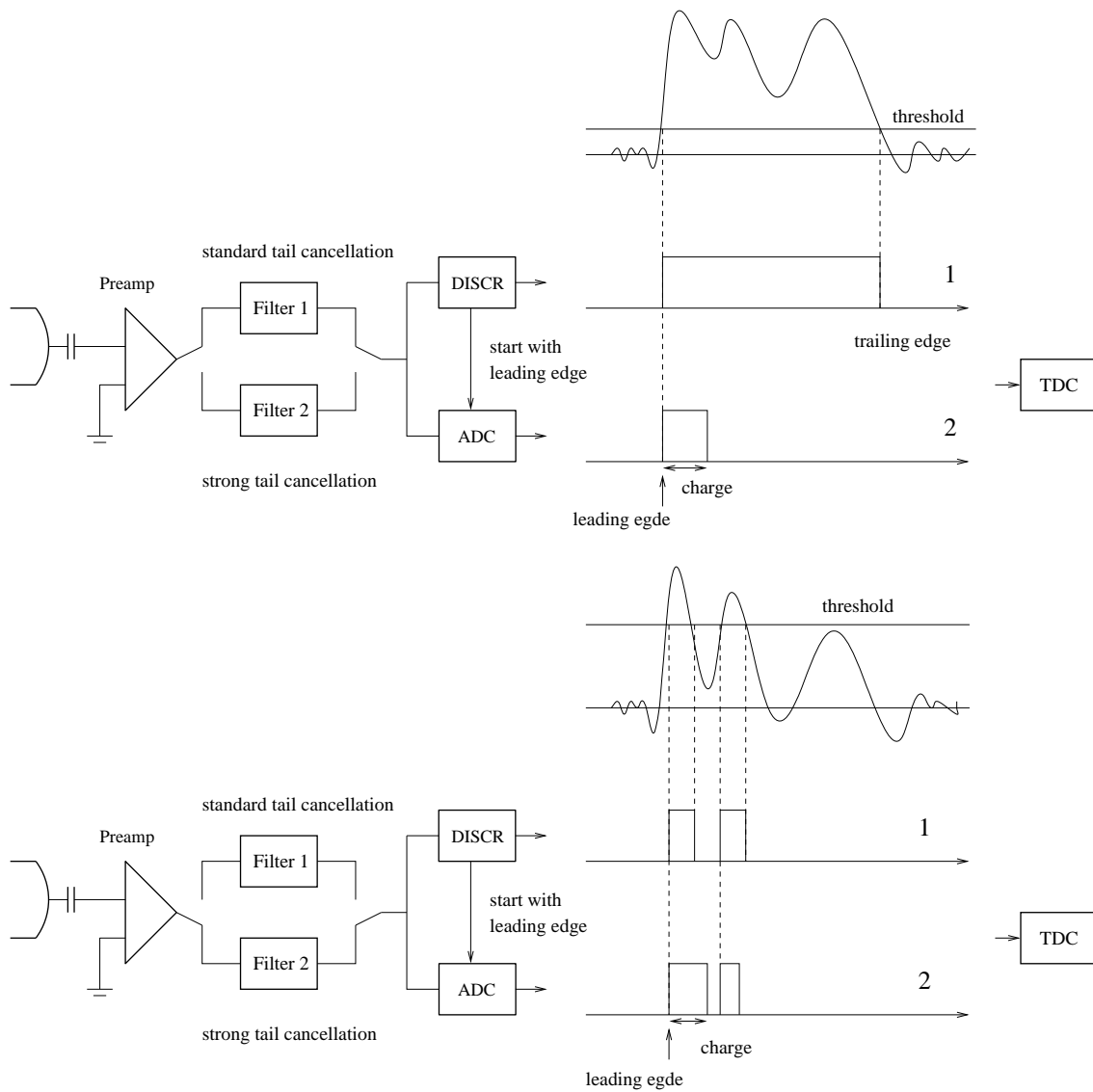


**Figure 12.16** : In this scheme the fronted electronics has two filter chains. In normal mode one would use the standard tail cancellation filter and a low threshold and one can optionally read leading and trailing edge or leading edge (1) and ADC (2). In case of high occupancies one would switch to the strong tail cancellation filter, apply a higher threshold without hysteresis and read out the leading edge and ADC channel (2). One would get acceptable double track separation efficiency with good leading edge resolution by recovering the loss in resolution due to the high threshold by applying a time slewing correction with the charge measurement.

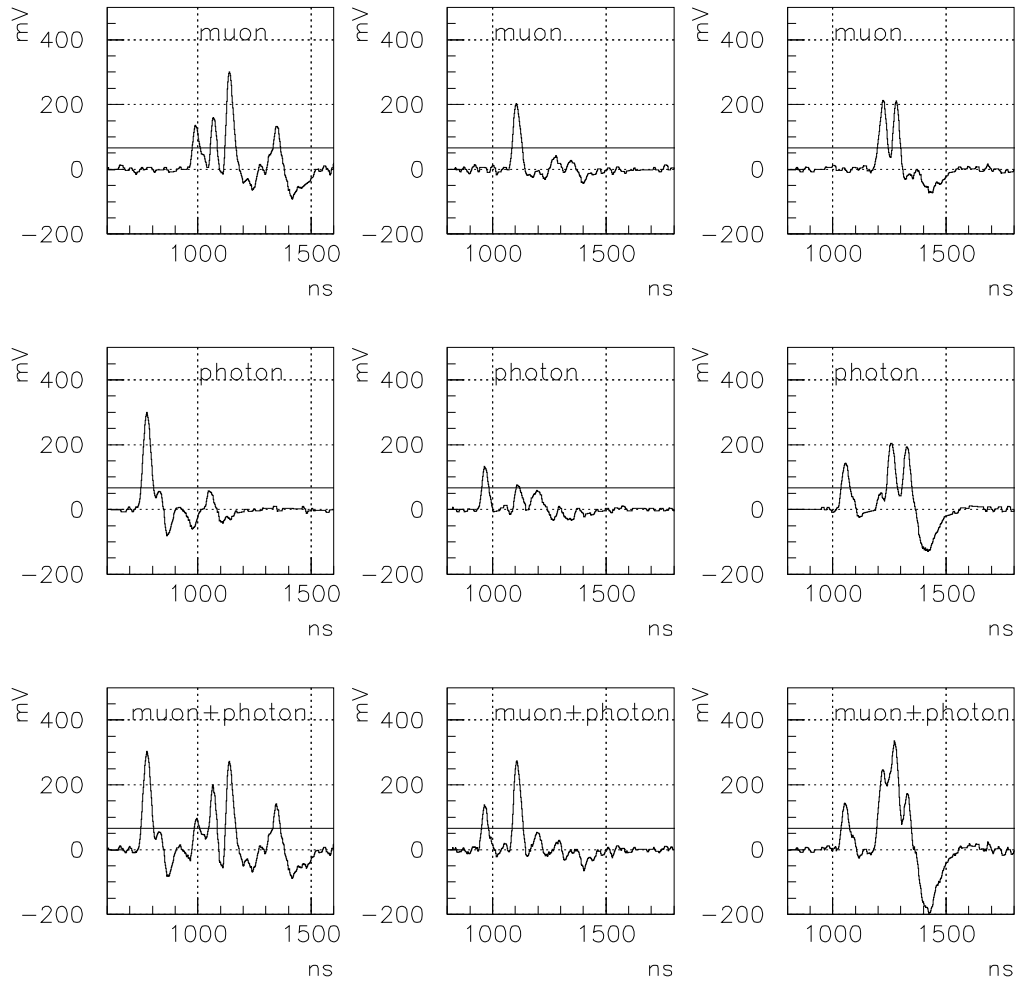


**Figure 12.17** : Using strong tail cancellation it is possible to find the muon leading edge even if it is 'piled up' with a photon background hit. The horizontal line indicates a threshold of 50 electrons.

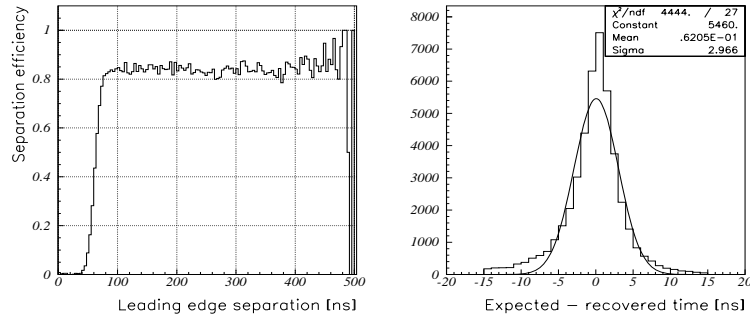


**Figure 12.18** : Separation efficiency for tracks perpendicular to the wire. The efficiency is close to 80%. The second histogram shows the additional bias in resolution for the overlaid track. For a gas with a drift velocity of about  $30\mu\text{m}/\text{ns}$  (like  $\text{Ar}/\text{N}_2/\text{CH}_4$  91/4/5) this would correspond to an additional bias of  $90\mu\text{m}$  which has to be added in quadrature to the nominal resolution at the given threshold.

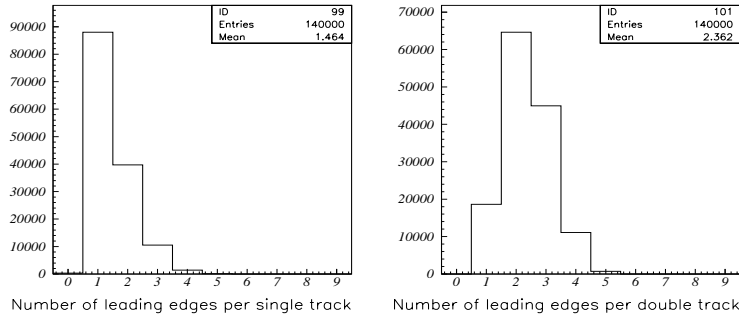


**Figure 12.19** : Average number of hits per single track and per double track.

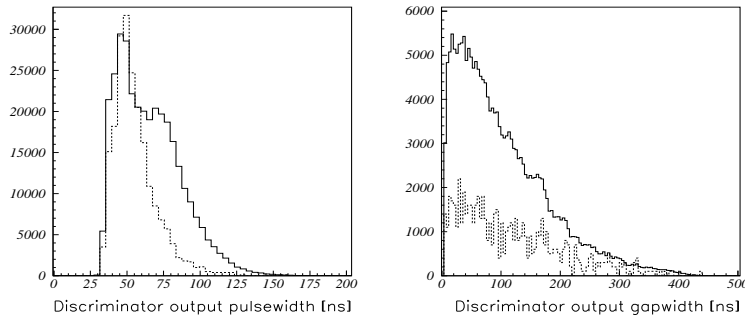


**Figure 12.20** : Pulse width and the time between the pulses ('gap width') of the discriminator output. The dotted line corresponds to single tracks, the solid line corresponds to double tracks. Note that these histograms show the pulse and gap width for the mode where the charge is encoded in the discriminator output. The gate assumed is 20ns and the charge information is converted into a time proportional to the charge.

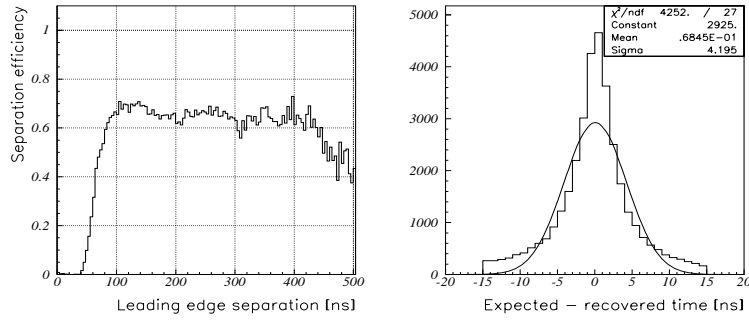


**Figure 12.21** : Separation efficiency for muons and pulses from Bi208 photons. The separation efficiency is lower due to the fact that the photon pulses are on average twice as high as the muon pulses. One can imagine that a 'small' muon pulse being hidden by a 'big' photon pulse is affected more than the muon-muon case in the previous figure. This can also be seen by the bigger bias in resolution.

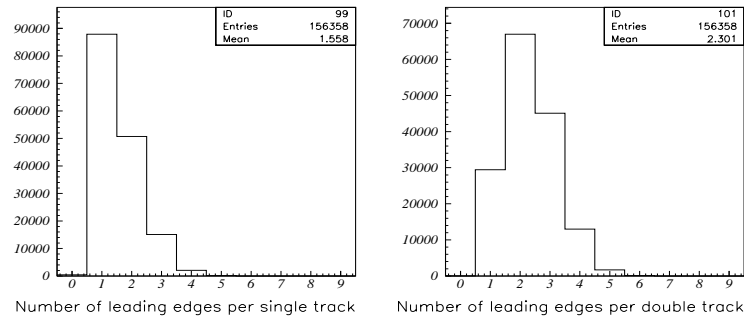


**Figure 12.22** : Average number of hits per single track and per double track.

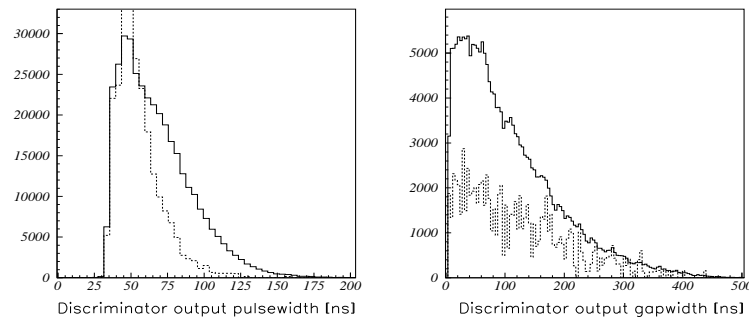


**Figure 12.23** : Pulse width and the time between the pulses (gap width) of the discriminator output. The dotted line corresponds to single tracks, the solid line corresponds to double tracks. Note that these histograms show the pulse and gap width for the mode where the charge is encoded in the discriminator output. The gate assumed is 20ns and the charge information is converted into a time proportional to the charge.

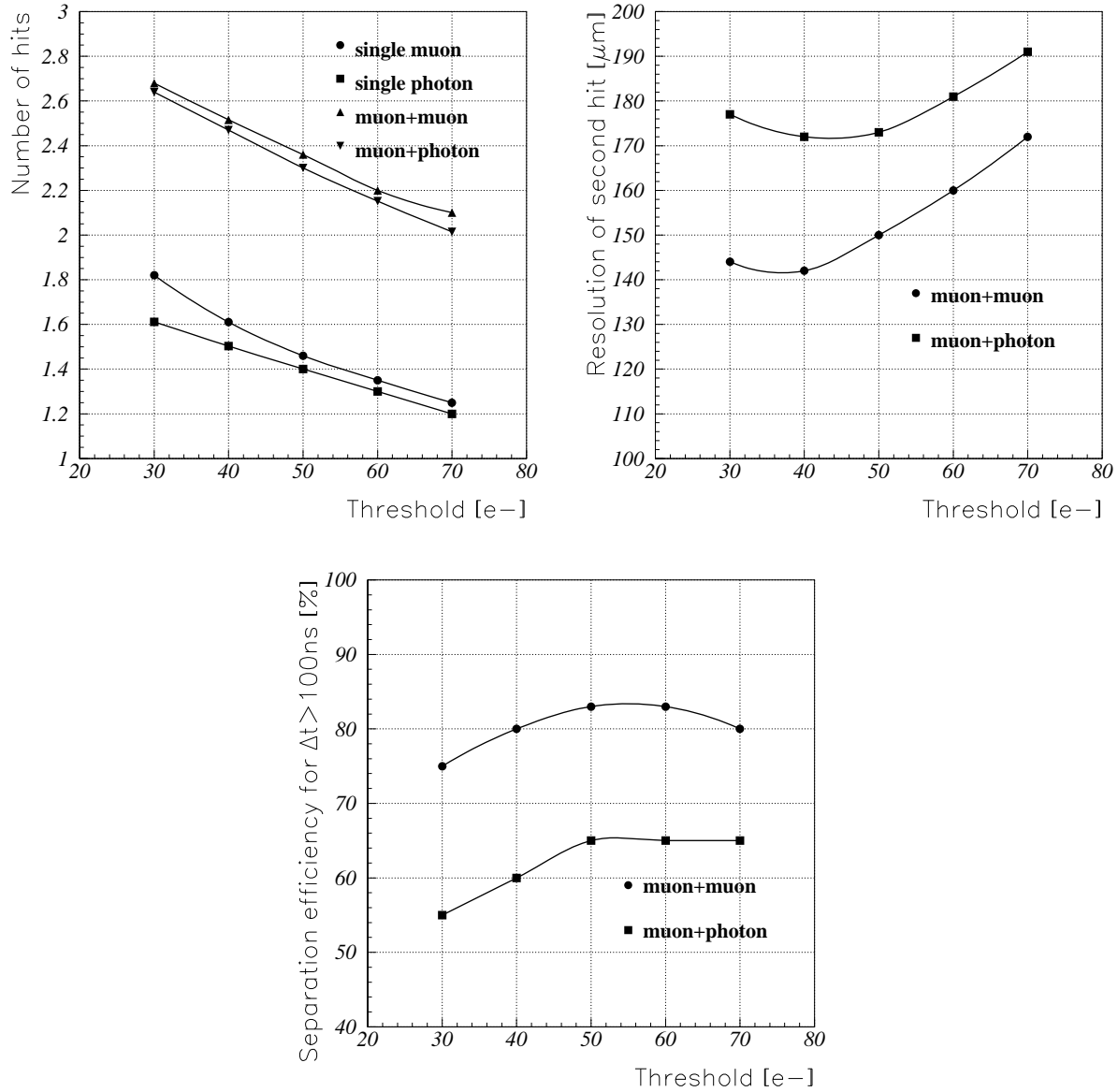


**Figure 12.24 :** Trends for hit numbers and resolution of the second hit for different thresholds. A higher threshold reduces the number of hits and also increases the separation efficiency. The resolution of the second hit is worse for the overlay of a muon and a photon since the photon pulses are higher.

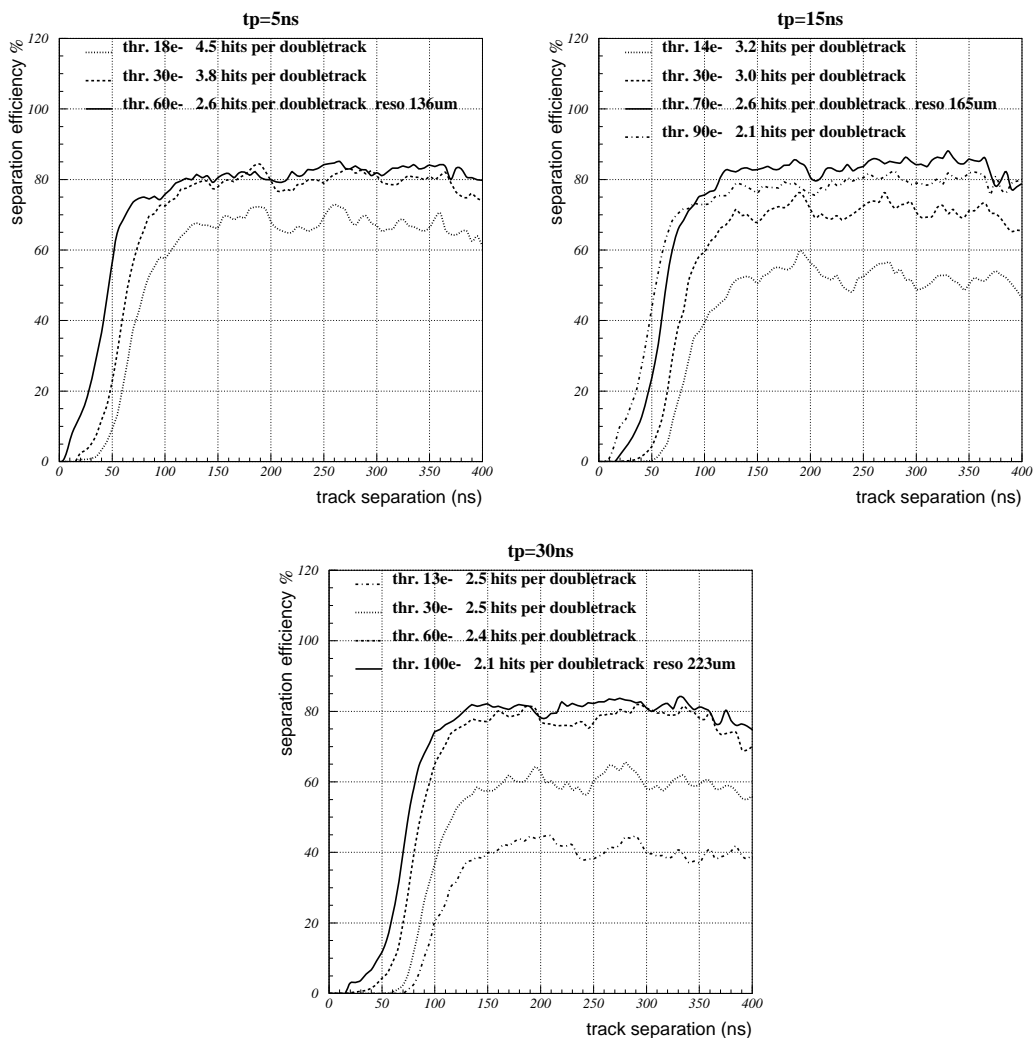


**Figure 12.25** : Separation efficiency for muons and tracks perpendicular to the wire as simulated with GARFIELD for three different preamplifier peaking times. The separation efficiency does not depend on the peaking time. The resolution of the recovered track is worse for long peaking times.

## 12.4.4 Two Discriminator Scheme

The second schematic under study and its functionality are given in fig. 12.26 and 12.27. The frontend electronics would contain two discriminators, one with a threshold set to the  $5\sigma_{noise}$  level for good spatial resolution and a second one with a threshold of  $\approx 120$  electrons to identify the 'piled up' leading edges. The advantage of this scheme is that we do not rely on the leading edge charge correction for good resolution like in the previous scheme. Fig. 12.28 and fig. 12.31 show the separation efficiencies for the overlay of two muon signals and muon signals with photon background signals. The separation efficiency is 10% better compared to the strong tail cancellation scheme. However, the leading edge recovered with the high threshold discriminator is systematically shifted since we determine the  $rt$ -relation with the low threshold hits. Since the shift is systematic we can correct for it. Fig. 12.29, 12.30, 12.32 and 12.33 characterize the discriminator output. Fig. 12.34 shows trends of separation efficiency, hit number and resolution of the second hit for this scheme.

Finally one can calculate the increase in efficiency when using a double track separation scheme (fig. 12.35), (12.36).

We conclude for the double threshold scheme:

- Using a second discriminator with a threshold of 120 electrons and performing an OR with the ADC channel gives on average 1.7 hits per signal.
- A threshold of 120 electrons for the second discriminator gives a separation efficiency of 95% for tracks perpendicular to the wire and 75% for a muon and a background photon if the leading edges are separated by more than  $\approx 100ns$ .
- The resolution of the second track is  $150\mu m$  and  $175\mu m$  for these cases. A correction for the systematic shift is necessary.
- This scheme is recommended since it is more efficient and reliable compared to the strong tail cancellation scheme.

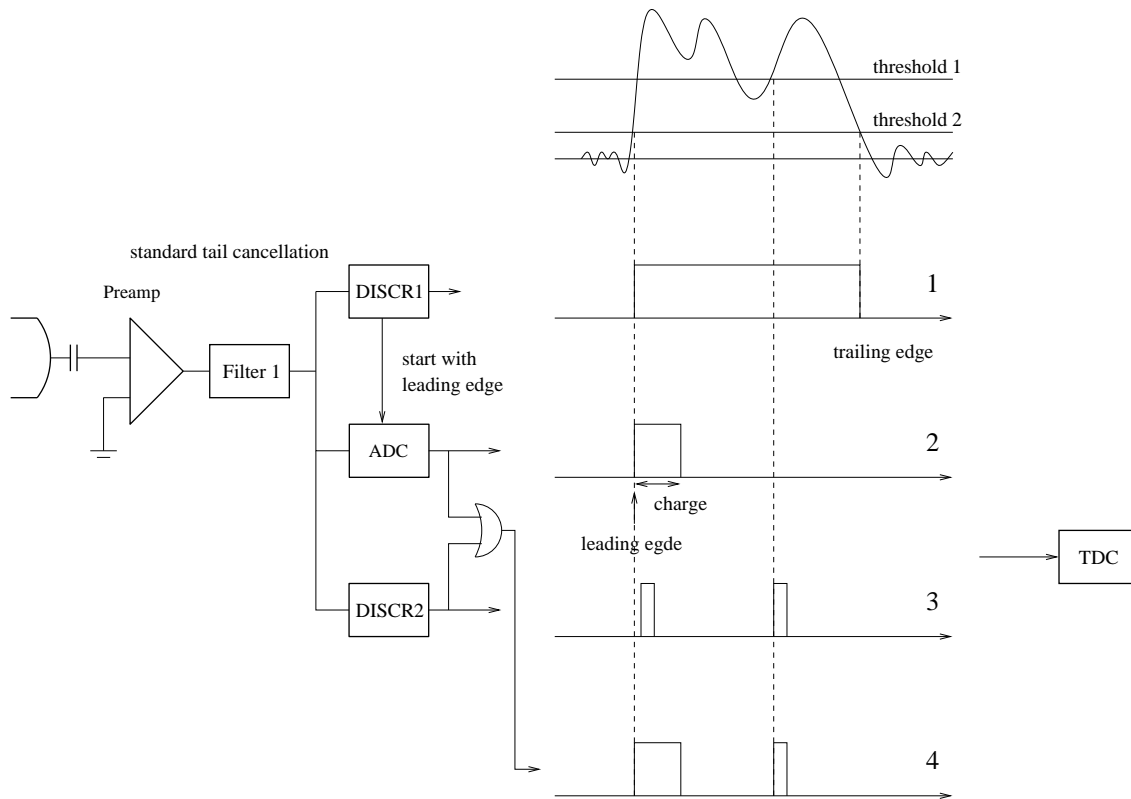


**Figure 12.26** : In this scheme the fronted electronics has two separate discriminators. In normal mode one would read only output (1) or (2) which gives one hit per signal. In case of trouble with high occupancies one would read out line (4) which is the OR of (2) and (3). The high threshold discriminator would have a fixed output pulse width of 10-20ns ( $<$  ADC gate), so the first pulse will always be 'eaten' by the output pulse of line (2). Since the pulse width of the ADC channel is always  $>$  ADC gate we can identify pulses from the high and the low threshold. The advantage of this scheme is that one gets the good resolution for the first leading edge without the time slewing correction. The only disadvantage of this scheme is the fact that we get a systematic shift of the second hit time because we can determine the  $rt$ -relation only with the low threshold.



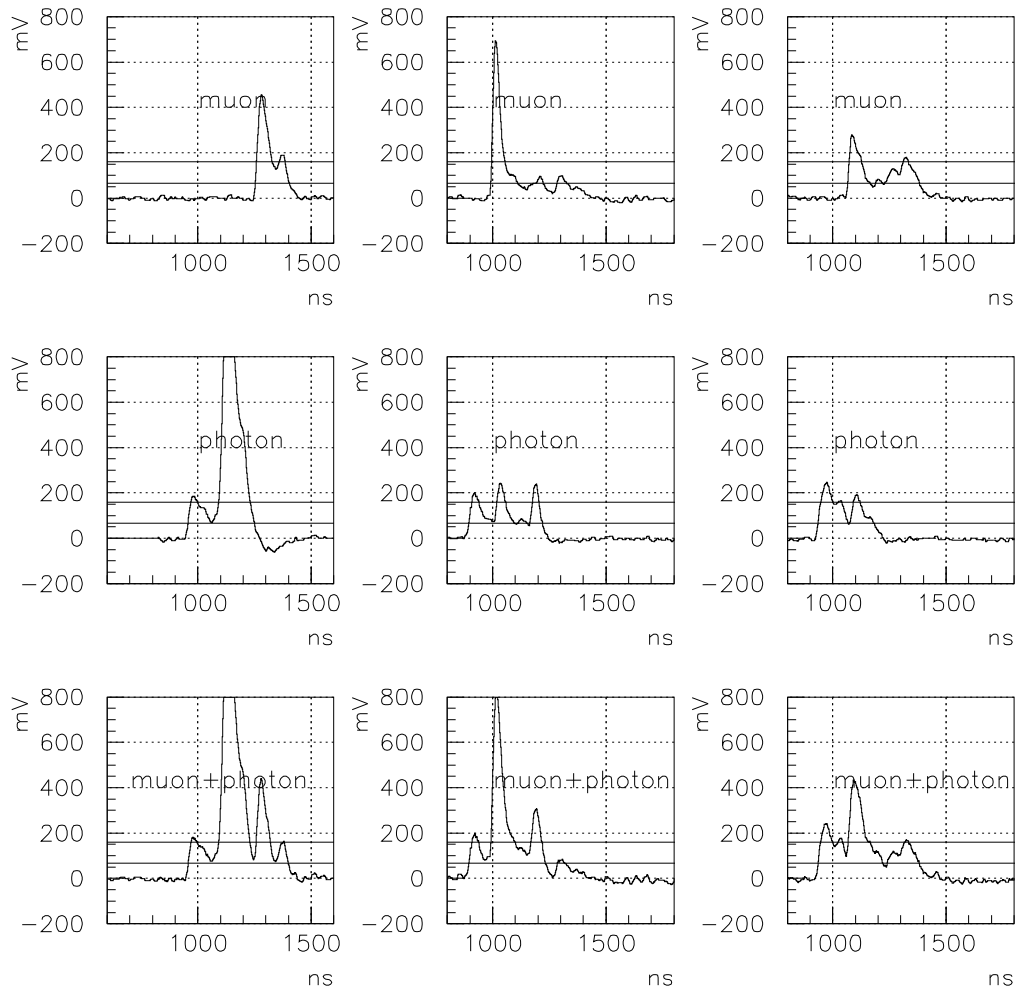


**Figure 12.27** : A high threshold discriminator can identify the leading edge of the muon signal that is piled up with a photon background hit.

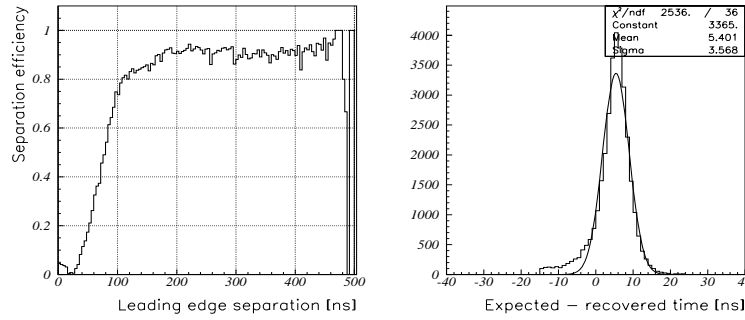


**Figure 12.28** : Separation efficiency for tracks perpendicular to the wire. The second histogram shows the additional bias in resolution for the overlaid track. For a gas with a drift velocity of about  $30\mu\text{m}/\text{ns}$  this would correspond to an additional bias of  $105\mu\text{m}$  which has to be added in square to the nominal resolution at the given threshold.

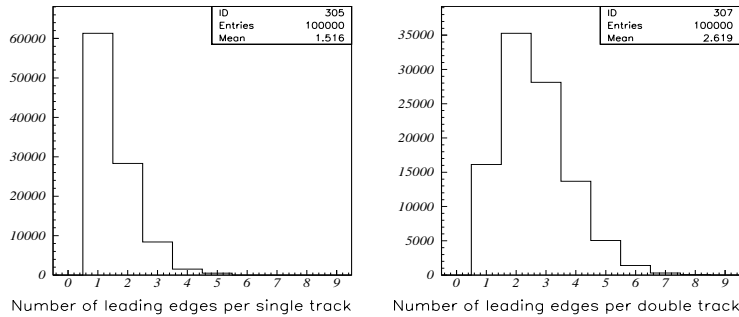


**Figure 12.29** : Average number of hits per single track and per double track.

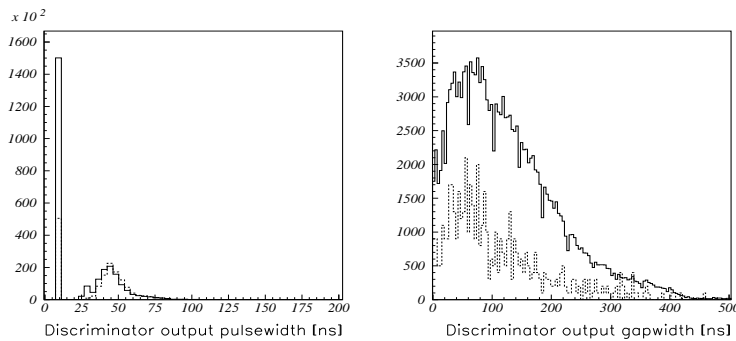


**Figure 12.30** : Pulse width and the time between the pulses (gap width) of the discriminator output. The dotted line corresponds to single tracks, the solid line corresponds to double tracks. Note that these histograms show the pulse and gap width for the mode where the charge is encoded in the discriminator output. The gate assumed is  $20\text{ns}$  and the charge information is converted into a time proportional to the charge.

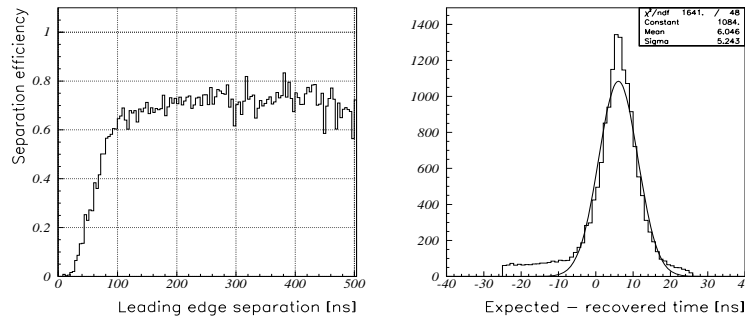


**Figure 12.31** : Separation efficiency for muons and pulses from Bi208 photons. The separation efficiency is lower due to the fact that the photon pulses are on average twice as high as the muon pulses. One can imagine that a 'small' muon pulse being hidden by a 'big' photon pulse is affected more than the muon-muon case in the previous figure. This can also be seen by the bigger bias in resolution.

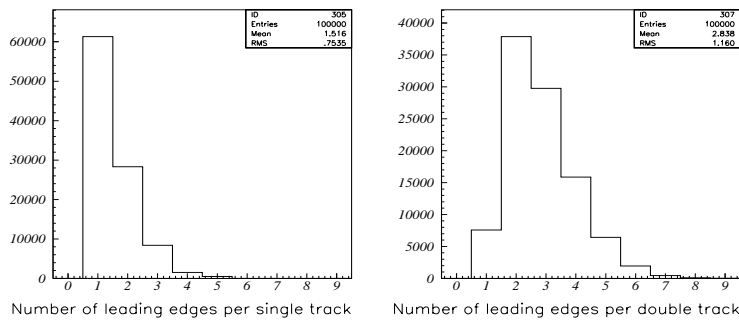


**Figure 12.32** : Average number of hits per single track and per double track.

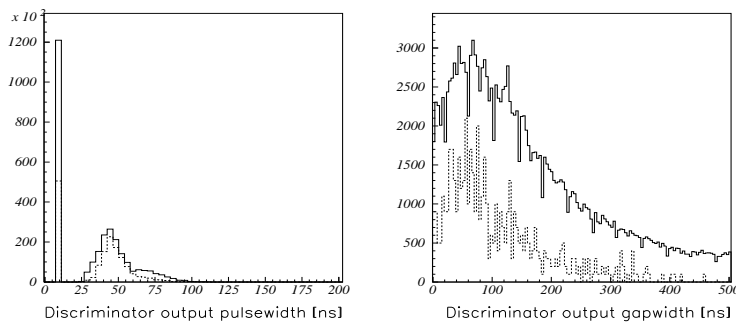


**Figure 12.33** : Pulse width and the time between the pulses (gap width) of the discriminator output. The dotted line corresponds to single tracks, the solid line corresponds to double tracks.

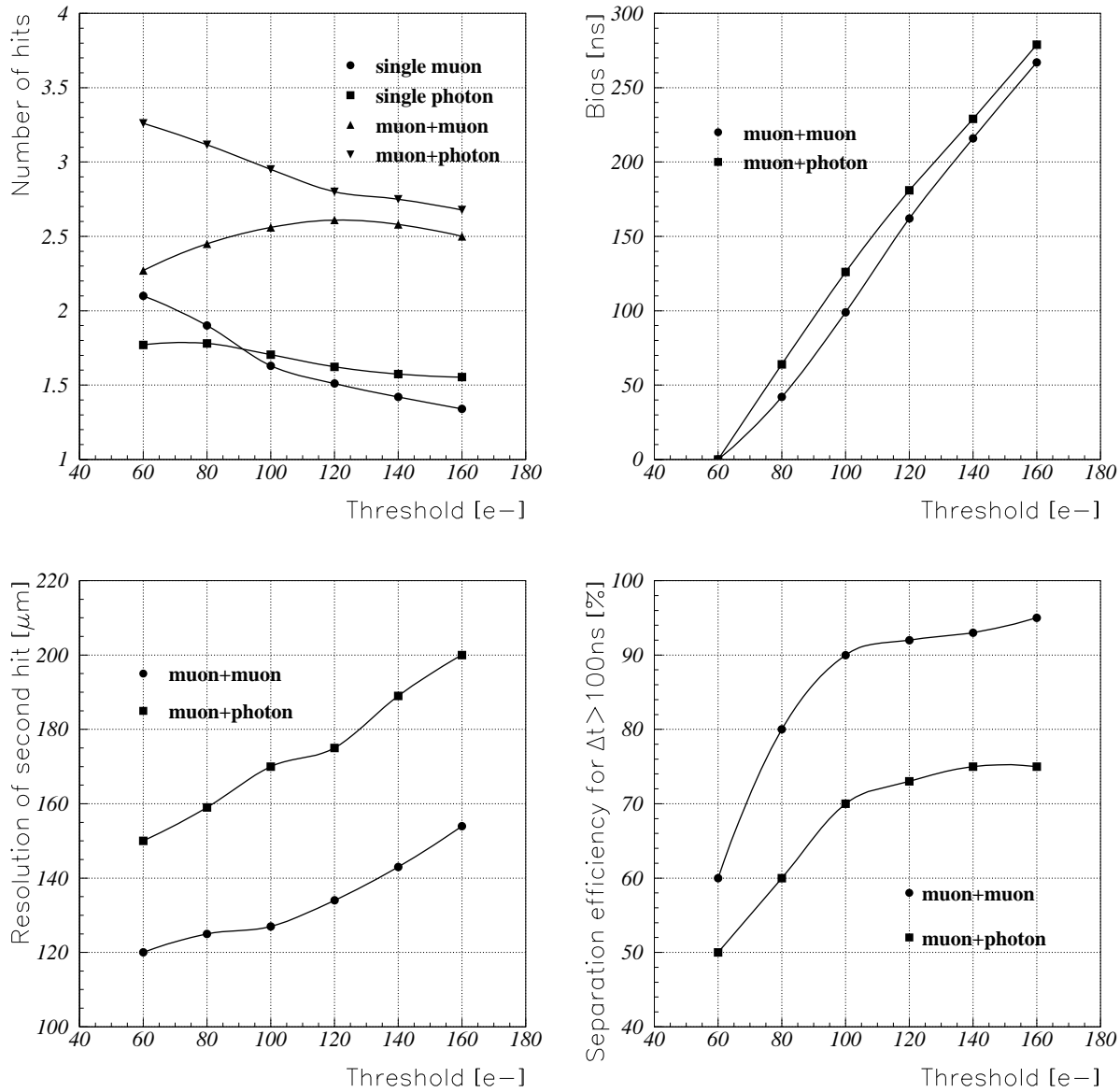


**Figure 12.34 :** Threshold dependence of various parameters. The number of hits per single signal decreases by raising the threshold, the separation efficiency increases, the resolution of the recovered hit decreases. One minor problem of the double threshold scheme is a systematic shift of the second track. We establish the  $rt$ -relation by using the hit times of the low threshold discriminator. If we use this  $rt$ -relation for the high threshold hit times we get a systematic shift of the track position. Since this shift only depends on the threshold we can correct for it.

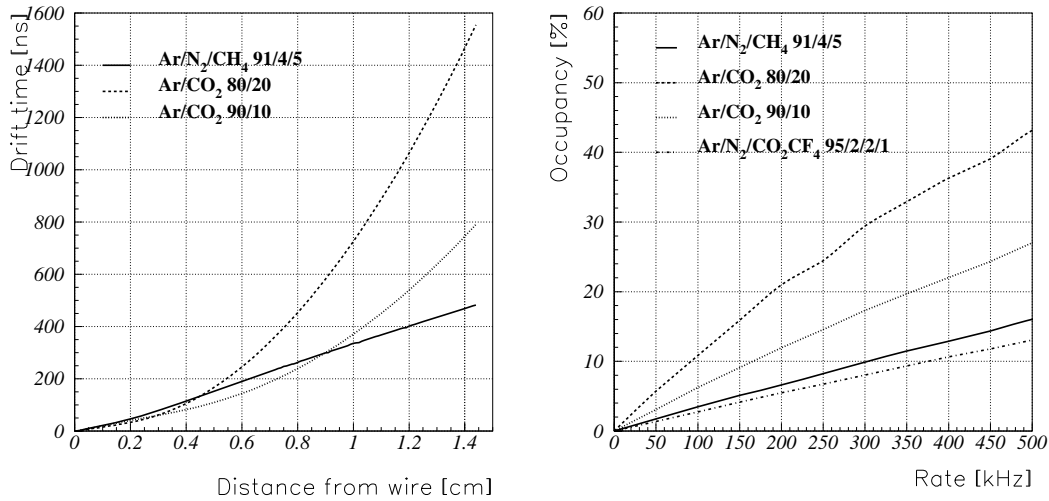


**Figure 12.35** : Space-drifttime relation and corresponding occupancy for different gas mixtures and photon background rates. A dead time of 100ns due to electronics response has been added. The occupancy is defined as the fraction of time where the tube is 'occupied' by drifting electrons.

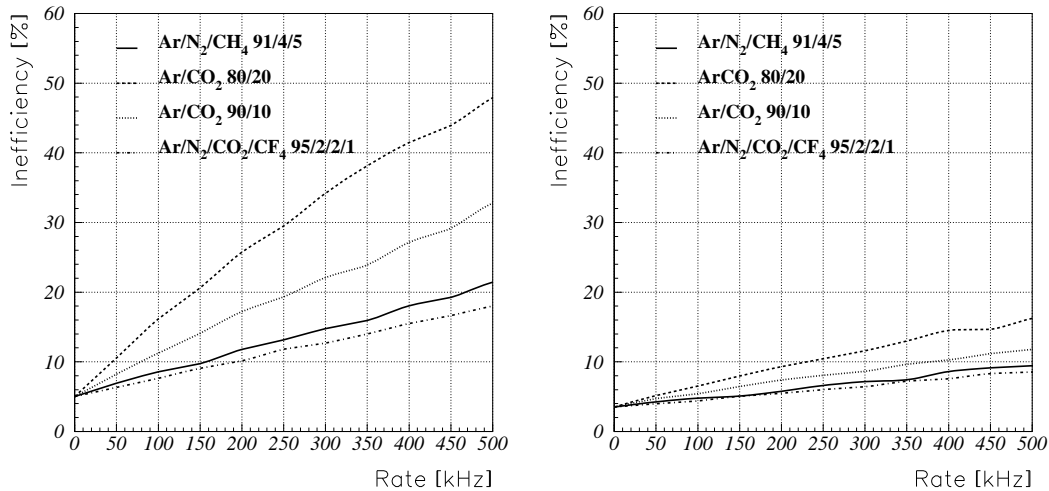


**Figure 12.36** : The left figure shows the MDT inefficiency for different rates assuming no multi hit capability (channel 1 or 2 in fig. 12.26). The right figure shows the MDT inefficiency using the double threshold scheme (fig. 12.26). For zero background rate we improve from 6% inefficiency to 4% inefficiency. The poor improvement is due to the fact that delta electrons are very close to the muon track. The efficiency dependence on the uncorrelated background rate is reduced significantly using double track separation.

# Chapter 13

## Summary and conclusion

- Detailed measurements and simulations of the MDT response to photons and charged particles were evaluated within this work in order to optimize spatial resolution and efficiency, which are the crucial MDT performance parameters for providing good momentum resolution and robust pattern recognition efficiency with the ATLAS muon spectrometer.
- The result of this work is a detailed understanding of all the components limiting the spatial resolution and efficiency of drift chambers. Detector physics parameters like diffusion, charge fluctuations, gas gain, gain fluctuations, space charge, temperature as well as electronics parameters like noise, preamplifier peaking time, discriminator threshold, tail cancellation networks and baseline variations were evaluated and compared to measurements. Externally induced wire vibrations as well as the recently discovered effect of avalanche induced wire vibrations were studied.
- The study resulted in the design of a frontend electronics scheme for the ATLAS MDT chambers that is currently under development (fig. 13.1). This scheme is capable of digitizing all the interesting information that is contained in the wire chamber signal and reading it into a single output channel.
- The detailed simulation of the detector physics processes was performed with HEED [6], MAGBOLTZ [7] and GARFIELD [8]. The quantitative comparison of simulation and measurements initiated a considerable improvement and extension of the GARFIELD program during the last two years.
- The electronics was simulated with PSPICE [19] and stand alone programs. The electronics can also be simulated with GARFIELD since recently.
- The response of individual ionization electron pulse shapes does not agree very well with the measurements and has to be matched phenomenologically. A likely explanation for this fact are space charge effects within the avalanche that reduce the electric field and hence the fraction of the electron component of the signal.

- The comparison of signals from charged particle tracks shows excellent agreement in every respect after matching the single electron response.
- A comparison of MDT resolution measurements with the simulation shows very good agreement, indicating that we have a complete understanding of the detector physics processes.
- The optimized operating parameters and justifications for the individual functions of the electronics frontend scheme (fig. 13.1) are the following:
  1. The MDT spatial resolution improves with pressure due to reduced diffusion and reduced charge fluctuations. A pressure of 3 bars is a good compromise in terms of resolution and total charge deposit.
  2. A gas mixture similar to the  $Ar/N_2/CH_4$  mixture with respect to maximum drift time ( $< 500ns$ ) and linearity is desired to avoid high occupancy ( $< 10\%$ ) and decreased resolution due to space charge and temperature effects.
  3. For a count rate of  $500Hz/cm^2$  and a gas gain of  $2 \times 10^4$ , the bias in resolution due to space charge is  $30\mu m$  for the  $Ar/N_2/CH_4 91/4/5$  gas mixture. The bias in resolution for a temperature change of 2K is  $10\mu m$  for this gas.
  4. The gas gain has an impact on the resolution through the minimum applicable threshold which is set to  $5\sigma_{noise}$ . The gas gain should be  $> 2 \times 10^4$  to provide good spatial resolution and high efficiency. It should be  $< 6 \times 10^4$  to avoid gas gain drop (20% at a gain of  $6 \times 10^4$  including a safety factor of 5 on the nominal background rate), decreased resolution due to space charge effects and wire vibrations. The increase in resolution from a gain of  $2 \times 10^4$  ( $5\sigma_{noise}=18$  electrons) to  $6 \times 10^4$  ( $5\sigma_{noise}=6$  electrons) is  $\approx 20\mu m$  and improves only marginally for higher gas gains.
  5. A very short preamplifier peaking time is desirable to provide good spatial resolution, however the choice of technology for the preamp design as well as multiple threshold crossings per single signal suggest a peaking time of 10 – 15ns. The difference in resolution for  $tp=5ns$  and  $tp=15ns$  is  $\approx 15\mu m$ .
  6. To avoid multiple threshold crossings per signal, the tail cancellation networks have to be adjusted differently for MDT chambers of different size which is due to a change of the signal shaping properties with the MDT length. The discriminator should have hysteresis that is adjustable over a wide range to avoid multiple threshold crossings. For a double pole/zero network together with a hysteresis set to half of the threshold we expect only one threshold crossing per signal.
  7. The trailing edge of the MDT signal has a fixed time relation with respect to the bunch crossing so it can be used to reject out of time background events which improves the pattern recognition efficiency. Using a time over threshold discriminator with a threshold set to 20 electrons and a hysteresis value of half the threshold, the trailing edge resolution is  $\approx 20ns$  neglecting B-field effects. Leading and trailing edge of the signal can be read out using channel (1) of the front end scheme.

8. The detailed study of the individual contributions to the spatial resolution showed that charge fluctuations in the leading edge of the signal causing time slewing effects are the biggest factor limiting the resolution. A time slewing correction scheme using a short gate ADC was developed within this work. Integrating the signal during 20ns following the threshold crossing time measures the signal rise time and the charge information is used to improve the spatial resolution by  $\approx 15\mu m$ . In addition to the improvement of the resolution the threshold dependence of the resolution is decreased considerably with this method. A charge measurement provides in addition a very useful tool for the chamber performance diagnostics. Leading edge and charge information can be obtained by reading channel (2) as shown in fig. 13.1.
9. The MDT inefficiency was studied by recording the MDT signals and analysing the pulse shapes of the inefficient events.
10. The MDT hit efficiency is very close to 100% if the muon track is  $> 150\mu m$  from the wall, i.e. the probability that there is at least one threshold crossing if a muon crosses the tube is very close to 100% for a threshold of 20 electrons.
11. At a threshold of 20 electrons there is an inefficiency of  $\approx 6\%$  due to delta electrons created by the muon in the tube wall or the counting gas (6% of the hits outside  $5\sigma$  of the predicted position). By raising the threshold we start to lose the leading edges for tracks very close to the wire, so a threshold  $\leq 20$  electrons is essential for high efficiency. Increasing the gas gain does not increase the efficiency.
12. Using a second discriminator with a threshold of  $\approx 120$  electrons we can identify muon signals superimposed to other signals from tracks perpendicular to the wire with an efficiency of 90% if the leading edges are separated more than 100ns. A muon being piled up to a photon background hit can be detected with a probability of  $\approx 70\%$ . A second discriminator would require a second readout channel which is not desired. However one can perform an OR of the high level discriminator output and the low level discriminator output and read the combined information into one TDC channel. Fixing the pulse width of the high threshold output to 10ns the pulses from the two discriminators can be identified and the redundant leading edge information is 'eaten' by the OR procedure (fig. 13.1). Using this scheme, the average number of hits per single signal is  $\approx 1.7$ .
13. The total count rate per tube in the worst region of the detector is 400kHz (including a safety factor of 5). If we do not use an active baseline restoration circuit, the baseline shift resulting from the unavoidable AC coupling of the system is 30 electrons with a big fluctuation around this value. An active baseline restoration circuit is therefore required.
14. MDT wire vibrations induced by a repulsion between positively charged wire and the positive ions created in the avalanche were studied. The extrapolation of the measurements to the maximum expected counting rate of 400kHz per tube gave a value for the wire displacement of  $\approx 20\mu m$  rms for a gas gain of



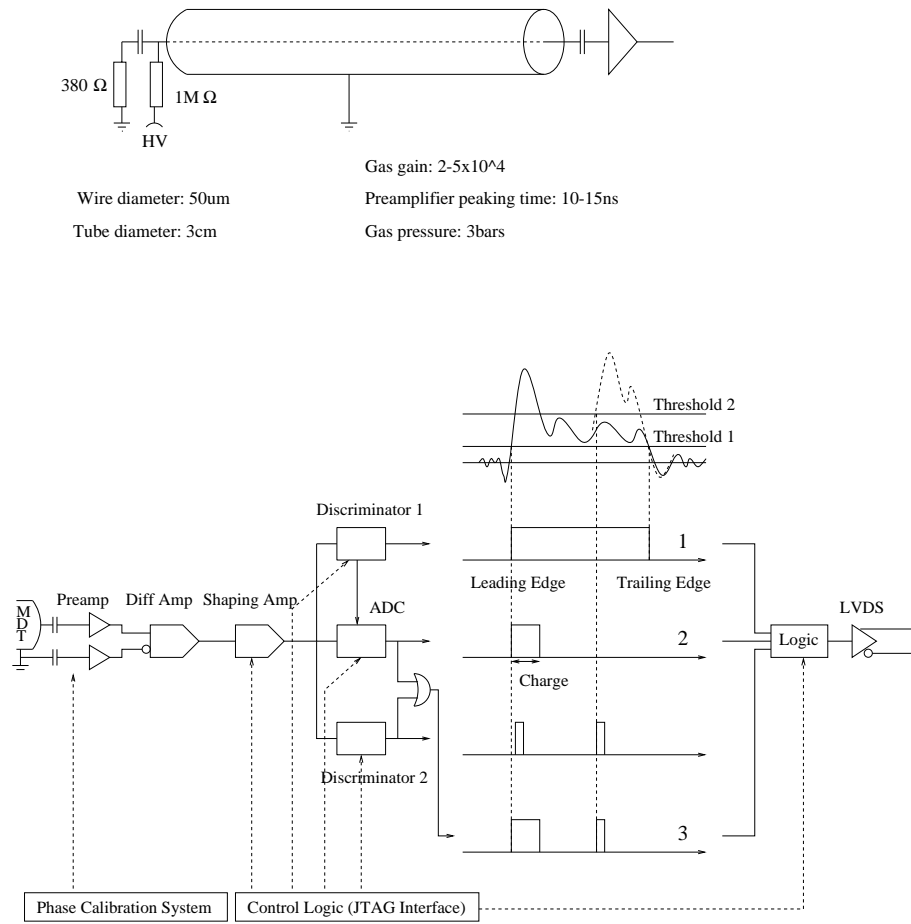


**Figure 13.1** : Front end schematic and operating parameters for the ATLAS MDT chambers.

$4 \times 10^4$  and an average energy deposit of  $\approx 35keV$  per event which is in good agreement with the calculations.

- Externally induced vibrations of the MDT wires were also studied. The damping of the MDT wires is such that for an excitation amplitude of  $1\mu m$  at one end of the tube, the wire resonant amplitude is  $50 - 100\mu m$ .

# Acknowledgements

First of all I want to thank Chris Fabjan for his continuous support throughout my stay at CERN. His ability of motivating people is truly amazing. I remember a day when after lots of frustration with my work I was on my way to his office to tell him that I would quit work immediately and leaving his office 5 minutes later fully convinced that working in High Energy Physics is the best thing in the world. Thanks also for the nice skiing days ! I want to thank Günther Neuhofer for giving me the chance to stay at CERN in summer 1994. I really enjoyed his friendliness, especially during the times of confusion in the beginning of my stay.

From Rob Veenhof, the author of GARFIELD, I learned most things that I know about drift chambers and high energy physics. He never got tired of answering my questions and adapting his program to all my needs. I will always remember the midnight coffee breaks when he tried to convince me that not physics but food and mountains are the most important things in the world.

During the first months of my stay at CERN I worked together with Georg Viehhauser who, as my 'supervisor', introduced me to the ATLAS experiment and the test beam activities. Many thanks to Valeri Tcherniatine who did all the pioneering work concerning MDT detector physics. Most of my work was strongly influenced by his ideas and discussions with him. Thanks to Vinnie Polychronakos for encouraging me so much and for teaching me the difference between a 'gedanken experiment' and a real one.

I also enjoyed a lot to work in the test beam with Nigel Hessey, Chuck Gruhn, Mario Deile, Joerg Dubbert and Thomas Sammer who all know that progress can only be achieved by working hard (and having a drink when the work is done).

Thanks to the Boston crew Eric Hazen, John Huth, John Oliver and Jim Shank for not giving up trying to explain electronics issues to a physicist - I am very much looking forward to working with them in the future.

I always learned a lot when working together with Frank Linde whom I really admire for his competence and endurance. Thanks also to Joerg Wotschack, Walter Blum and Michael Treichel for their support and help.

Whenever I spent more than two days with Mark Hill I started to have doubts that space and time behave according to physics laws. With Andreas and Michael I used to share the opinion that starting to go to Charlie's Pub on Tuesday is the best way to prepare for the weekend. I had a great time with our band, the 'Bowie Trashers' Catherine (Voc), Simon(Voc), Kurt(Git.) and Roman (Drums) - 'We don't need a key - we break it'. Because of our incredibly loud rehearsals I became deaf enough to be able to work in my new office without feeling disturbed by all the noise around me. Roman was my office neighbour during my first year and he supplied me with music and chocolate. Marko, the number one trouble solver, helped me a lot to get started at CERN. Thanks to Uli, Ingrid, Catharina, Silvia, Michael, Guenter, Martin, Alex and all the others who made my stay at CERN so enjoyable.

Thanks a lot to my family for all the support and giving me the feeling that I have a real home. I am of course most grateful to Edda who is the one person who really makes my life worth living.

# Bibliography

- [1] A. Sopczak, Status of Higgs Hunting at the Z-resonance and its Prospects at LEP2, CERN-PPE/94-73, 9-may 1994.
- [2] ATLAS Technical Proposal, CERN/LHCC/94-43, LHCC/P2, (1994).
- [3] ATLAS Muon Spectrometer Technical Design Report, CERN/LHCC/97-22, ATLAS TDR 10, (1997)
- [4] Edda Gschwendtner et al., Analysis of the X-tomograph scan data for MDT chamber prototypes, ATLAS internal note MUON-NO-175 (1997).
- [5] Georg Viehhauser, Detector Physics of the ATLAS precision muon chambers, doctoral thesis, CERN (1996).
- [6] Igor Smirnov, HEED, program to compute energy loss of particles in gases. Version 1.01, CERN.
- [7] S. Biagi, MAGBOLTZ, program to compute gas transport parameters, Version 1.10, CERN.
- [8] Rob Veenhof, GARFIELD, a drift chamber simulation program, Version 5.35, CERN.
- [9] V.K. Ermilova, L.P. Kotenko, G.I. Merzon and V.A. Chechin, primary specific ionization of relativistic particles in gases, Sov. Phys.-JETP 29, 861 (1969).
- [10] F. Lapique and F. Piuz, Simulation of the measurement by primary cluster counting of the energy lost by a relativistic ionizing particle in argon, NIM 175, 297 (1980).
- [11] M. Deile, J. Dubbert, N.P. Hessey et al., Testbeam Studies of the gas mixtures  $Ar : N_2 : CH_4 = 91:4:5$  ... ATLAS internal note MUON-NO-122 (1996), CERN.
- [12] G. D. Alkhazov, Statistics of electron avalanches and ultimate resolution of proportional counters, NIM 89, 155(1970).
- [13] Landolt-Boernstein, vol.4/3, Eigenschaften des Plasmas, no 44315, 6th edn (Springer, Berlin Heidelberg 1957).
- [14] W. Blum, L. Rolandi, Particle Detection with Drift Chambers, Springer Verlag, Berlin-Heidelberg-New York (1993).

- [15] S. Ramo, Currents induced in electron motion, PROC. IRE 27, 584 (1939).
- [16] M. Deile, J. Dubbert, N.P Hessey, Charge division and intrinsic pulse shaping in drift tubes, ATLAS internal note MUON-NO-105 (1996).
- [17] V. Radeka, Ann. Rev. Nucl. Part. Sci. 1988, 38, 217, 77
- [18] P.W. Nicholson, Nuclear Electronics, John Wiley and Sons.
- [19] PSPICE, analog circuit simulator, version 6.2 (1995).
- [20] C.Blocker, J.Huth, J.Oliver, Noise Considerations for the ATLAS Muon Front-End Electronics, ATLAS internal note MUON-NO-80 (1995)
- [21] R.A. Boie, A.T Hrisoho and P. Rehak, signal shaping and tail cancellation for gas proportional detectors at high counting rates, NIM 192 (1982).
- [22] NIKHEF, National Institute for Nuclear Physics and High Energy Physics. Kruislaan 409, 1098 SJ Amsterdam, Netherlands.
- [23] Lecroy Digital Oscilloscope, 9360 series.
- [24] L3 Wire-Amplifier NH19-6112, P. Rewiersma, NIKHEF-H [22].
- [25] M. Hill et al., Resolution Studies of a Prototype Set of High Pressure Monitored, ATLAS internal note MUON-NO-121 (1996).
- [26] Ludovico Pontecorvo (INFN Roma), private communication (1997).
- [27] Mario Deile, Joerg Dubbert (LMU), private communication.
- [28] Common base preamplifier IO-354-2 and Shaping Amplifier IO532-01, Instrumentation Division, Brookhaven National Laboratory, Upton, New York 11973.
- [29] LMU, Ludwig Maximilians Universitaet Muenchen, Geschwister-Scholl-Platz 1, 80539 Muenchen, Germany.
- [30] M2, Muon beam line at CERN, site Preveessin, BAT. 888, muon rate in the test beam area  $\approx 1Hz/cm^2$ .
- [31] Max-Planck-Institut fuer Physik (Werner-Heisenberg-Institut), Foehringer Ring 6, D-80805 Muenchen, Germany.
- [32] Joerg Dubbert, Bestimmung der Ortsaufloesung von Hochdruckdriftrohren fuer das Myon-Spektrometer des ATLAS Experimentes, diploma thesis, Aug. 1996 (LMU [29]).
- [33] W. Diethorn, A methane proportional counter system for natural radiocarbon measurements, USAEC Report NY06628 (1956)
- [34] L. Baliev, A. Boisov, Finite Element Analysis of the Vibration Problem for ATLAS MDT chamber Part 1, MUON-NO-130 (1996).

- [35] I.R.Boyko et al., Vibration of Signal Wires under Irradiation, ATLAS internal note MUON-NO-79 (1995).
- [36] M. Collet, Study of detector dynamics part 1, CERN technical note TA1/96 2 (1996).
- [37] DATCHA, Demonstration of ATLAS Chamber Alignment, UA1 pit, CERN, installed in 1996/97.
- [38] A. Ferrari, INFN-Milan, private communication (1996).
- [39] E.Hazen, J. Shank, Status of the Front End Electronics for the MDT System, ATLAS internal note MUON-NO-111 (1996).

# Curriculum Vitae

Werner Riegler

Auf der Schanz 9, 4360 Grein, Österreich

Geboren am 30.3.1970 in Enns, Österreich.

Famimienstand: ledig

- **1976-1980:** Volksschule in Grein (OÖ)
- **1980-1988:** Besuch des Bundesrealgymnasiums in Amstetten (NÖ), Realistischer Zweig mit Schwerpunkt Physik und Mathematik.
- **1988-1995:** Studium der Technischen Physik an der Technischen Universität Wien. Diplomarbeit 'Darstellung der Grundlagen der Allgemeinen Relativitätstheorie' am Institut für theoretische Physik.
- **Sommer 1995** Forschungsaufenthalt am europäischen Zentrum für Teilchenphysik CERN in Genf. Mitarbeit am Experiment NA48. Institut für Hochenergiephysik.
- **1992-1995:** Studium der Astronomie an der Universität Wien.
- **1995-1997:** Doktoratsstudium am CERN als Mitglied der ATLAS Gruppe, finanziert vom Bundesministerium für Wissenschaft und Forschung.
- **1.11. 1997:** Anstellung als Research Assistent an der Harvard Universität in Boston, USA.